Interfacing Ultracold Atoms and a Cryogenic Micromechanical Oscillator

Dissertation
zur Erlangung des Doktorgrades
des Departments Physik
der Universität Hamburg

vorgelegt von
Andreas Bick
aus Duisburg

Hamburg
2015

Gutachter der Dissertation:	Prof. Dr. Klaus Sengstock Prof. Dr. Roman Schnabel
Gutachter der Disputation:	Prof. Dr. Klaus Sengstock Prof. Dr. Roland Wiesendanger
Datum der Disputation:	06.02.2015
Vorsitzender des Prüfungsausschusses:	Prof. Dr. Caren Hagner
Vorsitzender des Promotionsausschusses:	Prof. Dr. Jan Louis
Dekan der Fakultät für Mathematik, Informatik und Naturwissenschaften:	Prof. Dr. Heinrich Graener

to my mom

Abstract

Why is it that our world, which consists of many microscopic quantum systems, can be described in terms of classical physics? This fundamental question about the transition between these two diametrically opposed theories is an unsolved problem of modern physics. In recent years, tremendous progress in the field of optomechanics paved the way for the observation of a large variety of quantum phenomena far beyond the microcosmos. Additional possibilities arise from the skillful combination of different quantum systems to create a so-called hybrid quantum system. In these systems, new possibilities to prepare and detect non-classical states in macroscopic systems arise.
In this thesis the setup of a new hybrid quantum system is described that consists of two entirely different systems. The first building block is a ^{87}Rb Bose-Einstein condensate *(BEC)* - an ideal realization of a many-body ground state. The second building block is an optomechanical system in a cryogenic environment, a membrane in an optical cavity *(membrane in the middle - MiM)*. Both systems are coupled over a macroscopic distance via a light field.
In this particular case, the MiM system is realized using a Si_3N_4 membrane in a fiber-based Fabry-Pérot cavity. In the course of this thesis, an asymmetric cavity with high reflectivity on resonance was identified as the ideal candidate. Such a system has not yet been reported in the literature, but allows for a strong coupling between the two constituents of the hybrid quantum system. Additionally, fibers are ideally suited to bring light into cryogenic environments due to their low thermal conductivity. In the cryostat, they will be mounted in novel fixe-axis goniometers.
The key parameters for an asymmetric fiber-based cavity is the mode overlap between the cavity mode and the fiber mode. Due to an interference effect, a small change in the mode match already results in a massive amount of light loss of the reflected cavity mode in the fiber. This previously unknown effect was identified as crucial in asymmetric fiber-based cavities and is studied in this thesis using an analytical model, which is verified using numerical calculations and experimental data.
The curved structures necessary for a stable cavity mode in the MiM system are processed onto the fiber tips using CO_2 laser pulses. The light is absorbed, resulting in the evaporation of material. Afterwards, the fiber is analyzed using a Linnik interference microscope to determine the radius of curvature of the processed feature. With this knowledge, an asymmetric fiber-based MiM system at room temperature was set up and in first measurements the mechanical quality factor and the optomechanical coupling strength were studied.
Furthermore, a setup to create BECs was planned and realized. Here, in first measurements, Bose-Einstein condensation was observed. The system is based on a 2D/3D MOT design in combination with a *Hybrid-Dee* magnetic trap. Using radio-frequency evaporation, BECs with $N \approx 8 \times 10^4$ atoms can be produced at a cycle time of 30 s.

Zusammenfassung

Warum lässt sich unsere Welt, die aus vielen einzelnen mikroskopischen quantenmechanischen Systemen besteht, so gut klassisch beschreiben? Diese fundamentale Frage bezgl. des Übergang zwischen jenen beiden diametralen Theorien ist ein ungelöstes Problem der modernen Physik. In den letzten Jahren haben bedeutende Fortschritte im Bereich der Optomechanik den Weg zur Beobachtung vielfältiger quantenmechanischer Phänomene weit jenseits des Mikrokosmos geebnet. Darüber hinausreichende Möglichkeiten ergeben sich durch die geschickte Kombination zweier verschiedener Quantensysteme, einem so genannten hybriden Quantensystem. In solchen kombinierten Systemen ergeben sich neue Möglichkeiten beispielsweise zur Präparation und Detektion nichtklassischer Zustände makroskopischer Objekte.

In dieser Arbeit wird der Aufbau eines neuartigen hybriden Quantensystems beschrieben, welches sich aus zwei grundverschiedenen Systemen zusammensetzt. Der erste Baustein ist ein ^{87}Rb Bose-Einstein Kondensat *(BEC)* - eine ideale Realisierung eines Vielteilchen-Grundzustandes. Der zweite Baustein ist ein optomechanisches System in kryogener Umgebung, eine Membran in einem optischen Resonator *(membrane in the middle - MiM)*. Beide Systeme werden über eine makroskopische Strecke gekoppelt, wobei die Wechselwirkung über ein Lichtfeld vermittelt wird.

Im Speziellen wird das MiM System, welches im Rahmen dieser Arbeit realisiert wurde, durch einen faser-basierten Fabry-Pérot Resonator und eine Si_3N_4 Membran gebildet. Es wurde ein asymmetrischer Resonator mit hoher Reflektivität auf Resonanz als optimale Lösung identifiziert. Ein solches System wurde bisher noch nicht experimentell realisiert, ermöglicht aber eine hohe Kopplungsstärke zwischen beiden Bausteinen. Fasern sind aufgrund ihrer schlechten thermischen Leitfähigkeit ideal geeignet um Licht in kryogene Umgebung zu bringen. Sie werden im Kryostat in neuartigen fünf-achsigen Goniometern, basierend auf Piezomotoren, gehaltert.

Der kritische Parameter für asymmetrische faser-basierte Resonatoren ist der Überlapp zwischen der Fasermode und der Resonatormode. Durch einen Interferenzeffekt sorgt bereits eine leichte Abweichung vom optimalen Modenüberlapp für einen massiven Verlust des reflektierten Lichts in der Faser. Dieser neuartige Effekt, der in asymmetrischen faser-basierten Resonatoren von essentieller Bedeutung ist, wurde mithilfe von einem analytischen Modell verstanden und mit numerischen Simulationen und experimentellen Untersuchungen verifiziert.

Die für eine stabile Resonatormode in dem MiM System notwendigen gekrümmten Strukturen auf den Faser-Endflächen werden mithilfe von CO_2-Laserpulsen erzeugt. Das Licht wird absorbiert und evaporiert Material von der Oberfläche. Nachträglich wird die bearbeitete Faser mit einem Linnik Interferenzmikroskop vermessen und der Krümmungsradius bestimmt. Auf der Basis dieser Erkenntnisse wurde ein asymmetrisches faser-basiertes MiM System bei Raumtemperatur aufgebaut und in ersten Messungen die Güte des mechanischen Oszillators sowie die optomechanische Kopplungsstärke vermessen.

Des Weiteren wurde ein Aufbau zur zuverlässigen Erzeugung von BECs geplant, realisiert und in ersten Messungen Bose-Einstein Kondensation beobachtet. Der Aufbau besteht aus einem 2D/3D MOT Design in Kombination mit einer *Hybrid-Dee* Magnetfalle. Mittels Radiofrequenz-Evaporation können BECs mit $N \approx 8 \times 10^4$ Atomen bei einer Zykluszeit von 30 s erzeugt werden.

Contents

Chapter 1

Introduction

Over the last decades, there has been a huge effort in many different fields of physics to prepare and control various systems in their quantum mechanical ground state. Successful realizations include such diverse objects as single ions [1], Bose-Einstein condensates [2, 3], superconducting q-bits [4] or the rather recent addition, macroscopic mechanical oscillators [5, 6]. This so-called field of optomechanics, the control and manipulation of mechanical oscillators using light fields [7], had tremendous success in recent years, pushing the experimental study of quantum mechanics further into the dense macroscopic world. Notable examples are the observation of strong coupling between an oscillator and a cavity field [8], nonlinear optomechanical coupling [9], active feedback cooling of the mechanical motion [10], resolved sideband cooling [11], observation of quantum motion [12], coherent wavelength conversion [13], generation of squeezed light [14, 15], and the preparation of diverse mechanical oscillators in or near the motional ground state [5, 6, 16–19].

These prospects and the possibility to functionalize mechanical systems [5, 20, 21] to couple them to almost anything in a controlled manner sparked the idea to realize and study hybrid quantum systems by combining mechanical resonators with different other quantum mechanical systems [22]. One major goal of this approach is to combine the advantages of different experimentally accessible quantum systems and to thereby overcome existing limitations in e.g. cooling, preparation or detection present in the individual parts to yield a maximum benefit for the performance of the coupled hybrid system. In a landmark experiment in 2010 [23], the coherent coupling of a fully controllable two level quantum system, a q-bit, to a mechanical oscillator in the GHz range allowed for the creation of non classical states of motion.

Due to their isolation from the environment and long coherence times, atomic ensembles are ideal companions for mechanical oscillators to compose new hybrid quantum systems. A BEC is a perfect realization of the quantum mechanical ground state of a many-body system. Furthermore, the sophisticated toolbox to manipulate all external and internal degrees of freedom of cold atoms [24] are readily available for the benefit of the combined device. This will open completely new avenues for the manipulation,

preparation and detection of the mechanical oscillator. Conversely, the mechanical element could be utilized as a quantum limited force sensor for the atomic system [25], giving rise to new prospects for the field of ultracold quantum gases [22].

The possibility to prepare both individual building blocks in their quantum mechanical ground state, as well as a strong coherent coupling between theses parts, much stronger than any decoherence processes connected to interaction with the environment, are desirable properties in an ideal hybrid quantum system. Examples are the coupling of a cantilever to a single spin of a nitrogen-vacancy center in diamond [26–28] or the coupling of atoms or molecules to superconducting microwave circuits utilizing superconducting stripline cavities combining the fields of circuit QED with AMO systems [29–32]. Both systems benefit from the comparatively strong coupling that can be generated via magnetic- and mw-fields respectively. Remarkable experimental progress was made in the last years, e.g. by trapping a BEC in the vicinity of a coplanar resonator at 4.2 K [33], preparing a cloud of atoms in a dilution refrigerator [34] or trapping atoms with a cryogenic atom chip [35].

All these approaches mentioned above are based on short range interaction between the two quantum systems. It is also possible to create a coherent quantum-link between two systems over a large distance, as realized between two identical cavity QED experiments [36] where the coupling between the two constituents is mediated by light. Using two different quantum systems enables the realization of a long-distance coupled hybrid quantum system as sketched in Figure 1.1. In this approach, both constituents can be housed under optimal conditions without any trade-offs.

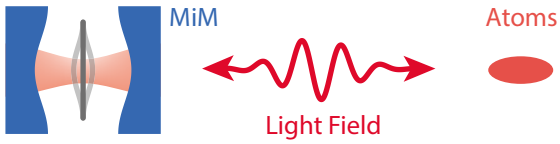

Figure 1.1: Sketch of the light mediated interaction between the membrane in the middle system [37] and the atomic system.

The mechanical part of the hybrid quantum system interacts bi-directionally with the light field. It also interacts bi-directionally with the second constituent of the hybrid system, an an atomic sample in this case. The result is a mutual coupling between the mechanical and the atomic part, mediated by the light field.
This mediated coupling approach gained more and more attention in the field of hybrid quantum systems in the past years with theoretical proposal on long-distance coupling and cooling of the mechanical oscillator [38–41], coupling and feedback cooling [42], EIT-based cooling [43], or entanglement [44]. First experimental evidence of a long-distance coupling was presented by observing a bi-directional resonant interaction between an atomic ensemble and a plain membrane [45]. Recently, sympathetic cooling of a membrane in a Fabry-Pérot cavity, a "membrane in the middle system" (MiM), to 650 mK by laser cooling the atoms was observed [46].

The goal of this thesis is to take the atom-MiM hybrid system one step further, by placing the MiM system into a cryogenic environment of 30 mK. With this precondition, it should be possible to cool the mechanical oscillator into the quantum ground state by laser cooling the atoms [40]. This is an especially promising route to the quantum ground state for low frequency mechanical oscillators, a still outstanding goal.

The MiM system in this experiment is based on a fiber Fabry-Perot cavity [47]. We chose to use a fiber-based approach as it has several crucial experimental advantages. Fibers are very well suited to work in cryogenic environments due to their low thermal conductivity and are widely deployed in atomic force microscopes [48]. No windows are required to shine external laser beams into the cryostat. This results in an excellent thermal shielding and therefore in a significantly lower base temperature. Fibers are also conveniently interfaced with the atomic side of the experiment. The coupling laser illuminates the atoms and can be coupled into the remote end of the fiber cavity in the cryostat afterwards. The atomic side of the hybrid system is a ^{87}Rb machine capable to create large Bose-Einstein condensates. A sketch of the hybrid system is shown in Figure 1.2.

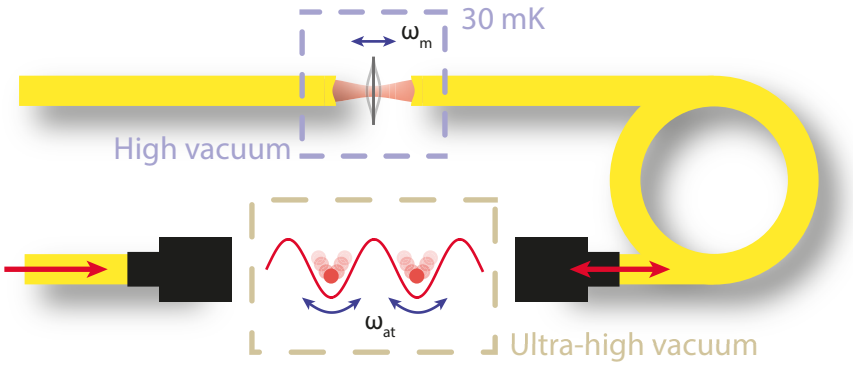

Figure 1.2: Sketch of the envisioned hybrid quantum system. A membrane with oscillation frequency ω_{m} is located in a dilution cryostat. The atomic part is trapped in an optical lattice with trapping frequency ω_{at} [40].

During this thesis, substantial work towards the realization of the hybrid quantum system was performed. The ^{87}Rb-BEC machine was planned according to the specific experimental requirements and subsequently set up. It produces large BECs at a cycle time of approximately 30 s. One crucial requirement is the capability to easily move the machine to the second laboratory at a later point in time where the cryostat is located.

Furthermore, extensive experimental and theoretical studies necessary to create fiber cavities with high reflectivity on resonance were performed. It turns out that the mode match in such an asymmetric geometry is extremely important, much more than in a symmetric fiber cavity. The inability to externally mode match fiber cavities leads to strong restrictions on the specific cavity parameters. Using these fiber cavities, a first asymmetric MiM system at room temperature was realized.

This thesis is structured as follows:

Ch. 2 – Atom-Membrane Hybrid Quantum System
This chapter describes the overall experimental setup of the hybrid quantum system consisting of a cryogenic MiM system coupled to an atomic system. After key design considerations, a short introduction to optomechanics is given, which is necessary to understand the effect of an optomechanical system on the light field. A coupling scheme according to [40] is introduced and experimental parameters are estimated. The low temperature of the dilution cryostat limits the tolerable amount of power introduced into the system due to absorption of the membrane. Estimations of the expected membrane temperatures under the influence of an external heat load are discussed.

Ch. 3 – BEC Machine for a Hybrid Quantum System
In this chapter, the cold atom part of the hybrid system is described. After an overview of the vacuum system, the magnetic fields used to trap and manipulate the atoms are presented and the used optical setups are described. In the last segment, first experimental results like the observation of Bose-Einstein condensation are presented.

Ch. 4 – Fiber Processing
This chapter discusses the fiber processing necessary to create high finesse fiber cavities. The CO_2 laser system is described and the in-house Linnik interference microscope used to analyze the processed fiber tips is discussed and validated.

Ch. 5 – Asymmetric Fibercavities
In this chapter, all the necessary ingredients to realize asymmetric fiber cavities with high reflectivity on resonance are presented. An analytical model is developed, which gives insight into the optimal cavity parameters for different applications. Furthermore, this model is validated using numerical calculations. In the last part, the experimental realization of an asymmetric fiber Fabry-Pérot cavity is presented and compared to the analytical model.

Ch. 6 – Room Temperature MiM System
In this chapter, the experimental realization of an asymmetric fiber-based MiM system is presented. The experimental setup is sketched and first measurements of key parameters such as the mechanical Q factor and the frequency shift of the cavity with respect to the membrane position are presented.

Chapter 2

Atom-MiM Hybrid Quantum System

This chapter describes the overall experimental setup of the hybrid quantum system consisting of a cryogenic MiM system coupled to an atomic system. After key design considerations, a short introduction to optomechanics is given, which is necessary to understand the effect of an optomechanical system on the light field. A coupling scheme according to [40] is introduced and experimental parameters are estimated. The low temperature of the dilution cryostat limits the tolerable amount of power introduced into the system due to absorption of the membrane. Estimations of the expected membrane temperatures under the influence of an external heat load are discussed.

With the goal to combine AMO-physics with the field of optomechanics, the first choice had to be on the atomic part of the hybrid quantum system. A cloud of atoms trapped in a magneto-optical trap (MOT) is an ideal starting point. Atoms can be loaded into the trap with high efficiency, creating a milli-kelvin sample, well isolated from the environment. Trapped atomic samples can be cooled to lower temperatures with high efficiency, using different cooling techniques [49–52]. In a magnetic or far-detuned dipole trap, a Bose-Einstein condensate can be routinely realized.
BECs and trapped atomic systems have found wide application to store quantum information [53], create entanglement between different atomic systems over a long distance [54], and to store and produce non-classical states [55, 56]. This versatility in combination with long coherence times, and the possibility to create one part of the hybrid quantum system into its many-body ground state resulted in the choice to use a BEC as the atomic side of the hybrid quantum system.

In principle, any optomechanical system can be used to create a long-distance coupled hybrid quantum system. With the large variety of optomechanical systems, spanning over 21 orders of magnitudes in mass and frequencies from Hz to GHz [57], it is cruicial to find the one system, optimally suited to couple to the atomic system.

To create a promising hybrid quantum system the following parameters are needed:

(i) Excellent incoupling into the optomechanical system. This is necessary as any loss in between the two system will degrade a coherent evolution between the two constituents.

(ii) Reflection asymmetry. The light has to be redirected to the atomic sample to create a bidirectional coupling.

(iii) A frequency suitable for resonant interaction with the atoms. It can be resonant with external or internal degrees of freedom.

(iv) The mechanical $Q = f/\Delta f_{\mathrm{FWHM}}$ of the mechanical oscillator should be as large as possible. This key parameter in optomechanics describes the decoupling of the different modes of the oscillator and, alongside others, scales the thermal decoherence rate, the coupling to the environment.

(v) The possibility to implement in a cryogenic environment. This reduces the thermal noise of the oscillator and eases the requirements to reach the ground state.

Exemplary optomechanical systems of different types with decreasing mass are: suspended macroscopic mirrors [58], suspended micro mirrors, trampoline resonators [59], micromechanical membranes [37], whispering gallery mode resonators [11], microsphere resonators [60], photonic crystal structures [6], and nanorods [61].

Evaluating (i) with respect to these systems, whispering gallery mode resonators, microsphere resonators, and photonic crystal resonators are commonly coupled using the evanescent light of a tapered fiber [62]. This severely limits the incoupling efficiency, making theses systems unusable. The interfacing of fibers with photonic crystal oscillator was only recently realized. A tapered fiber was used to couple into a waveguide which is evanescently coupled to the photonic crystal at 1550 nm [63] and [64, 65]. In contrast, Fabry-Pérot cavities with moving end mirrors or MiM systems can achieve perfect mode match.

To realize directional coupling (ii), a finite reflectivity on resonance is necessary. In Fabry-Pérot cavities, this can easily be achieved using different mirror reflectivities. Whispering gallery mode resonators and microsphere resonators are not suited as they are intrinsically symmetric and based on total reflection at the edge of the resonator. Photonic crystal structures might have the possibility for finite reflectitiy on resonance but no experimental realization has been presented yet.

To achieve resonant interaction (iii), the frequencies of the oscillator have to match the atomic frequencies. External degrees of freedom can range from 1 Hz in a magnetic trap to several hundreds of kHz in optical lattices. Coupling to internal states can be realized between the m_f-states, tunable by a magnetic field up to several Mhz for ^{87}Rb or in the 6.2 GHz between $F = 1$ and $F = 2$.

With respect to the frequency, a lot of oscillators are suitable, especially when coupling to internal states. The high frequency oscillators would need to be tailored to match the 6.2 GHz splitting, whereas fine adjustment can be done with a magnetic field.

A large optomechanical Q (iv) is desirable. Of whispering gallery mode type, bottle resonators exhibit exceptionally high Q of $Q = 1 \times 10^8$ [66], closely followed by high stress micromechanical membranes with $Q = 5 \times 10^7$ [67]. Fabry-Pérot cavities with movable end mirror are limited with respect to Q. A good reflectivity, which requires layers of materials with different refractive index, and a high mechanical Q has to be combined in one device. Hence any defects affect the mechanical Q, a tradeoff between reflectivity and Q is often necessary [68–70].

Cryogenic implementation (v) can be realized with most of the microscopic optomechanical systems. Windows can be used to bring light into cryogenic environments, but limit the achievable base temperature due to increased black-body radiation. This effect becomes more critical the lower the base temperature of the system is. For the 30 mK system here, this is a delicate problem. Fibers are better suited and widely used in low temperature atomic force microscopes [48, 71]. The bad thermal conductivity leads to a small thermal path from room temperature to the cryogenic environment, enabling a low base temperature in the cryostat.

Taking all these considerations into account, we decided to use an asymmetric fiber-based MiM system as the optomechanical part of the hybrid quantum system. It is the only system that complies with every requirement and is ideal to implement in a cryogenic environment. No system of this type is reported in the literature yet. Only symmetric, room temperature fiber-based MiM systems are reported [61, 72–74]. Cryogenic implementation of MiM systems based on free space cavities were presented for 400 mK [75], 1 K [18], and 5 K [19].

Another benefit of the MiM system is the possibility to quickly change the oscillator type. It is not only a membrane in-the-middle system, it can be an "oscillator in-the-middle" system. Possible are sub-wavelength, low mass nano mechanical oscillators [61, 76] (carbon nanotubes or nanowires) or larger micromechanical membranes of different materials. Examples are:

- Si_3N_4, low absorption ($\mathrm{Im}(n) \lesssim 2 \times 10^{-5}$ at 780 nm [77]), high mechanical Q (5×10^7 [67]), widely employed in MiM systems;
- SiO, very low absorption ($\mathrm{Im}(n) \approx 2 \times 10^{-7}$ [78]), unknown mechanical Q;
- graphene, high mechanical Q (1×10^5 [79]) but high absorption (2.3 % [80]);
- hexa-Boron nitride, should have mechanical Q comparable to graphene but lower optical absorption, as it is a wide-bandgap insulator.

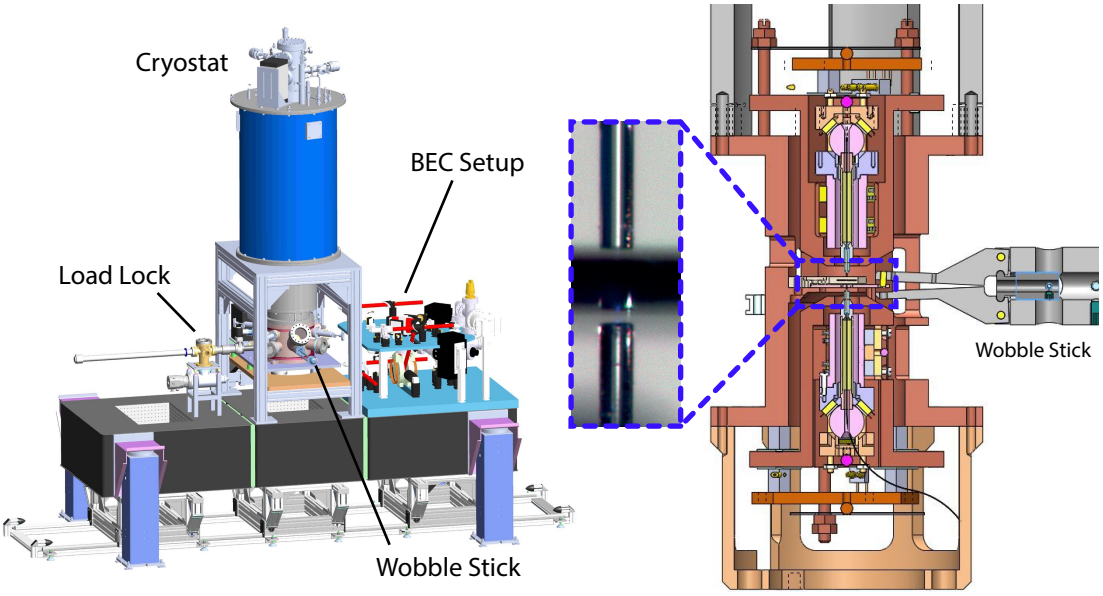

Figure 2.1: **Left:** CAD drawing of the combined system. **Right:** CAD drawing of the fixe-axis goniometers later on used in the cryostat and an image of two fibers positioned by the goniometers close to a Si_3N_4 membrane under ambient conditions.

The small waist in fiber cavities allows the use of very small and light membranes. The only downside in MiM systems, residual absorption of the membrane and subsequent heating, does not limit the ability to cool to the ground state or create entanglement [81]. Note that an asymmetric cavity can be used from both sides, which is also intended here. Different beams, for example a PDH locking beam, will be coupled from the higher reflecting side (see Section 6.2).

2.1 Experimental Setup

Both parts of the hybrid quantum system will be located next to each other on a single damped optical table. The laboratory has excellent passive vibration properties and was originally built to house a scanning probe microscope suitable for low-noise atomic resolution experiments. A CAD drawing of the combined setup is shown in Figure 2.1.

The MiM system will be located in a UHV compatible dilution refrigerator with a minimal base temperature of 30 mK at the mixing chamber and a cooling power of 560 µW at 100 mK, manufactured by Oxford Instruments. It is custom designed to realize a high cooling power using two continuos heat exchangers. Furthermore, great care was taken to avoid vibrations in the system by placing all external pumps in a neighboring room. In contrast to the pulsed-tube cryostats, which are often used, our system should exhibit a much lower vibrational noise level as no internal pulsed pumps to re-liquify the ^{4}He are used. This is done externally, the cryostat is refilled with liquid ^{4}He. Mechanical decoupling of the pulsed-tube cryostat and the sample to reduce vibrations is possible but very difficult [69]. It is better to avoid the vibrations in the first place.

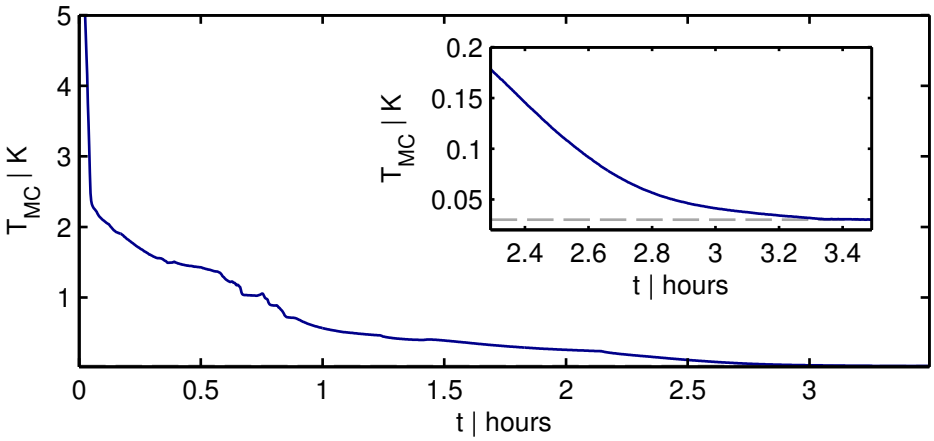

Figure 2.2: Temperature at the mixing chamber during a cooldown to the base temperature of 30 mK, indicated as the dashed gray line. The inset is a magnification of the mixing chamber approaching the base temperature. The temperature was measured with a calibrated RuO sensor.

To align the MiM system in the cryostat, the fibers are mounted in novel five-axis goniometers [82], which were developed at this project. All axes are based on inertial stepper motors using shear piezos, a technique commonly used in AFM systems. This approach is much better than often applied Attocubes, which are very lackluster in terms of vibrations [69]. A total of 16 piezos (θ, ϕ: 2, z: 6, x, y: 3) per goniometer are used and allow for milli-degree $\theta\varphi$- and nanometer xyz-accuracy. The goniometers are already tested under ambient conditions [82] and, based on experience in low temperature scanning probe microscopes, we are confident that they will perform well under cryogenic UHV conditions.
In the cryostat, the mechanical oscillator will be fixed onto a shuttle that can be removed from the MiM system after retracting the fiber ends. This shuttle can be removed from the vacuum using a wobble stick with a pincer and a transfer bar to bring it into the load lock chamber (see Figure 2.1). Therefore, the mechanical oscillator in the MiM system can be quickly exchanged without breaking the vacuum or heating up the whole system. The wobble stick can also be used to manipulate shutters in the radiation shields of the cryostat. Once the membrane is placed in the cavity and the cavity aligned using long working distance microscopes and the reflection signal, the shutters can be closed to reduce the external thermal load to a minimum.

The dilution cryostat is already tested and is capable to reach the base temperature of 30 mK. A cooldown sequency is shown in Figure 2.2. In this measurement, the goniometers were not yet mounted on the mixing chamber and the radiation shields completely closed. The expected base temperature with attached goniometers and closed shutters will be slightly higher due to the additional thermal load (wiring, optical fibers). Further details on the cryostat will be presented in a following thesis.

2.2 Optomechanics

To understand the interaction of the hybrid quantum system, it is important to understand how the optomechanical part of the hybrid system interacts with the light field. This type of interaction is universal to the large variety of optomechanical systems. Some basic optomechanical properties important for the presented design are introduced here. For a review of the field, the reader is referred to the reviews [57, 83, 84] and the recent textbook [22].

A typical optomechanical system consists of a light mode ω_{cav} and a mechanical mode Ω_{m}. This corresponds to a Hamiltonian $\hat{H}_0$ of the form [83]

$$\hat{H}_0 = \hbar\omega_{\mathrm{cav}}\hat{a}^\dagger\hat{a} + \hbar\Omega_{\mathrm{m}}\hat{b}^\dagger\hat{b}. \tag{2.1}$$

For the case of dispersive optomechanics, the resonance frequency of the cavity mode ω_{cav} changes with respect to the position of the mechanical oscillator.

$$\omega_{\mathrm{cav}}(x) \approx \omega_{\mathrm{cav}} + x \cdot \frac{\partial\omega_{\mathrm{cav}}}{\partial x} + \dots \tag{2.2}$$

The optical frequency shift per displacement is defined as $G = -\partial\omega_{\mathrm{cav}}/\partial x$. Inserting $\omega_{\mathrm{cav}}(x)$ into the Hamiltonian and writing $\hat{x}$ in terms of the zero point motion

$$x_{\mathrm{ZPM}} = \sqrt{\frac{\hbar}{2m_{\mathrm{eff}}\Omega_{\mathrm{m}}}} \tag{2.3}$$

of the oscillator as $\hat{x} = x_{\mathrm{ZPF}}\left(\hat{b} + b^\dagger\right)$, the full hamiltonian can be written in the form [83]

$$\hat{H}_0 = \hbar\omega_{\mathrm{cav}}\hat{a}^\dagger\hat{a} + \hbar\Omega_{\mathrm{m}}\hat{b}^\dagger\hat{b} - \hbar g_0\hat{a}^\dagger\hat{a}\left(\hat{b} + \hat{b}^\dagger\right). \tag{2.4}$$

The parameter $g_0 = G \cdot x_{\mathrm{ZPM}}$ is the vacuum optomechanical coupling strength. It is the interaction between a single photon and a single phonon.

A simple realization of such a scheme is a Fabry-Pérot cavity with a movable end mirror. The resonance condition of the Fabry-Pérot cavity is fulfilled if $n\lambda_n = 2L$ with a respective resonance frequency of $\omega_{\mathrm{cav}} = n\pi c/L$. A displacement of the movable end mirror changes the cavity length L. The resulting, position-dependent, cavity frequency $\omega_{\mathrm{cav}}(x)$ can be written as

$$\omega_{\mathrm{cav}}(x) = \frac{n\pi c}{L + x} \approx \omega_{\mathrm{cav}}\left(1 - \frac{x}{L}\right) = \omega_{\mathrm{cav}} - x \cdot \frac{\omega_{\mathrm{laser}}}{L}. \tag{2.5}$$

The frequency shift per displacement G for a Farby-Pérot cavity is therefore

$$G = \frac{\omega_{\mathrm{laser}}}{L}. \tag{2.6}$$

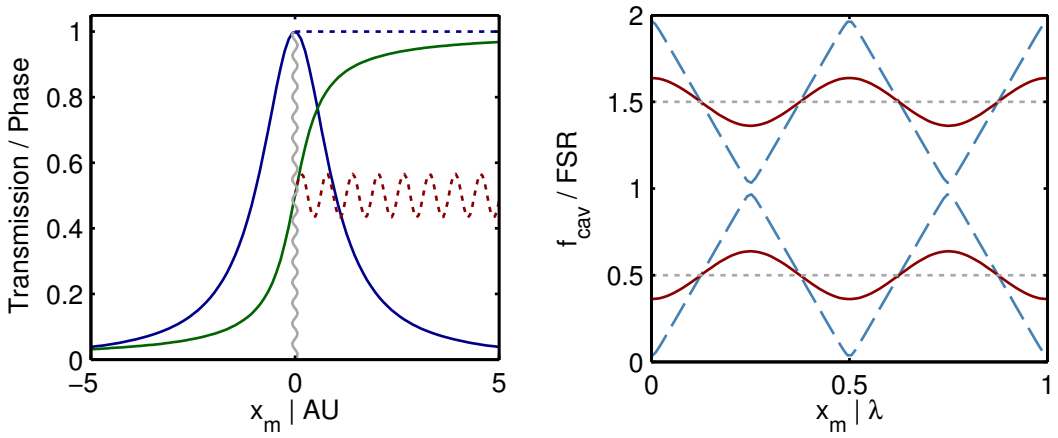

Figure 2.3: **Left:** Sketched effect of the oscillator motion shown in the vertical gray line. Shown in blue is the transmission of the Fabry-Pérot and the phase of the transmitted light in red. Effect of the oscillator motion on the transmission and phase of the light is shown as a dotted line with the respective color. **Right:** Shift of the cavity resonance for a membrane in the middle system with field reflectivity $r_m = 0/0.42/0.995$ in dotted/solid/dashed.

Figure 2.3 depicts the general behavior of such an optomechanical system. Depending on the position of the oscillator, the cavity can be tuned in and out of resonance as $\omega_{\mathrm{cav}} = \omega_{\mathrm{cav}}(x)$. The phase of the transmitted light through the cavity has a maximal slope at the resonance position. If the cavity is locked to the laser with a bandwidth smaller than the oscillator frequency, the movement of the mechanical oscillator is not affected by the lock and its motion mapped to phase oscillations of the light transmitted through the cavity. These phase oscillations can be analyzed with high precision using homodyne detection to detect and manipulate the motion of the oscillator [10].

2.2.1 Membrane in the Middle

The optomechanical system under study here, a MiM system, behaves similar to a Fabry-Pérot cavity with a moving end mirror. It can be described by the same Hamiltonian but with a modified coupling G. Due to the standing wave structure in the Fabry-Pérot cavity, G has a more complex structure [37, 85, 86] that is periodic with the position of the membrane:

$$\omega_{\mathrm{cav}}(\Delta x) = \nu_{\mathrm{FSR}}\left(2\phi_r + 2\arccos\left(|r_m|\cos\left(2k\cdot\Delta x\right)\right)\right). \tag{2.7}$$

Here, $\nu_{\mathrm{FSR}} = c/2L$ is the free spectral range of the cavity. The membrane has a field reflectivity r_m and is located in the center of a cavity with length L. ϕ_r is the constant phase shift introduced by the membrane, $k = 2\pi/\lambda$ the wavenumber and Δx the position of the membrane in the cavity. Dependent on the position of the membrane in the intra cavity field, a linear optomechanical coupling at the slope of the cavity field ($x_m = 0.125\lambda$) or quadratic coupling at the maxima/minima of the field ($x_m = 0.25\lambda$ / $x_m = 0$) is possible [9], necessary for QND type interactions. As expected, the derivative of equation 2.7 collapses to equation 2.6 for $r_m = 1$ with a new cavity length $L = L/2$.

2.3 Coupling to External Degrees of Freedom

A interesting proposal to couple an atomic sample and a membrane was published in 2010 [38], later expanded [40], and experimentally realized [46] with a room temperature MiM system. It is based on the coupling of a mechanical oscillator to the center of mass motion of a cloud of atoms, trapped in an optical lattice.

This well known technique in the cold atoms community is based on the dipole force [87]. The optical lattice can be created by retroreflection of a laser beam. The interference of the two counter propagating beams with amplitude E_1 and E_2 creates a lattice potential with $\lambda/2$-spacing:

$$(E_1 + E_2)(E_1^* + E_2^*) = V_0 \cos(kx)^2 . \tag{2.8}$$

In harmonic approximation, valid in the deep lattice, an atom trapped in a lattice minimum experiences a potential

$$V = \frac{1}{2} m_{\mathrm{at}} \omega_{\mathrm{at}}^2 x_{\mathrm{at}}^2 \tag{2.9}$$

with trapping frequency ω_{at}. If the atom is displaced from the minimum, it experience the restoring dipole force

$$F_{\mathrm{dipole}} = -\frac{\partial V}{\partial x_{\mathrm{at}}}. \tag{2.10}$$

This restoring force not only has an effect on the atom, it also affects the amplitude of the light fields E_1 and E_2, which create the lattice [88, 89]. Microscopically, the dipole force can be expressed as a stimulated redistribution of photons between the two counter propagating modes with $\pm\hbar k$ creating the lattice. If a momentum of $2\hbar k$ is transferred to the atom, one photon with $+\hbar k$ is absorbed and reemitted in the $-\hbar k$ mode. This results in a power modulation of the lattice light with the trapping frequency ω_{at} caused by the atomic sample.

To create an interaction between the atoms and a mechanical oscillator, an asymmetric MiM system is used instead of a fixed mirror, to create the optical lattice [40]. The mechanical oscillator is susceptible to changes in the radiation pressure and therefore affected by the motion of the atoms. A resonant interaction is possible if the trapping frequency of the atoms in the lattice ω_{at} matches the resonance frequency of the optomechanical system ω_{m}.

Not only the oscillator is affected by the light, the motion of the oscillator also affects the atoms trapped in the lattice. A Fabry-Pérot cavity has a reflection minimum on resonance and a phase slope of the reflected field as, similar to Figure 2.3. If the cavity length is changed, the resonance frequency shifts as mentioned above. This also affects the phase of the reflected beam. The fields creating the lattice are now $E_1 = E_{01}\exp(i(kx))$ and $E_2 = E_{02}\exp(i(-kx + \varphi))$. As the phase φ of the reflected light depends on the position of the mechanical oscillator δx_{m}, the location of the lattice minima also depend on δx_{m}. The optical potential can then be expressed using the linear approximation

$$\varphi(\delta x_{\mathrm{m}}) \approx \frac{\mathrm{d}\varphi}{\mathrm{d}x} \cdot \delta x_{\mathrm{m}} = \frac{8\mathcal{F}}{\lambda} \cdot \delta x_{\mathrm{m}} \tag{2.11}$$

as

$$(E_1 + E_2)(E_1^* + E_2^*) = V_0 \cos\left(kx - \varphi(\delta x_\mathrm{m})/2\right)^2 \tag{2.12}$$

$$= V_0 \cos\left(kx - \frac{4\mathcal{F}}{\lambda} \cdot \delta x_\mathrm{m}\right)^2 . \tag{2.13}$$

Here, the expression for the phase slope of a cavity with perfect asymmetry with a reflectivity on resonance of one is used. This expression is derived in Section D.3 of the appendix.

To summarize: If the cavity length changes with frequency ω_m, the phase of the reflected light is affected and the position of the lattice minima oscillate with ω_m. The displacement of the atoms in the lattice affect the power of the beam behind the atoms, hence affecting the oscillator due to change in radiation pressure. This gives an idea of the coupling mechanism from the optomechanical system to the external degree of freedom of the atoms as proposed in [40].

2.3.1 Experimental Parameters

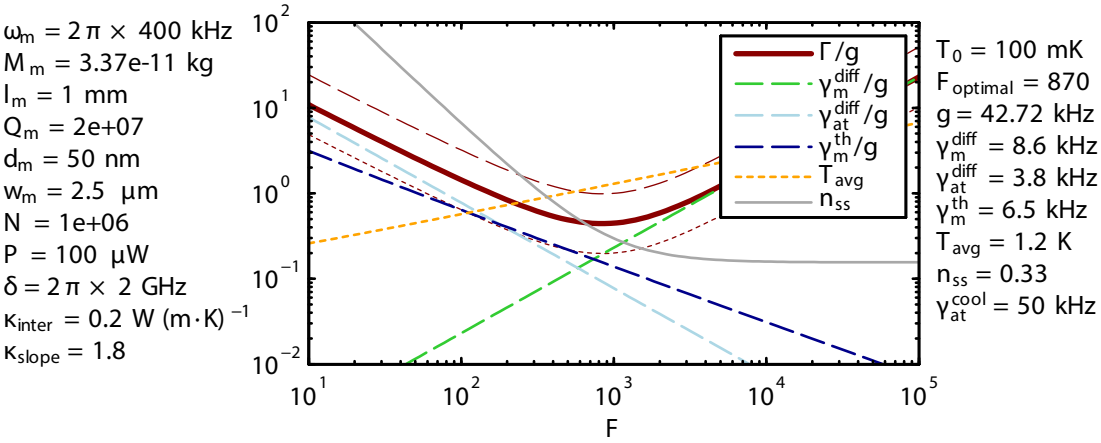

Figure 2.4: Experimental parameter for the coupling to external degrees of freedom according to the model presented in [40]. Shown are the decoherence rates as described in the text relative to the coupling strength g. The parameter Γ is the sum of all decoherence rates. The thin dashed/dotted lines correspond to a decrease/increase of the atom number N by a factor of five. Furthermore the average temperature T_avg is shown, here the vertical axis is given in K. In gray is the expected steady state occupation number if the atomic system is cooled with the rate $\gamma_\mathrm{at}^\mathrm{cool}$.

The coupling to the motional degree of freedom illustrated above can be described according to [40] by the effective hamiltonian

$$H_\mathrm{eff} = \hbar\omega_\mathrm{m} a_\mathrm{m}^\dagger a_\mathrm{m} + \hbar\omega_\mathrm{at} a_\mathrm{at}^\dagger a_\mathrm{at} - \hbar g x_\mathrm{m} x_\mathrm{at} \tag{2.14}$$

with the corresponding on-resonance ($\omega_{\mathrm{at}} \approx \omega_{\mathrm{m}}$) coupling strength

$$g = \omega_{\mathrm{at}} |r_{\mathrm{m}}| \frac{2\mathcal{F}}{\pi} \sqrt{\frac{m_{\mathrm{at}} N}{m_{\mathrm{m}}}} \tag{2.15}$$

of the mechanical oscillator and the atoms. A few things are to note here. First of all, this is a linearized description of the system. The parameter g is a result of the coupling between the mechanical system and the light field g_{m}, and the coupling of the atoms to light field g_{at} and a subsequent adiabatic elimination of the light field. Also, the atomic ensemble in the lattice is treated as individual, separated atoms. This can be seen in Equation 2.15, as in the coupling strength g, the mass of the atoms is scaled by the number of atoms in the lattice N.

To achieve a strong coupling between the membrane, the coupling g has to be larger than the sum of all decoherence rates [40]

$$g > \Gamma = \gamma_{\mathrm{m}}^{\mathrm{diff}} + \gamma_{\mathrm{at}}^{\mathrm{diff}} + \gamma_{\mathrm{m}}^{\mathrm{th}}. \tag{2.16}$$

Here, the membrane diffusion rate $\gamma_{\mathrm{m}}^{\mathrm{diff}}$ [40] describes the radiation pressure noise originating from the intra-cavity field:

$$\gamma_{\mathrm{m}}^{\mathrm{diff}} = \frac{4P}{m_{\mathrm{m}} c^2} \frac{\omega_{\mathrm{L}}}{\omega_{\mathrm{m}}} |r_{\mathrm{m}}| \left(\frac{2\mathcal{F}}{\pi}\right)^2. \tag{2.17}$$

This diffusion rate is a fundamental limit in optomechanical systems and was recently observed [90]. Here, ω_{L} is the laser frequency and P the power incident on the cavity.

The thermal decoherence rate of the membrane $\gamma_{\mathrm{m}}^{\mathrm{th}}$ describes the coupling to a thermal reservoir with temperature $T = T_0 + \delta T$ and is given by [40]

$$\gamma_{\mathrm{m}}^{\mathrm{th}} = \gamma_{\mathrm{m}} \frac{k_{\mathrm{b}} (T_0 + \delta T)}{\hbar \omega_{\mathrm{m}}}. \tag{2.18}$$

The atoms are affected by the momentum diffusion rate $\gamma_{\mathrm{at}}^{\mathrm{diff}}$ [91]

$$\gamma_{\mathrm{at}}^{\mathrm{diff}} = \frac{(k_{\mathrm{L}} l_{\mathrm{at}})^2 \gamma_{\mathrm{se}} V_0}{\hbar |\delta|}, \tag{2.19}$$

where γ_{se} is the linewidth of the transition, δ the detuning with respect to the atomic resonance, l_{at} the zero point motion of the atoms in the lattice potential and k_{L} the laser wave number.

These decoherence rates are summarized in Figure 2.4, which shows the calculated rates relative to the coupling rate g for the input parameters shown on the left. The strong coupling condition $\Gamma/g < 1$ is fulfilled for reasonable experimental parameters. The finesse of $\mathcal{F} = 870$ is easy realizable in asymmetric cavities. A reflectivity of $R_1 = 0.993$

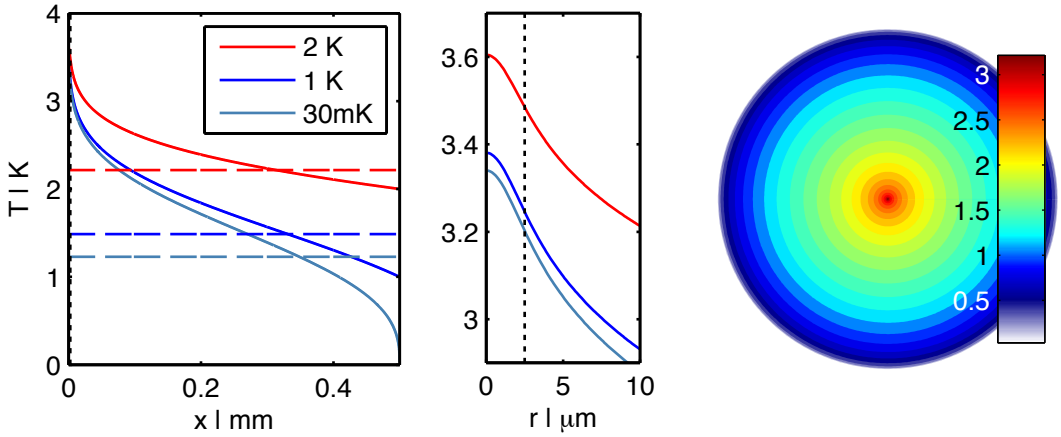

Figure 2.5: **Left:** Radial temperature dependence of a Silicon Nitride membrane for three different bath temperatures T_0. The dashed lines correspond to the average temperature. The vertical dotted black line is the waist size of beam heating the membrane. Power and absorption are as specified in Figure 2.4. **Center:** Magnified view of the temperature in the center. **Right:** Surface plot of the 30 mK temperature distribution.

and $R_2 = 0.9998$ would lead to $\mathcal{F} = 870$ and a reflectivity on resonance of 0.9.

It is also possible to cool the membrane by laser cooling the atoms trapped in the lattice with the rate $\gamma_{\mathrm{at}}^{\mathrm{cool}}$. The corresponding steady-state mode occupancy n_{ss} [40]:

$$n_{\mathrm{ss}} \approx \frac{\gamma_{\mathrm{m}}^{\mathrm{th}} + \gamma_{\mathrm{m}}^{\mathrm{diff}}/2}{\gamma_{\mathrm{m}} + \Gamma_{\mathrm{cool}}} + \left(\frac{\gamma_{\mathrm{at}}^{\mathrm{cool}}}{4\omega_{\mathrm{at}}}\right)^2 + \frac{\gamma_{\mathrm{at}}^{\mathrm{diff}}}{2\gamma_{\mathrm{at}}^{\mathrm{cool}}}, \tag{2.20}$$

with the sympathetic cooling rate Γ_{cool} [40]:

$$\Gamma_{\mathrm{cool}} = \frac{g^2}{\gamma_{\mathrm{at}}^{\mathrm{cool}}} \frac{1}{1 + \left(\gamma_{\mathrm{at}}^{\mathrm{cool}}/4\omega_{\mathrm{m}}\right)^2}, \tag{2.21}$$

is also included in Figure 2.4. As $n_{\mathrm{ss}} < 1$ and $\Gamma/g < 1$ is achievable at the same finesse, it should be possible to cool the membrane into the quantum ground state by laser cooling the atoms. Switching off the cooling leads to coherent evolution of the system. In contrast to the experimental parameters given in [40], we

- used lower, more realistic, thermal conductivity κ, discussed in A.1;
- used the complete analytical solution for the temperature distribution of the membrane based on a gaussian heat source and a temperature dependent $\kappa(T) = \kappa_{\mathrm{intercept}} T^{\kappa_{\mathrm{slope}}}$, rather than the flat top approximation and $\kappa = \kappa(T_0)$ used in [40]. This is derived and discussed in A.2, the result is shown in Figure 2.5;
- used a lower number of interacting atoms, in the range of the recent experimental realization [46];
- used a lower cooling rate $\gamma_{\mathrm{at}}^{\mathrm{cool}} = 50\,\mathrm{kHz}$ of the atom in the lattice, rather than $\gamma_{\mathrm{at}}^{\mathrm{cool}} = 220\,\mathrm{kHz}$ as used in [40];

- used the average temperature of the membrane as a more realistic approximation of the expected mode temperature. This is discussed in a bit more detail below.

If a mechanical oscillator has a constant temperature, the bath temperature T_0, the mode temperature is identical to the bath temperature. The oscillator moves according to the equipartition theorem $kx_{\mathrm{rms}}^2 = k_{\mathrm{b}}T_0$. In contrast, for a oscillator with a non-constant temperature, it is not initially clear how the temperature distribution is connected to the mode temperature. According to the model presented in [92], which connects the temperature distribution to the effective temperature of an oscillating cantilever, the temperature close to the clamped edge is more important than at the loose end. The cantilever is modeled as a sum of short segments, each one oscillating with the corresponding amplitude x_{rms} to the respective temperature of the segment. A high temperature at the clamped end leads to a large oscillation of the whole cantilever due to the large lever. A similar argument should hold true for a doubly clamped beam and a membrane. Hence, the average temperature seems to be a more reasonable choice to use for the mode temperature, rather than the center temperature as used in [40].

2.4 Coupling to Internal Degrees of Freedom

Other coupling schemes we want to realize rely on a coupling of the mechanical motion to internal degrees of freedom rather than to external degrees of freedom. Such a system could be realized using Faraday rotation [93] in the Λ-level scheme available in ^{87}Rb, is sketch in Figure 2.6.

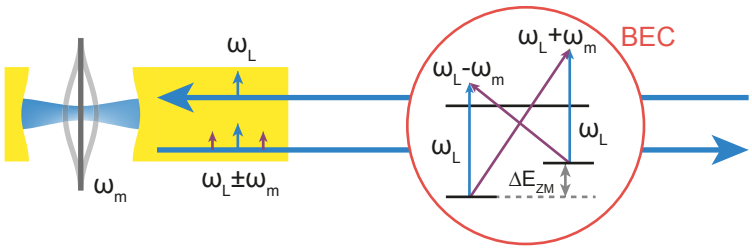

Figure 2.6: Scheme for coupling the motion of the membrane to atomic hyperfine degrees of freedom via Faraday rotation. The mechanical oscillator has a frequency ω_{m}, and imprints sidebands of the lightfield (ω_{L}). The atomic resonance can be tuned by ΔE_{ZM} using a magnetic field.

The sidebands created by the motion of the oscillator on the reflected light couple two internal states. The polarization of the light that is transmitted through the atoms is affected by the Faraday effect. This can be mapped to intensity modulation at the membrane if a polarization dependent element is introduced in the beam path. A Faraday angle of 10° with cold, but still thermal, atoms was realized using ^{87}Rb [94]. As the Faraday angle is dependent on the optical density rather than the particle number, a BEC is ideal for this type of interaction. Changing the applied magnetic field would allow to bring the atomic system in resonance with the membrane over a wide range of

frequencies from the kHz up to the MHz regime. A repumping laser could be used to depopulate the higher energy state thus removing energy and therefore cooling the system.

The possibility to realize long distance entanglement using internal states via the scheme proposed in [44] is also an intriguing idea. The basic principle behind this idea is entangling collective spin variables of the atomic medium with the nano-mechanical oscillator via a QND measurement. One major benefit of this scheme is that even if atoms and oscillator are not cooled to the ground state, the system will be projected in a pure entangled state by the QND measurement in the strong coupling limit. Beyond that, the use of a BEC opens up additional fascinating prospects. One possibility would be to use a spin-orbit coupled BEC [95], which would allow swapping the entangled excitations from the spin to the spatial excitations of the BEC. From this perspective an intriguing question is to which degree such an ensemble of atomic 2-level systems can be used as a quantum state analyzer for the state of the membrane. Thereby, the internal atomic states can be detected by a Stern-Gerlach time-of-flight measurement [96] or in a quantum non demolition (QND) measurement based on Faraday rotation. The spatial excitations can be recorded via traditional absorption imaging of the momentum distribution after time-of-flight. Vice versa, excitations in the atomic system can in principle be transferred to the membrane and back in a Rabi oscillation-like fashion. Such an observation would be a direct proof for coherent coupling between an atomic and a nano-mechanical system.

Very recently, a full quantum theory on the coupling to internal states over a long distance was presented [41]. Similar to [40], it should be possible to cool the mechanical oscillator its motional ground state by laser-cooling the atoms.

Chapter 3

BEC Machine for a Hybrid Quantum System

In this chapter, the cold atom part of the hybrid system is described. After an overview of the vacuum system, the magnetic fields used to trap and manipulate the atoms are presented and the used optical setups are described. In the last segment, first experimental results like the observation of Bose-Einstein condensation are presented.

The element used for the atomic side of the hybrid quantum system is ^{87}Rb. As mentioned in Section 2.3, the interaction of the hybrid quantum system scales with the number of particles. The goal of the machine was to quickly produce large MOTs and BECs in a robust way. This is realized in a 2D/3D MOT geometry [97]. This setup enables high vapor pressures in the 2D MOT and therefore high loading rates of the 3D MOT while still maintaining the excellent background pressure conditions in the 3D MOT region.

3.1 Vacuum System

The vacuum system consists of two main parts as sketched in Figure 3.1. In a 2D MOT glass cell located above the central chamber, Rubidium is pre-cooled and transferred by a pushing beam through a differential pumping tube into the 3D MOT glass cell, located below the chamber, where the atomic beam is captured by a large volume 3D MOT. Here, after a molasses phase and transfer to a magnetic trap, a Bose-Einstein condensate is produced by radio frequency evaporation [98–100]. A pressure of $p < 1 \times 10^{-11}$ mbar ensures that the lifetime of the BEC is not limited by collisions with background gas [101] and is therefore the goal of this setup. A central chamber of the same design as implemented here is already in use in several other experiments in our group [102–105], and has proven over the years to be a reliable starting point for the setup of new quantum gas vacuum systems for various atomic species. The latest evolutionary version which is also used here was built during the thesis of Sören Dörscher [102]. All other parts were designed to optimally fit the needs of this particular experiment. Among these are the

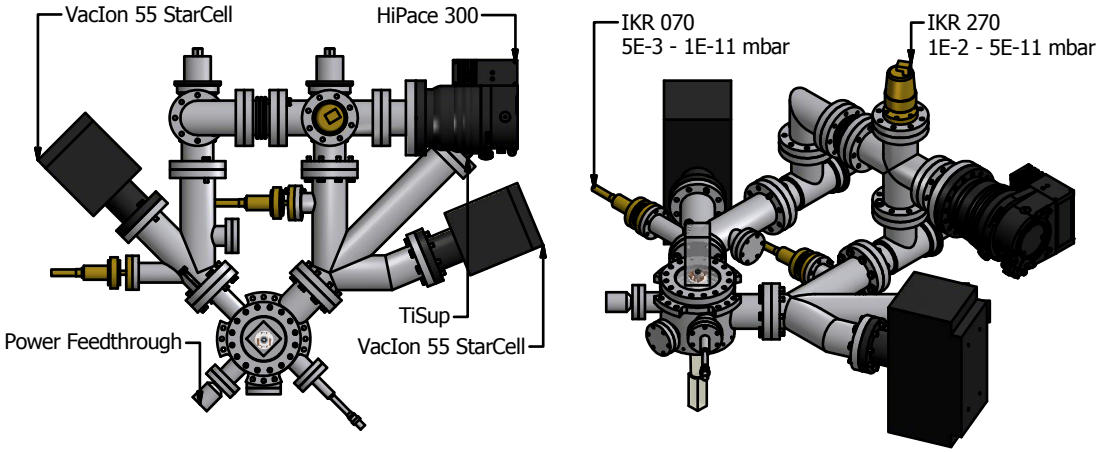

Figure 3.1: CAD drawing of the vacuum system. Two glass cells, one for the 2D MOT (upper cell) and one glass cell for the 3D MOT (lower cell) are mounted to a central chamber. Attached to the chamber are two pump arms, one for the 2D MOT (left pump arm) with a gauge and IGP, the other for the 3D MOT with a gauge, IGP and TiSup. Both arms are connected via angle valves to a turbo pump.

need for a compact setup, as the vacuum system is to be moved to another lab later on. The system is therefore setup onto a 1.1 m × 1.1 m breadboard, exactly fitting the spatial requirements of the new laboratory.

All full metal vacuum parts, except the valves, were vacuum baked prior to the assembly at 1200 °C by Pfeiffer Vacuum. The is done to remove residual gas and contaminations from inside of the steel. This contamination is a result of the manufacturing process and does not reenter the steel after the vacuum bakeout resulting in a faster progression to the desired base pressure.

3.1.1 Glass Cells

In contrast to a chamber with windows, glass cells enable a larger optical access and are much more compact. The 2D MOT cell is a 50 mm × 50 mm × 120 mm cell made from Spectrosil 2000 fused silica glass. The bottom ring is made out of Viteosil and is connected to the central chamber with two Helicoflex gaskets. These are spring loaded aluminum "c" rings which can seal polished surfaces when compressed. The cell is coated on the outside with a broadband AR coating. For more detail on the mounting of the glass cell see the thesis of Sören Dörscher [102].
In contrast to the 2D MOT cell, the 3D MOT cell is mounted to the vacuum chamber with a CF 35 flange. The flange is connected with a metal-to-glass transition to a glass tube that ends in the rectangular glass cell. The total length from flange to the cell end is 100 mm, the glass cell itself has a outer dimension of 80 mm × 26 mm × 26 mm with 3 mm thick walls. All outer surfaces are treated with an anti reflective coating from 500 nm to 1100 nm, specified with $< 1\%$ for the side and $< 2.2\ \%$ for the bottom of the cell.

3.1.2 Pump Arms

Attached to the central chambers are two pump arms with ion getter pumps[1] (IGPs) and gauges for both the 2D and 3D MOT. The pump arms are designed for the pumps to be as close as possible to the vacuum chamber to provide maximum pumping speed. A titanium sublimation pump[2] with three filaments is mounted in the 3D MOT pump arm[3]. This pump can be fired occasionally to coat the inside of the tube with titanium, a potent getter material. It provides additional pumping rate necessary to reach the low 10^{-11} mbar regions. For pre-pumping, both pump arms are connected via full metal angle valves to a single turbo molecular pump[4].

3.1.3 Differential Pumping Tube

The differential pumping tube actually consists of two separate graphite tubes. The upper part is a cylindrical tube and the aforementioned 2D MOT IGP pumps the 2D MOT volume through this tube. By design the upper tube is capable to maintain a pressure ratio of 440 [102]. The lower tube is conical in shape to provide a larger acceptance angle for the atomic beam coming from the 2D MOT. It is by design capable to maintain a pressure ratio of 270 [102]. With dispensers active and a background pressure of the 2D MOT of $p_{2D} = 6 \times 10^{-10}$ mbar, we observe a pressure of $p_{3D} < 1 \times 10^{-11}$ mbar, which is the lowest pressure the IKR 070 gauge can measure, in the 3D MOT region. Note that the background pressure of the 2D MOT is measured after the differential pumping tube. Therefore the actual pressure in the 2D MOT cell is higher.
In contrast to the 2D MOT cell which is pumped through the upper part of the differential pumping tube, the 3D MOT cell is pumped directly by the 3D MOT IGP to achieve maximum pumping speed. A sketch of the differential pumping system is also shown in [101].

3.1.4 System Assembly

To reduce contamination, the system was carefully set up in a clean environment under flow boxes using dust free overalls. We exclusively used silver coated copper gaskets, which provide less resistance when mounting the CF components together. Each flange was bolted together and tightened using distance measurement knifes. After each roundtrip, the distance was measured and the amount of turnaround of the screws adjusted accordingly to ensure a planar compression of the gasket. The final flange distance is $\approx 0.2\,\text{mm}$. This left the possibility to still tighten it further in case of a leak. This technique worked very well and was applied in our group several times. In the case of this system assembly, no leak was measurable on any flange with a Helium leak detector. Duo-nuts were used whenever possible as they make the assembly dramatically easier.

[1] Agilent VacIon Plus 55 StarCell with Dual Controller.
[2] Agilent titanium sublimation pump with sublimation controller
[3] It is mounted on axis of the chamber flange with the idea to sputter titanium as far into the chamber and close to the 3D MOT cell as possible.
[4] Pfeiffer HiPace 300 with Agilent TriScroll 300 pre-vacuum pump

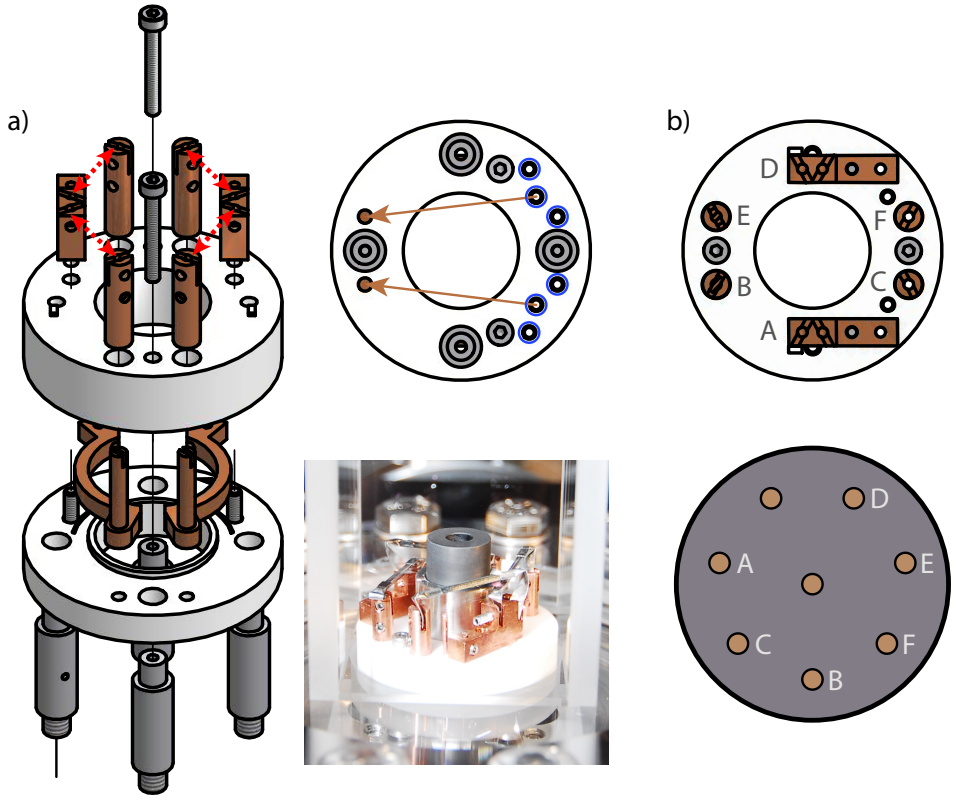

Figure 3.2: **a)** CAD drawing of the dispenser mount assembly. Visible is the two part design. The red dashed arrows indicate the position of the dispensers. **Middle:** Sketch of the internal connections and a photo of the dispenser mount inside of the 2D MOT glass cell. The blue circles indicate the positions where the feedthrough cables are connected to the dispenser mount. The arrow indicates the internal connection. The horizontal bars in the image are the rubidium dispensers, the grey tube is the upper differential pumping tube. **b)** Connections of the dispenser mount to the power feedthrough (lower circle). The upper left and central pin are not connected.

During the assembly only nitril gloves were used as even powder free latex gloves can contain residuals [106].

3.1.5 Dispenser Mount and Feedthrough

Located on the central chamber is an eight pin electrical feedthrough. Inside the vacuum chamber, six plain low-oxygen copper cable are going from the feedthrough to to dispenser mount. They are isolated with ceramic pearls tightly packed around the cables. The cables are connected to the feedthrough by push pin connectors[5]. Between the push pins, a marcor spacer is located to avoid short circuits between the large push pin connectors[6].

[5] Pfeiffer XAK015A

[6] During the installation it proved convenient to use a second pushpin on the side away of the feedthrough just to fix the ceramic pearls tightly packed on the wire. We then wiggled the cable through the hole going upwards to the 2D MOT cell. This was done for all wires. After the wires were installed, the upper pushpin and possibly additional ceramic pearls can be removed. The result is a

The dispenser mount consists of two marcor rings with copper pieces in between, which providing electrical connections. A CAD drawing is shown in Figure 3.2. The cables from the electrical feedthrough are going upwards into the 2D MOT cell from one of the holes in central chamber. The dispenser mount is designed in such a way that all the connections for the feedthrough cables are located over this hole. Therefore, no additional bending or complicated wiring inside the 2D MOT cell is necessary, which reduces the risk of short circuits. This design proved to be convenient and easy to install.

After the feedthrough and the cables are installed, the dispenser mount is pushed over the cables and fixed in its position. The cables are fixed with screws on the dispenser mount and cut to the right length. The benefit is that the cables can not be cut too short which would cause the need for a complete rewiring. After the dispenser mount is installed, four rubidium dispensers[7] are clamped with small screws in their respective mounts. The dispensers are installed in pairs of two which share on wire, therefore three wires per two dispensers. Due to the high vapor pressure of rubidium [107], the exact location and orientation of the dispensers in the 2D MOT volume is not important.
To reduce contamination of the final setup all dispensers are heated to their final operation point of $\approx 3.5\,\mathrm{A}$ prior to the system bakeout. The installed rubidium dispensers do no require a certain activation current. The preheating it is only performed to remove dirt from the dispensers and cables.

3.1.6 Bakeout

After assembly, the vacuum system was baked to achieve the desired pressures of $p < 1 \times 10^{-11}$ mbar. This was done with the glass cells already attached in contrast to other vacuum systems in our group. The obvious benefit is that there is no need to break the vacuum again, which reduces the risk of contamination by air and especially water.
It is necessary to ensure a low temperature gradient at the glass cells and the metal to glass transition of the 3D MOT cell. To enable a smooth heating sequence, four heating computers, which can be simultaneously programmed by LabVIEW, were used. The computers were used to heat the 3D MOT cell (1), the 2D MOT cell (2), the central vacuum chamber (3) and the rest of the pump lines (4). Separate resistive heaters were attached to the IGPs[8] and controlled manually with an isolating transformer.
To further ensure a careful and homogeneous heating of the whole vacuum system, the heating bands were carefully wrapped around the systems avoiding overlap and the whole setup wrapped with aluminum foil to ensure a homogeneous heating. To further protect the glass cells thick copper shields were used to ensure an equal temperature along the glass cells. The procedure to protect the 3D MOT cell was:

tightly packed and therefore isolated cable. This proved to be much easier than trying to add the pearls after the cable was installed or to install the cable with loose pearls.

[7] SAES Getters RB/NF/4.8/17 FT10+10. The dispensers contain 4.8 mg of Rb.

[8] The magnets were removed during the bake out and the IGPs were switched off. This is beneficial as the system is open during the bake out, also removing dirt from inside the IGPs

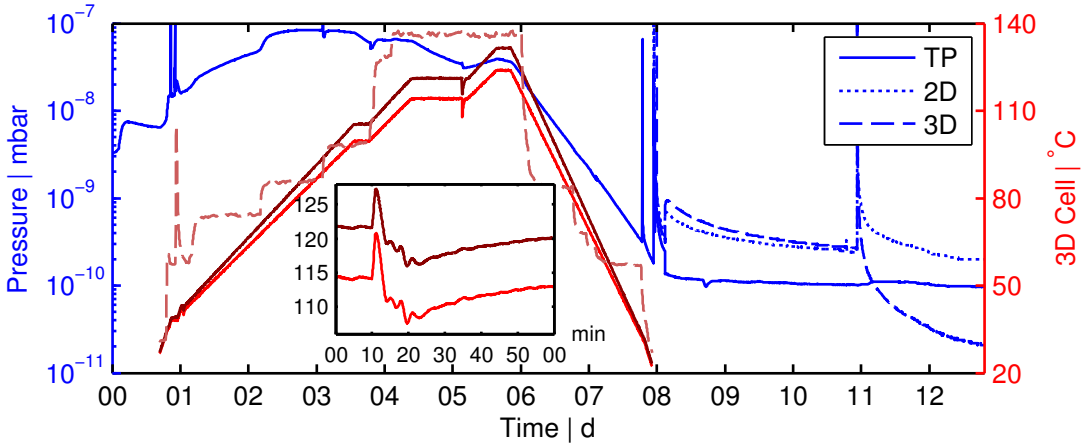

Figure 3.3: Pressures and temperature data during the bakeout procedure. Shown in blue is the pressure data of the three gauges installed in the vacuum system. The gauge located close to the turbo pump (TP), shown in solid blue, is continuously running during the bake out. The temperature data shown here are three of the total of seven sensors used to monitor the baking. The solid red lines are sensors from the top and bottom edges of the 3D MOT cell and the sensor attached to the IGP which is scaled by a factor of 0.65 (dashed red line). **Inset:** A wrong programming of the heating computer lead to a short full power heating of the whole system shortly after day five. This shows that at least our glass cell can withstand short temperature spikes quite well even though it is definitely not recommended to bake the system at such a speed.

- Tight double layer of aluminum foil.
- Rough, mashed together aluminum foil.
- Tight copper shield.
- Resistive heat band and temperature sensor.
- Many layers of aluminum foil.

The wrapping procedure for the 2D MOT cell was:

- Tight double layer of aluminum foil.
- Several layers of rough, mashed together aluminum foil.
- Resistive heat band and temperature sensor.
- Loose copper hat.
- Many layers of aluminum foil.

The bakeout sequence is shown in Figure 3.3. The system was heated over the course of five days to $\approx 120\,^{\circ}\mathrm{C}$ and cooled down over two days. The temperature sensors were externally calibrated by wrapping them together in aluminum foil, placing them in a tight metal tube and heating the tube.
After the cooldown was complete, the valves were closed, which can be seen by the sharp peak around day eight. At day eleven, the TiSup pump was fired resulting in a decrease of pressure in the 3D MOT part of the chamber by more than an order of magnitude, yielding the desired pressure of $p < 1 \times 10^{-11}\,\mathrm{mbar}$.

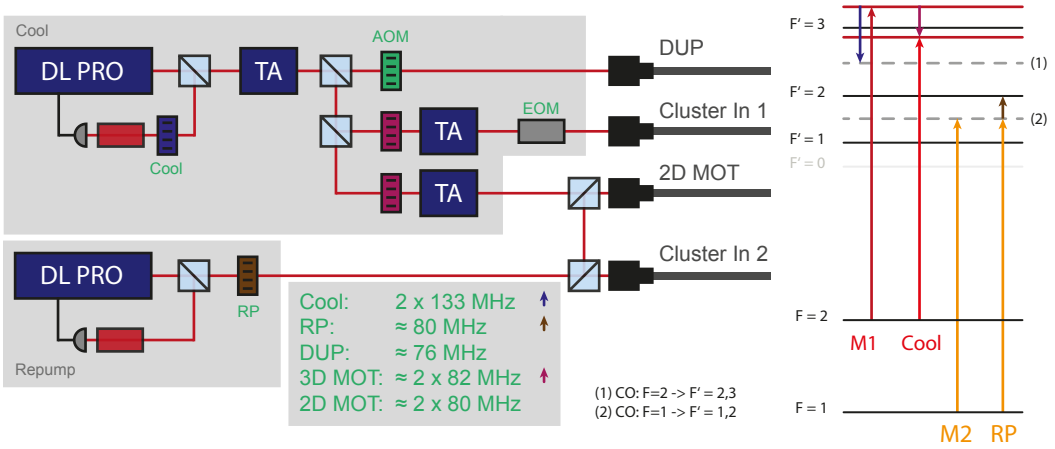

Figure 3.4: Left: Sketch of the laser system to create a ^{87}Rb Bose-Einstein condensate. It consists of two master lasers, one cooling laser and a repumping laser. Both are locked by doppler free absorption spectroscopy to crossover transitions (dashed lines on the right). The cooling laser seeds a tapered amplifier, which is subsequently split for the detection, pumping and pushing light (DUP), for the 3D MOT (Cluster Input 1) and the 2D MOT. The repumping laser is split and overlapped with the 2D MOT cooling beam and also coupled into a separate fiber for the 3D MOT (Cluster Input 2). The DUP fiber is exemplary, the detection, pumping and pushing light is each coupled into an individual fiber.

3.2 MOT Laser System

The creation of ^{87}Rb Bose-Einstein condesates requires frequency stablized cooling and repumping lasers. The laser system in use in this experiment, sketched in Figure 3.4, is based on two commercial Toptica DL Pro external cavity diode lasers (ECDL), one for the cooling, the other one for repumping. Both lasers emit around 60 mW at 780 nm.

3.2.1 Laser Lock to Rubidium

The repumping and cooling laser are locked to individual rubidium vapor cells via Pound–Drever–Hall frequency stabilization [108] using a Toptica DigiLock. The necessary sidebands are modulated onto the laser via the DC modulation input of the laser. The modulation signal is created by the DigiLock module and ranges from 1.56 MHz to 25 MHz in five steps with a maximal modulation amplitude setting of 1.9 Vpp. To ensure the sidebands are weak enough to not negatively affect the cooling of the atoms, the modulation amplitude for various modulation frequencies and modulation amplitudes was measured. (see Figure 3.5). The measurement was done with the cooling laser and a 50/50 power splitter between the modulation output of the DigiLock and the DC modulation input of the laser. Therefore the set value of the DigiLock is scaled by $1/\sqrt{2}$ in the plot. The sidebands were measured by observing the transmission through a Fabry-Perot cavity[9] on a photodiode.
In the experiment, both lasers are used with a modulation frequency of 25 MHz at the maximal modulation amplitude of 1.9 Vpp. This results in a sideband power of

[9] Toptica FPI 100-0750-3V0

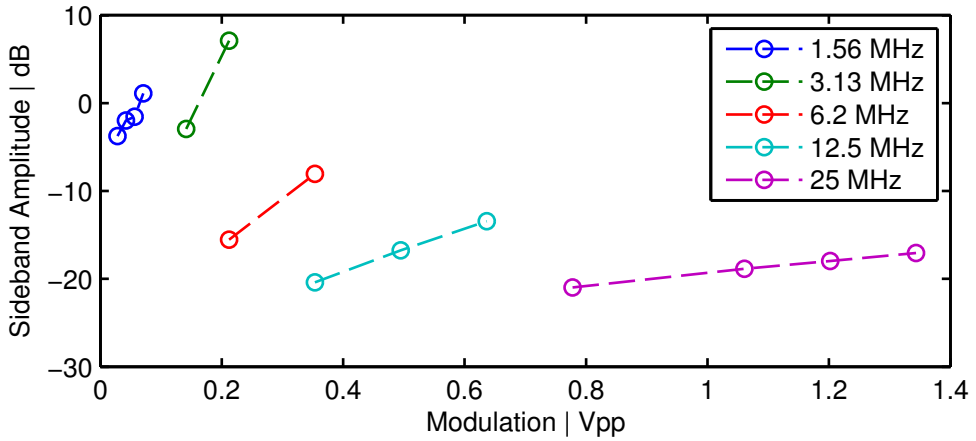

Figure 3.5: Measured sideband strength of Toptica DL Pro ECDL laser at 780 nm

$P = -17\,\mathrm{dB}$ for the cooling laser and $P = -13\,\mathrm{dB}$ of the repumping laser due to the lack of the 50/50 power splitter. The power splitter of the cooling laser is needed as the sidebands are also used to lock a transfer Fabry-Perot cavity on the laser (see figure 6.3). The photodiode signal for the PDH lock is demodulated internally by the DigiLock to creating the error signal necessary for the laser lock.

3.2.2 Repumping Light

The power of the repumping laser is already high enough so further amplification is not needed. It is simply passed through a single pass AOM at approximately +80 MHz to change the frequency from the $F = 1 \rightarrow F' = 1{,}2$ crossover to the $F = 1 \rightarrow F' = 2$ repumping line. The beam is split for the 2D and 3D MOT. The 2D MOT part is coupled into one axis of the polarization maintaining 2D MOT fiber whereas the 3D MOT part is coupled into one input of the 2-6 fiber port cluster[10]. This cluster overlaps the repumping and cooling light for the 3D MOT and splits it into six polarization maintaining fibers for the six MOT axes.

3.2.3 Cooling Light

The cooling light is preamplified by a tapered amplifier (TA)[11] to avoid any power limitations. The light emitted from the TA is split into three parts. The first part passes an AOM and is used as the detection, pushing and repumping light, each one coupled into separate single mode fibers. The second and third part is transmitted through a double pass AOM and each seeds an additional TA for the 2D and 3D MOT respectively. Both TA have a maximal output power of 1.5 W.

[10] This cluster is a commercial splitter from Schäfter und Kirchhoff. The light from the two incoupling fibers is overlapped on a polarization dependent beam splitter and subsequently split into six beams using polarization dependent beam splitters. The beams are then coupled into polarization maintaining fibers. The splitting ratio can be controlled via waveplates. The transmission through the cluster (without incoupling efficiency) is $\approx 75\%$

[11] This TA has a maximal output power of 1W and normally runs at $P_{\mathrm{out}} \approx 150\,\mathrm{mW}$

The 2D MOT cooling light is superimposed with the repumping light at a polarizing beam splitter and coupled into the 2D MOT polarization maintaining fiber.
To switch the 3D MOT cooling light efficiently, the beam is passed through a switching EOM[12]. It has a high transmission of approx. 90 %, the switching time is limited by the slew rate of the Amplifier[13] of $300\,\mathrm{V\,\mu s^{-1}}$.

3.3 Magnetic Fields

To create the 2D/3D MOT combination and subsequent evaporation to quantum degeneracy we use three sets of coils in the experiment. The rectangular 2D MOT coils create the fields for the 2D MOT where the atoms are precooled and subsequently transferred by a pushing beam into the 3D MOT. The 3D MOT coils are located in the same water chilled housing as the magnetic cloverleaf trap. Around the magnetic trap, the compensation coils are located to eliminate offset fields and field gradients.

3.3.1 2D MOT Coils

The design of the rectangular 2D MOT coils follows the existing design in the group [105, 109]. They are wound onto an aluminum housing and connected in series to an anti Helmholtz configuration. Each coil has 42 windings and is operated with currents from 5 A to 7 A. The whole housing is mounted onto a two inch mirror mount and a translation stage to align it with respect to the differential pumping tube. A gradient of $20\,\mathrm{G\,cm^{-1}}$ is created in the center of the 2D MOT glass cell at a current of 7 A [105]. To ensure that each individual coil has no defects or electrical short circuits, we measured the inductance ($L \approx 90\,\mu\mathrm{H}$ @ $1\,\mathrm{kHz}$[14]) and resistance ($R \approx 625\,\mathrm{m\Omega}$) of each coil. Also the number of windings was crosschecked with a current clamp.

3.3.2 3D MOT Coils and Magnetic Trap

The 3D MOT coils and magnetic trap in use in this experiment was developed during the diploma thesis of Ralf Dinter [110, 111]. It proved to very reliably produce large volume magneto optical traps and in combination with the magnetic trap and rf evaporation very large BECs. This trap is in use in several experiments in our group [105, 111] [112][15].
Both coils are water cooled by pumping water through the housing. The two sides are held at a distance of 30 mm by four spacers and are mounted onto the optical table with two aluminum feet for maximal stability. To ensure both coils are similar and do not show any defect, the inductivity and resistance of the Helmholtz and magnetic trap coils (see appendix, Table B.3) was measured.
The current to drive these coils is supplied by two high power switching power supplies[16].

[12] Linos LM0202
[13] A.A. Lab Systems A-301HS
[14] Measured with Hameg HM8118
[15] This trap is an older version and has a slightly different parameters
[16] Delta Elektronika SM 45-140-P154, 45V, 140A with 0-10V analog control input modification.

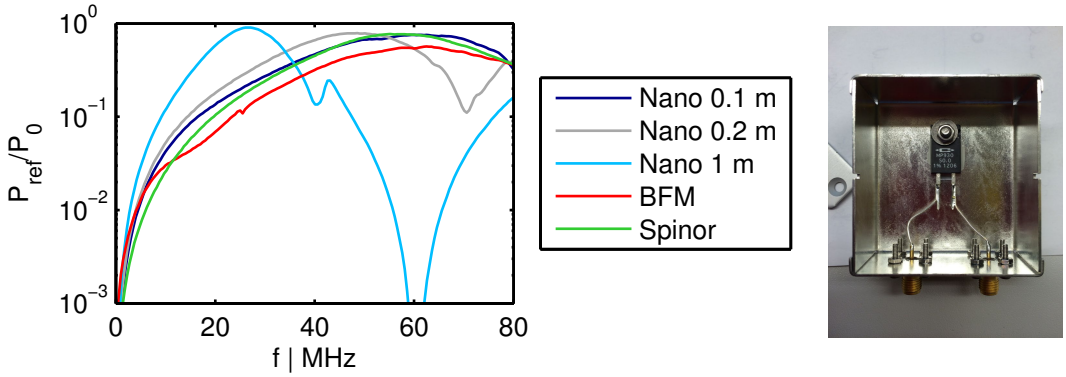

Figure 3.6: Reflected power of the evaporation system, measured with a network analyzer for different cable length between the 50 Ω resistor and the one-loop antenna. Shown on the right is an image of the inline 50 Ω resistor.

Helmholtz Coils

Located in the outer part of the housing are the Helmholtz (HH) coils. They have a total of 54 windings, nine windings in six radial layers. With their radius of 75 mm and distance between the two coils of 35 mm they produce a homogeneous field of $7.67\,\mathrm{G\,A^{-1}}$ in Helmholtz and a radial gradient of $(0.50 \pm 0.02)\,\mathrm{G\,A^{-1}\,cm^{-1}}$ in anti-Helmholtz configuration, measured using a hall probe.

Magentic Trap

The magnetic trap used in this experiment is a hybrid 4-Dee trap. The cloverleaf coils consist of 14 and the dees of 42 windings. The magnetic trap is operated with a current of 110 A and is used together with the HH coils. Dependent on the current in the HH coils it is possible to create a large volume isotropic trap ($I_{\mathrm{offset}} \approx 38\,\mathrm{A}$) which is used when transferring atoms from the MOT into the magnetic trap. The trap can be compressed trap with a lower offset field of $I_{\mathrm{offset}} \approx 3\,\mathrm{A}$, which is used during rf evaporation. Due to the small trap frequencies ω in the isotropic trap, the position of the trap minimum is not in the geometrical center of the coils. The atoms are affected by the gravitational sag [109] and located

$$s = -g/\omega^2 \tag{3.1}$$

below the geometrical center. With the measured frequency of $\omega \approx 2\pi \cdot 11\,\mathrm{Hz}$, this corresponds to a sag of 2 mm. To reduce oscillations during the transfer, the MOT is shifted to the position of the isotropic trap by applying a homogeneous field in the vertical direction, the MOT translation field.

3.3.3 Evaporation System

We use radio frequency evaporative cooling [98–100] to achieve Bose-Einstein condensation in the magnetic trap. The radio frequency is used to flip the spin of high energy atoms to expel them from the trap. Subsequent rethermalization reduces the ensemble

temperature. During the evaporation, the phase space density is increased by six orders of magnitude [109]. The evaporation system consists of a rf source[17], a rf amplifier[18], and a 50 Ω resistor[19] (Figure 3.6) that is connected in line with the rectangular one loop antenna. The antenna has a dimension of ≈ 25 mm × 80 mm, is made from silver wire, and is mounted in contact to the side of the glass cell. We observed that it is crucial for the cable between the resistor and the antenna to be as short as possible due to back-reflection issues. Shown in Figure 3.6 is the measured reflection signal[20] of the 50 Ω resistor and the antenna for three cable lengths and in comparison to two already running experiments in our group. For the one meter cable, a strong maximum at 30 MHz is visible, interfering with the evaporation ramp which is normally employed from 40 MHz to 800 kHz. A shorter cable between the antenna and the resistor moves this maximum to higher frequencies where it does not affect the evaporation substantially any more.

3.3.4 Compensation Coils

The HH coils and the magnetic trap are surrounded by three pairs of compensation coils. They can be used to compensate residual magnetic fields if used in HH configuration or to compensate gradients in anti-HH configuration. The design, especially the axial coil was optimized compared to previous realizations in the group. Each pair of compensation coils consists of three separate coils with different winding numbers and can be connected individually to HH or anti-HH configurations. The calculated field strength are listed in Table 3.1 and the spatial field distribution is shown in Figure 3.7. The axial compensation coil is circular and close to a ideal HH geometry. This results in a very homogeneous field, compared to the two other coil pairs, which are realized in a racetrack geometry.

The calculation was done using a Matlab implementation of the Biot-Savart law programmed by Sören Dörscher. As can be seen in the simulation, the axial coils, shown in the top row of Figure 3.7, create a very symmetric field. The field is approximately 200 times more homogeneous 10 mm away from the center compared to racetrack coil implementations. This enables the creation of very homogeneous fields or close to ideal anti-HH configurations if necessary. The coils are mounted directly on the magnetic trap housing, reducing relative movement between the magnetic trap and the compensation coils.

[17] Toptica VFG
[18] Minicircuits LZY-22+
[19] MP930 - 50 Ohm. The resistor is mounted on a passive heat as it can get warm.
[20] Rohde & Schwarz ZVL13 Network Analyzer

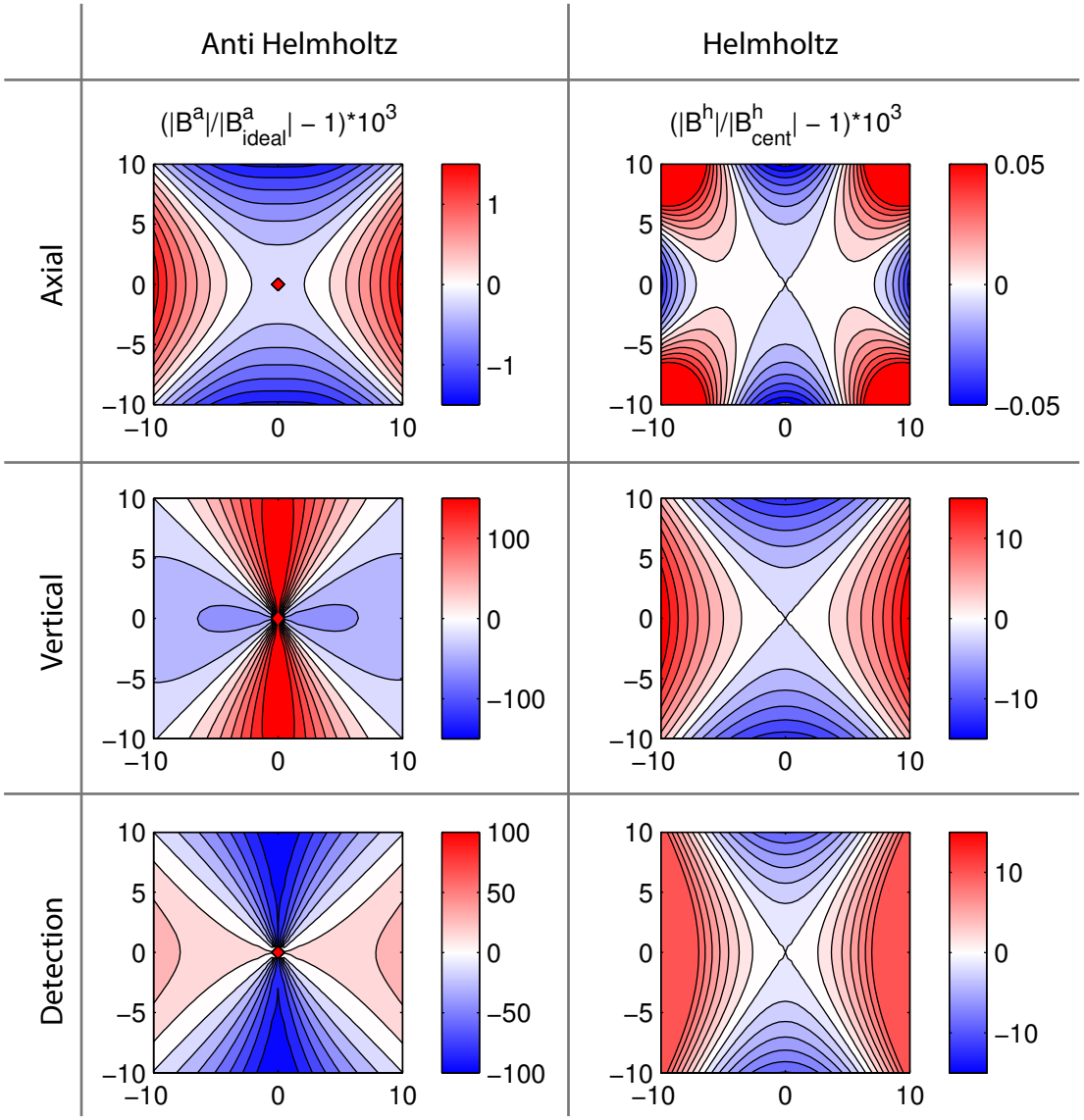

Figure 3.7: Simulated magnetic fields of the compensation coils. **Left:** Deviation from an ideal anti-Helmholtz coil calculated as $B(\mathbf{r})/B_{\text{ideal}}(\mathbf{r}) - 1$. **Right:** Inhomogeneity in Helmholtz configuration, normalized on the field in the center $B(\mathbf{r})/B(\mathbf{r} = \mathbf{0}) - 1$. **From top to bottom:** Axial, vertical, detection. All units are in mm. The vertical and detection compensation coils are racetrack coils. This results in the worse homogeneity in HH and anti-Helmhotz configuration.

Axial	$\partial_{x/y} = 73.4/144.5$ [G/Am]	0.33 G/A @ 4 wdg	1,1,2 layer
Vertical	$\partial_{x/y} = 91.4/149.2$ [G/Am]	0.22 G/A @ 7 wdg	1,2,3 layer
Detection	$\partial_{x/y} = 64.0/144.0$ [G/Am]	0.19 G/A @ 7 wdg	1,2,3 layer

Table 3.1: Simulated gradients and homogeneous field strengths of the compensation cage. There are three coils with different number of layers wound into each coil housing. The axial coils have four windings per radial layer, the other two have seven.

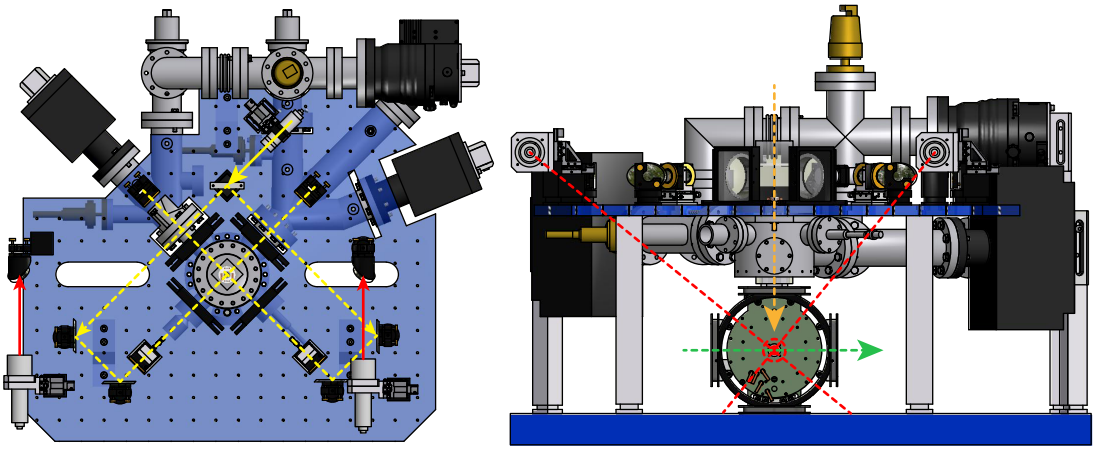

Figure 3.8: Sketch of the beam path for the 2D MOT (yellow), 3D MOT (red), detection beam (green), and pushing beam (orange). The 2D MOT beam is split on the upper breadboard with a polarizing beam splitter in the two axes and expanded with a cylindrical telescope to form the elliptic beams necessary for the 2D MOT. The upper 3D MOT telescopes are located on the upper level and reflected through a hole in the breadboard onto the lower glass cell. Both beams are tilted by eight degrees with respect to the 45 degree axes which is reserved for a retroreflected 2D lattice (not shown here). The pushing beam is passing vertically through the differential pumping tube in the center of the vacuum chamber and transfers the atoms from the 2D MOT into the 3D MOT.

3.4 Optics

In this Section an overview of the optics used for the creation, manipulation and detection of the BEC is given. All of the light is transferred to the experiment with optical fibers and collimated and focussed onto the atoms with telescopes.

3.4.1 2D MOT

The starting point in creating a sample of cold atoms is the 2D MOT. Here, highly elliptical beams are used to create a 2D MOT above the differential pumping tube. The cooling and repumping light emitted from the polarization maintaining fiber is collimated with a telescope[21] and split with a $\lambda/2$ plate and a polarizing beam splitter into the two axes (Figure 3.8). The telescope is mounted on a vertical translation stage which enables easy alignment with respect to the axis of the subsequent lenses once the beam is aligned to be horizontal. Both axes pass a $\lambda/4$ plate and are expanded by a two lens cylindrical telescope[22] to elliptical beams with a diameter of $13.5\,\mathrm{mm} \times 54\,\mathrm{mm}$. After passing the glass cell, each beam is focussed[23] through a $\lambda/4$ plate onto a retroreflecting mirror. The size of the beam can be controlled with an aperture that is mounted on the collimation telescope.

[21] Schäfter und Kirchhoff 60FC-T-4-M75-37, collimated beam diameter 13.5 mm
[22] Thorlabs LK1336L1-B ($f = -50\,\mathrm{mm}$) and Thorlabs LJ1309L1-B ($f = 200\,\mathrm{mm}$)
[23] Thorlabs LA1002-B ($f = 150\,\mathrm{mm}$)

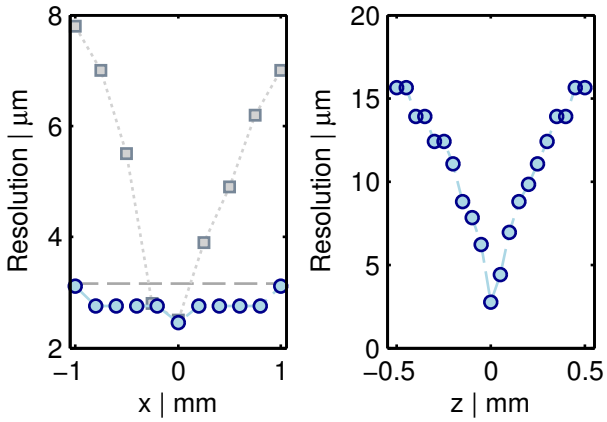

(a) **Left:** Measured offaxis performance in blue. The horizontal dashed gray line indicates the calculated performance. Previous systems developed in our group displayed in grey, M = 5 [113]. The measured images are shown in Figure 3.10. **Right:** Measured depth of field for the same magnification.

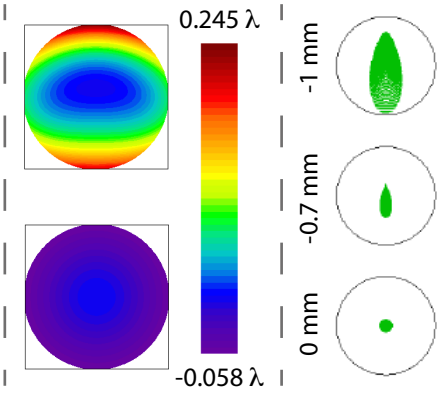

(b) **Left:** Calculated wavefront curvature 1 mm off the optical axis (upper) and on the axis (lower). **Right:** Calculated spot diagram on and offaxis. The circle shows the Airy disk.

Figure 3.9: Measured and calculated performance of the detection system. Shown here is the $M = 3.46$ magnification.

3.4.2 3D MOT

To create a large volume 3D MOT, the light splitted by the fiber port cluster is collimated by large beam diameter telescopes[24]. The integrated $\lambda/4$ waveplate in combination with the polarization maintaining fiber enables an easy and stable alignment to the required circular polarization needed for the MOT. The upper telescopes are mounted on the upper breadboard where also the 2D MOT optics is located. They are reflected through cuts in the breadboard onto the 3D MOT cell. Any phase delay of the mirrors between $s-$ and $p-$polarization can be compensated with the internal $\lambda/4$ plate and a rotation of the telescopes themselves. The 3D MOT is tilted by eight degree with respect to the diagonal axes where a far-detuned 2D lattice will be installed later on. This design circumvents the need to overlap the two different wavelengths. The lower telescopes are located in a hole below the lower breadboard and reflected with mirrors through a slit in the lower breadboard onto the 3D MOT cell. The axial beams are reflected through the hole of the magnetic trap onto the 3D MOT cell. The beam paths are sketched in Figure 3.8.

3.4.3 Detection System

The detection system in use at this experiment is a home built multi-lens telescope with excellent off-axis performance, numerical aperture of 0.15 and a resolution of $\approx 3\,\mu m$. It was developed using OSLO[25] at this experiment during the bachelor thesis of Martin

[24] Schäfter und Kirchhoff 60FC-Q780-4-M150-37, collimated beam diameter 26.9 mm

[25] OSLO is a commercial raytracing software which can optimize optical systems by minimizing an user defined error function which depends on the various aberration coefficients.

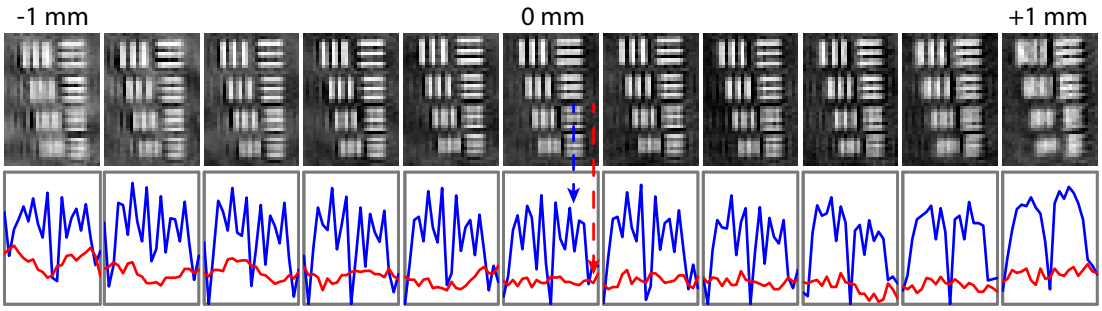

Figure 3.10: Raw data of the field of view measurement obtained with a pco.pixelfly USB camera. Images are from -1 to +1 mm off the optical axis. The blue lines are vertical cuts through the smallest two horizontal line segments, the red a vertical cut through the background on the very right. This is indicated by the two dashed lines in the center. The segments correspond to 3.11/2.76/2.46/2.19 µm.

Jambor [114]. The system consists of two sub-parts, a collimating part with a focal length of $f = 136.9\,\text{mm}$ and a replaceable focussing part to realize different magnifications. It is the third iteration of homebuilt detection systems in our group [113, 115]. One goal during the development of this particular system was the optimization of the off axis performance. Good off axis performance enables easier alignment as the exact position of the telescope is rather uncritical and it is possible to change the time of flight setting without changing the lens position.

Each lens has aberrations but some are positive, other negative. The idea behind multi-lens systems is to compensate the total aberrations of the system by carefully choosing specific lenses which work well together in terms of aberrations and give the desired design specifications like focal length and NA. The improvement in off axis performance compared to the previous design is achieved by using exclusively curved lenses. Although more difficult it enables a better compensation of the total aberrations as there are more degrees of freedom for the system. The calculation and measurement for the $M = 3.46$ magnification are exemplarily shown in Figure 3.9.
One diffraction criterion can be calculated from the wave front curvature of the multi lens system. Diffraction limited performance [116] is achieved if the peak-value optical path difference $OPD_{\text{P-V}} \leq 0.25\lambda$ and the rms optical path difference is $OPD_{\text{RMS}} \leq 0.07\lambda$. This is valid as can be seen in Figure 3.9 for the on axis performance, as well as for 1 mm off-axis. The second diffraction criterion is connected to the Airy disk. If all traces through the multi-lens system are located in the Airy disk, the systems shows diffraction limited performance. This is also given on the optical axis as well as 1 mm off-axis as can be seen in Figure 3.9 (b) on the very right.

The measure resolution of the $M = 3.46$ magnification, obtained with an USAF 1951 target, validates the expected excellent off-axis performance. As the resolution is even better than expected, Figure 3.10 shows the corresponding test-target images for the field of view measurement. It is clear to see that the horizontal 3.11 µm and 2.76 µm

Description		Magnification	Resolution | µm	off-axis $OPD_{\text{P-V}}$ | λ	off-axis OPD_{RMS} | λ
Collimating part itself		-	3.16	0.244	0.052
Collimating part combined with	self designed	1.58/1.68	3.49/3.47	0.276	0.066
	focus solutions	3.04/3.46	3.16/2.76	0.248	0.055
	commercial aplanat	2.2/2.28	3.16/2.76	0.213	0.046
	single achromats	5.11/5.11	3.16/2.76	0.235	0.050
		7.3/7.24	3.16/2.76	0.243	0.051

Table 3.2: Overview of the optical performance of the detection system. The two values stated for magnification and resolution are the calculated and measured value. To ensure diffraction limited performance the optical path differences have to be $OPD_{\text{P-V}} \leq 0.25\lambda$ and $OPD_{\text{RMS}} \leq 0.07\lambda$.

segments are resolved from -1 mm to 1 mm whereas in the very extremes, the vertical lines of the 2.76 µm segment are not well resolved. In the center it can be argued that also 2.46 µm is resolved. All in all this is an excellent performance. The measured off axis performance is slightly worse for the lower magnifications but always better than ± 0.6 mm. An overview of the calculated and measured performance for the different magnifications is shown in Table 3.2.

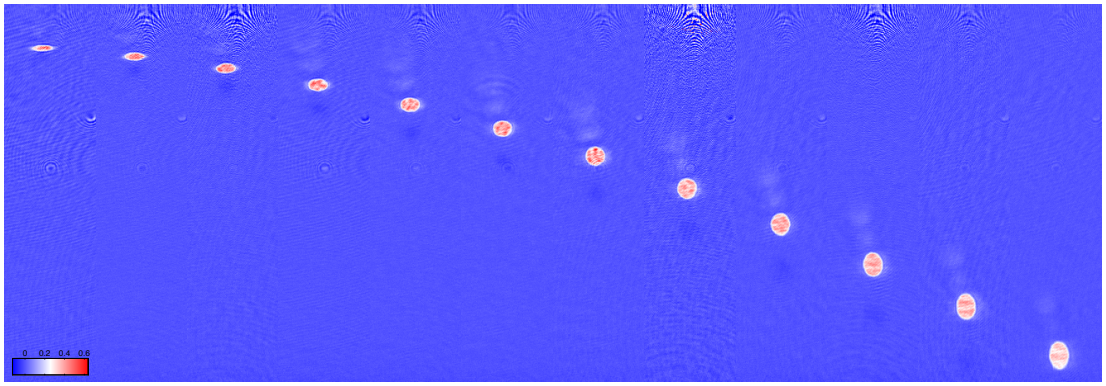

Figure 3.11: TOF sequence of a ^{87}Rb BEC prepared in the magnetic trap for a time of flight of 1 ms to 23 ms.

3.5 System Performance

This Section presents some proof of principle measurements to ensure that the system is operational and performs comparable to other ^{87}Rb setups in our group. These measurements are in no way meant to be a complete characterization and may not include all experimental parameters in detail. This will be presented in the upcoming thesis of Christina Staarmann.

3.5.1 Observation of Bose-Einstein Condesation

To ensure that it is indeed possible to achieve quantum degeneracy in this newly set up system, Figure 3.11 shows a time of flight (TOF) sequence [96] of a ^{87}Rb Bose-Einstein condensate. Visible is the characteristic aspect ratio inversion due to interactions from a horizontally elongated cloud on the left to a vertically elongated cloud on the right. The images are obtained via absorption imaging, each image is a new realization of a BEC. The dark spot below the BEC are residual atoms on the reference image. A homogeneous offset field using the HH coils is applied during the reference image to reduce this effect, brining the atoms out of resonance with the detection light. The bright clouds to the top left of the BEC are most likely aberrations, maybe from reflections of the detection light on the uncoated inner sides of the glass cell.

To prepare the BEC, the MOT is loaded for 11 s. Subsequently, the MOT gradient field is switched off and a molasses phase of 5 ms cools the atoms further. The next step, evaporative cooling, is done in the magnetic trap. The atoms are transferred to the circular magnetic trap at a homogeneous offset field of $I_{\text{off}} = 38.8\,\text{A}$. To increase the density, the magnetic trap is compressed by exponentially lowering the offset current over 1.5 s to 3.19 A. During this step, the Delta power supply is ramped to zero current and the trap floor current is supplied by the HMP2030 power supply (see Figure B.2 in the appendix). Evaporation was done from 50 MHz to 800 kHz over 18 s using an exponential ramp. This results in a pure BEC without a visible thermal component as can be seen in Figure 3.11.

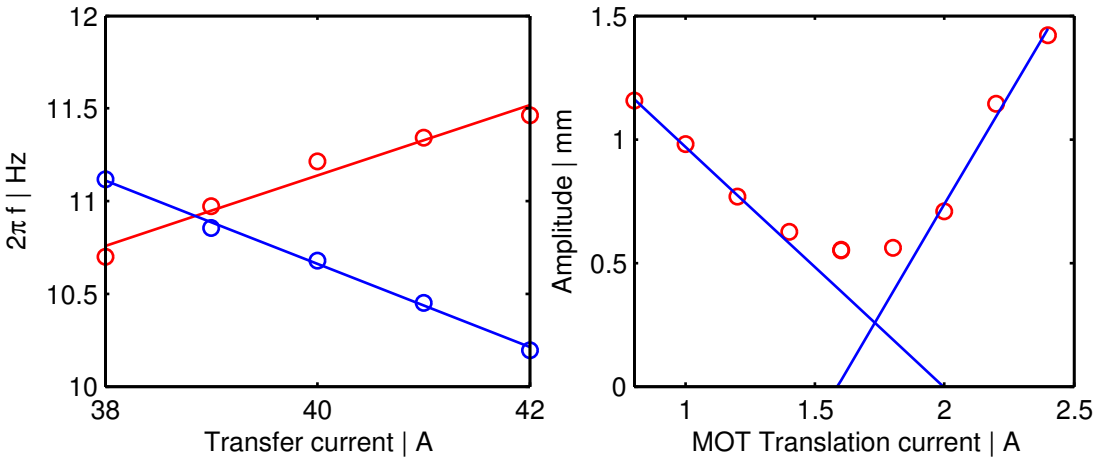

Figure 3.12: Left: Vertical/horizontal trap frequencies (red/blue) dependent on the transfer current applied to the HH coils. The solid lines are linear fits to the data. **Left:** Amplitude of center of mass oscillations in the circular magnetic trap, dependent on the MOT translation coil current. The solid lines are linear fits to the outer three data points.

3.5.2 Magnetic Trap Oscillations

To improve the transfer to the magnetic trap, we measured the trap frequency in the vertical and horizontal direction of the circular magnetic trap by fitting a sinusoidal oscillation to the position of the atomic cloud over several periods. To efficiently transfer the molasses to the magnetic trap, a spherical geometry is desired. The fitted intersection point of the vertical and horizontal frequency in Figure 3.12 is at $I_{\text{off}} = 38.8\,\text{A}$. Knowing this transfer current, an optimization of the MOT translation current is necessary as shown in Figure 3.12 on the right. A clear minimum of the oscillation amplitude after transfer to the magnetic trap at around 1.7 A is visible. The still present oscillations are most likely caused by the misaligned MOT as the measurement was done with the MOT aligned to the calculated translation current of 1.344 A. Here, further optimization is necessary.

3.5.3 Magnetic Trap Lifetime

To ensure that efficient evaporation is possible, the lifetime of cold atoms in the magnetic trap was measured. This result is shown in Figure 3.13 on the left. The trap floor was chosen such that a BEC was visible at $\approx 170\,\text{kHz}$. The measured lifetime for evaporation to 3 MHz is 52 s without the rf-shield and 40 s with the rf-shield applied also at 3 MHz. The data agrees well with an exponential decay. If the temperature of the ensemble is reduced and density increased by evaporating to a lower frequency, three body losses start to limit the lifetime of the atoms in the trap. This results in a double-logarithmic decay with a measured decay rate of 3.6 s and 23.8 s.

The BEC lifetime, shown in Figure 3.13 on the right also depends on the offset field of the trap. For a low offset field which corresponds to an end-evaporation frequency

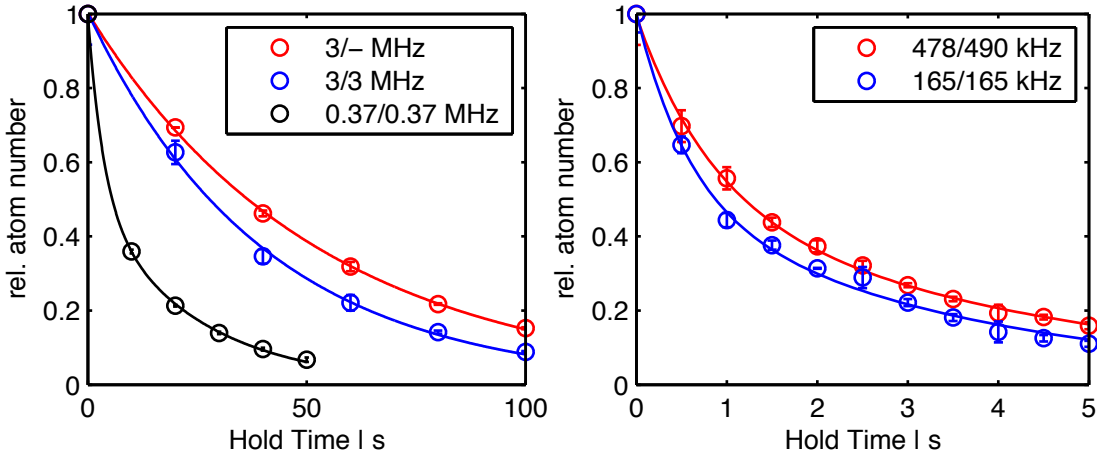

Figure 3.13: **Left:** Lifetime of cold atoms in the magnetic trap for different end evaporation frequencies. The first value in the legend is the evaporation end-frequency, the second value the rf shield frequency. The solid lines are fitted exponential decays, the black is a double exponential decay. **Right:** BEC lifetime at different end evaporation frequencies. The solid lines are fitted double exponential decays. The error bars are the standard deviation of three images.

of 165 kHz, the measured lifetime is 0.6 s and 3.5 s. The less steep trap with higher offset field and therefore higher end-evaporation frequency shows a longer lifetime of 0.8 s and 4.4 s.

Note that the lifetime measurements were performed without the dedicated trap floor power supply. The trap floor in these measurements current was supplied by the large Delta Elektronika supply. The implementation of the dedicated supply did not change the performance on the first glance but will be studied in a later characterization measurement. The lifetimes presented in Figure 3.13 are already more than sufficient to perform experiments with kHz range interaction between the membrane and the atoms. After some optimization, the larges BECs with $N = 8 \times 10^4$ were obtained at evaporation end frequencies of ≈ 800 kHz. At these higher frequencies, the three body losses are further reduced and a longer lifetime than the measurements in Figure 3.13 is expected.

3.6 Conclusion

To conclude, a robust machine to create ultracold ^{87}Rb samples was planned and set up. As the system is similar to already existing setups in our group, some further optimization will result in even larger BECs of $N \approx 1 \cdot 10^6$ atoms. The atomic side of the experiment is ready to move to the laboratory where the cryostat is located.

Chapter 4

Fiber Processing

This chapter discusses the fiber processing necessary to create high finesse fiber cavities. The CO_2 laser system is described and the in-house Linnik interference microscope used to analyze the processed fiber tips is discussed and validated.

The optomechanical part of this hybrid quantum system is a fiber-based MiM system. To realize fiber Fabry-Pérot cavities, CO_2 laser processing of the fiber ends is commonly used to create concave features on the fiberend, necessary to realize a stable Fabry-Pérot cavity mode. This laser-based fiber processing was pioneered by the group of J. Reichel [117]. The ultra low roughness concave features are ideally suited for subsequent high reflective coating to create a fiber-based Fabry-Pérot cavity [47, 74]. The good surface quality is created by the thin melt layer [118, 119] that forms during the evaporation. Previous realization of fiber cavities were based on transferring an external fabricated mirror onto the fiber [120], a much more difficult procedure compared to laser-based fabrication.

4.1 CO_2 Laser System

Regular optical fiber used in the near infrared are made from glass. The CO_2 laser processing is based on the strong absorption of 10.6 µm light in glass and subsequent evaporation of material [122]. To create concave structures on the fibertip, the CO_2 laser is focussed to a similar size as the desired structure size. The quality of the focus is important as any imperfections will be visible in the processed structure.

The CO_2 laser used here has a maximal output power of 28 W and is a laser normally used for engraving. It is controlled over an external TTL signal by a home programmed micro controller system[1]. It enables easy control of the pulse sequence (one pulse, continuous pulses etc.) of various lengths. It is easy to use and can be expanded later on if needed. The output power of the CO_2 laser is intrinsically puled at $f \approx 800\,\mathrm{Hz}$ (see

[1] Conrad C-Control I Station

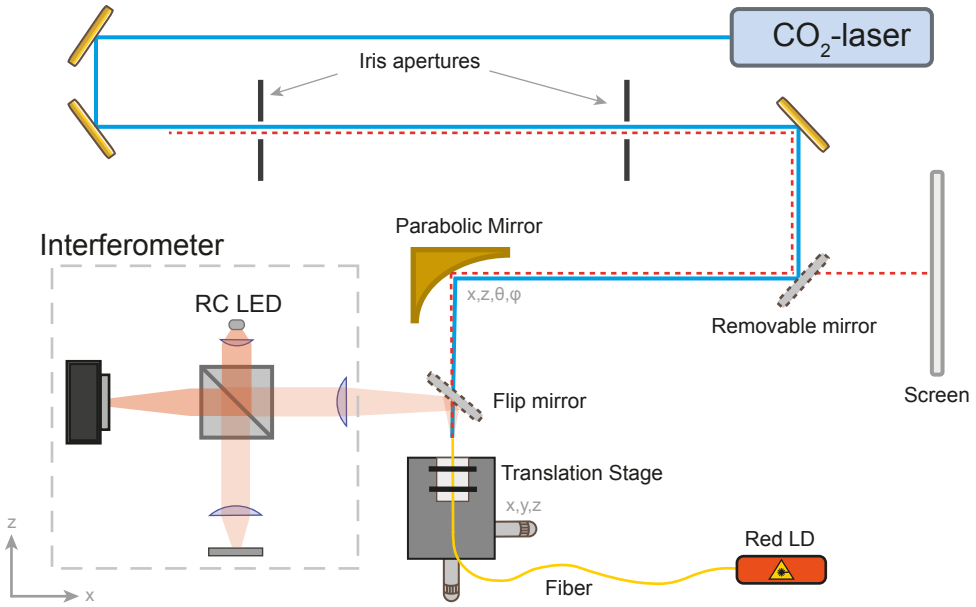

Figure 4.1: Sketch of the CO_2 laser-based fiber processing setup. A flip mirror interfaces the CO_2 laser and the interferometer shown in the gray box. Figure taken from [121].

Figure C.1 in the appendix). The whole system is mounted on a 1.2 m × 0.45 m breadboard an can be easily transported. A sketch of the CO_2 laser setup is shown in Figure 4.1.

4.1.1 Alignment

The central focussing element of the CO_2 laser, a parabolic mirror shown in Figure 4.1, is alined using 660 nm light emitted from a pigtailed laser diode[2]. The focussing of a parabolic mirror is based on reflection and therefore wavelength independent. It allows the combination of alignment and processing optics in one optical element. Normally ZnSe lenses are used [123, 124], which are based on refraction and therefore wavelength dependent.

By collimating the emitted light, the focus of the parabolic mirror is centered on the fiber core and the optical axis of the parabolic mirror is aligned with respect to the fiber axis. The collimation is checked and optimized at distances of about five meters on a screen. This is possible as one of the mirrors in the beam path is mounted in a removable mirror mount. Any misalignment of the parabolic mirror is visible as aberrations such as coma in the collimated beam. The alignment sensitivity of the parabolic mirror is also the main downside in the approach presented here. Nonetheless if aligned correctly, which can be done quickly with some experience, the parabolic mirror produces high quality foci and can be used for fiber processing. An exhaustive treatment of the developed alignment techniques can be found in the masters thesis of Philipp Christoph [121].

[2] Thorlabs LPS-660-FC

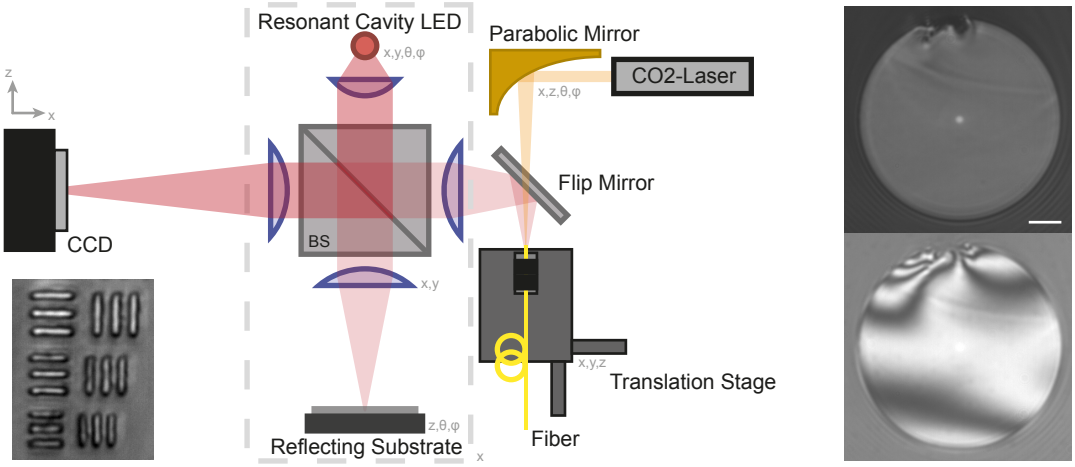

Figure 4.2: Left: Sketch of the Linnik interference microscope used to analyze the processed fiber tip. **Right:** The upper image is a typical fiber image I_f with the interferometer arm blocked. The lower image shows the same fiber with the interferometer arm unblocked. The length bar indicates 20 µm. **Lower Left:** Image of the smallest three segments of a USAF 1951 test target corresponding to a resolution of 2.76/2.46/2.19 µm.

To focus the CO_2 laser onto the fibertip, two apertures are used to mark the beam position of the aforementioned collimated beam. The CO_2 laser is superimposed using these apertures. This procedure ensures that the fiber tip is hit by the CO_2 laser. Unfortunately, this alignment method is not precise enough to center the CO_2 laser spot on the fiber, it is approx. 20 µm to 30 µm off in a normal situation. The large collimated beam is difficult to center precisely on the first aperture. Another error-source is a finite cleave angle of the alignment fiber. This angle will cause a small refraction of the light away from the geometric fiber axis. Therefore it is important to use a well cleaved alignment fiber. The final alignment is done by iteratively processing the fiber, marking the spot on the fiber and realigning it with the fiber xy-stage to center the CO_2. This fine alignment is necessary on a daily basis due to small drifts in the whole setup.

The apertures are also used to reduce the beam diameter on the parabolic mirror to reduce aberrations [121].

4.2 Interferometer

Two properties are important when processing fibers to manufacture fiber cavities. First of all it is important to determine the spatial shape of the processed feature, especially the radius of curvature r, as this radius defines the spatial mode shape in the cavity. Secondly, it is important to ensure that the concave feature is centered on the core of the fiber to achieve a good through coupling efficiency. The position of the cavity mode is fixed by the position of the concave feature.

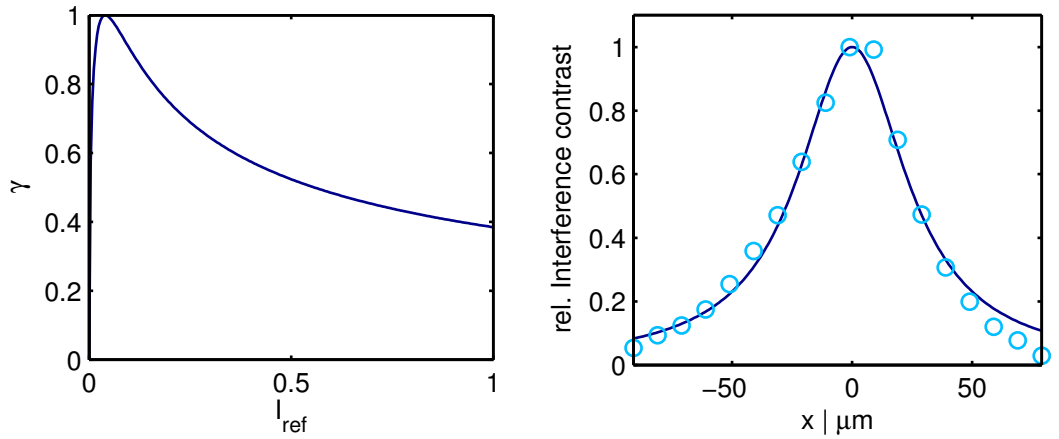

Figure 4.3: Left: Calculated interference contrast γ according to Equation 4.5 dependent on the reflected intensity of the reference substrate I_{ref} for $I_{\mathrm{f}} = 0.04$. **Right:** Measured interference contrast of the interferometer against a length change of the reference beam path, scaled to one. The solid line is a Lorentzian fit, also constrained to a maximal value of one.

To tackle these problems we set up a short-coherence-length Linnik interference microscope (LIM) [125], sketched in Figure 4.2. This modification of the Michelson interferometer replaces one mirror with the surface to be measured and adds lenses in the imaging and reference arm. A typical image of a fiber (I_{f}) is shown in Figure 4.2 in the upper right. Below that is an image of the same fiber with the interferometer arm unblocked (I_{int}).

The observed image I_{int} is the interference between the image of the fiber I_{f} and the image of the reference substrate I_{s}.

$$
\begin{aligned}
I_{\mathrm{int}}(\mathbf{r}) &= \left|E_{\mathrm{f}}(\mathbf{r}) + E_{\mathrm{s}}(\mathbf{r})\right|^2 && (4.1)\\
&= E_{\mathrm{f}}(\mathbf{r})E_{\mathrm{s}}^*(\mathbf{r}) && (4.2)\\
&= \left|E_{\mathrm{f}}(\mathbf{r})\right|^2 + \left|E_{\mathrm{s}}(\mathbf{r})\right|^2 + 2\,\mathrm{Re}\left(E_{\mathrm{f}}(\mathbf{r})E_{\mathrm{s}}^*(\mathbf{r})\right) && (4.3)\\
&= I_{\mathrm{f}}(\mathbf{r}) + I_{\mathrm{s}}(\mathbf{r}) + 2\sqrt{I_{\mathrm{f}}(\mathbf{r})}\sqrt{I_{\mathrm{s}}(\mathbf{r})}\cos\left(2k\cdot f(\mathbf{r}) - \phi_0\right). && (4.4)
\end{aligned}
$$

The profile depth $f(x, y)$, processed into the fiber leads to a phase shift of the fiber image I_{f} with respect to the reference image I_{ref} of $2k \cdot f(x, y)$, with $k = 2\pi/\lambda$ being the wave number. This phase shift is visible in the interference fringes. Equation 4.4 is often written in terms of the interference contrast

$$\gamma = \frac{2\sqrt{I_{\mathrm{f}} I_{\mathrm{ref}}}}{I_{\mathrm{f}} + I_{\mathrm{ref}}} \tag{4.5}$$

as

$$I_{\mathrm{int}} = I_0\left(1 + \gamma\cos\left(2k\cdot f - \phi_0\right)\right) \tag{4.6}$$

with the mean intensity $I_0 = I_{\mathrm{f}} + I_{\mathrm{ref}}$. Interference contrast of one is achieved if the

fiber and the reference arm have the same reflectivity (see figure 4.3). The reflectivity of a plain glass fiber is with $R = 0.04$ very low. Therefore, a LIM is a better solution compared to commercially available Mirau-type interferometers to inspect fibers as the reflectivity of the reference substrate can be matched to the reflectivity of the fiber using an uncoated glass reference substrate. In Mirau-type microscope lenses, which are often used for interference microscopy due to the single path geometry, the reference has a high reflectivity of $I_{\mathrm{ref}} \approx 1$. This results in a bad interference contrast of $\gamma \approx 0.4$ if used to inspect an uncoated fiber.

The interferometer is illuminated by a resonant cavity LED[3] at 650 nm with a specified coherence length l_{c} [126] of

$$l_{\mathrm{c}} = \frac{2\ln(2)\,\lambda^2}{\pi\Delta\lambda} = 27\,\mu\mathrm{m}. \tag{4.7}$$

The coherence length corresponds to a reduction of fringe visibility by 50% if the path length is changed by $\pm l_{\mathrm{c}}$. The short coherence length is beneficial as only interference in the length scale of the coherence length is visible. No residual interference e.g. between different optical components contributes to the observed signal. A measurement of the fringe visibility against a translation of the reference arm is shown in Figure 4.3 on the left. In this measurement, the interference contrast is normalized to one. The measured width agrees with $l_{\mathrm{c}} \approx 27\,\mu\mathrm{m}$ very well with the specified value. The RCLED is therefore well suited to be used in the interferometer.

Processing setup and interferometer are interfaced with a manual flip mirror. It is flipped away to process the fiber as it blocks the CO_2 laser beam and flipped back to inspect it. Several tests with pellicle beam splitters to overlap the RCLED light and CO_2 were unsuccessful. Coated as well as uncoated pellicle beam splitters showed too much absorption and were destroyed.

4.2.1 Imaging Arm

The imaging arm consists of a 25 mm aspheric lens[4] and the flip mirror. The fiber is imaged onto the CMOS camera[5] using the aspheric lens for collimation and a 500 mm achromatic lens[6] to focus the image onto the camera with a magnification of around 20, which can be easily calculated from the pixel size and fiber diameter. The resolution of this imaging system is better than 2.2 µm, measured with an USAF 1951 test target. The smallest three segments correspond to a resolution of 2.76 µm, 2.46 µm and 2.19 µm are all well resolved (see Figure 4.2).

[3] Optowell PR65-F1P0T
[4] Thorlabs AL1225-A, $NA = 0.23$. This corresponds to a maximal resolution 1.7 µm.
[5] Thorlabs DCC1545M, 1280 x 1024 pixel
[6] Thorlabs AC254-500-A

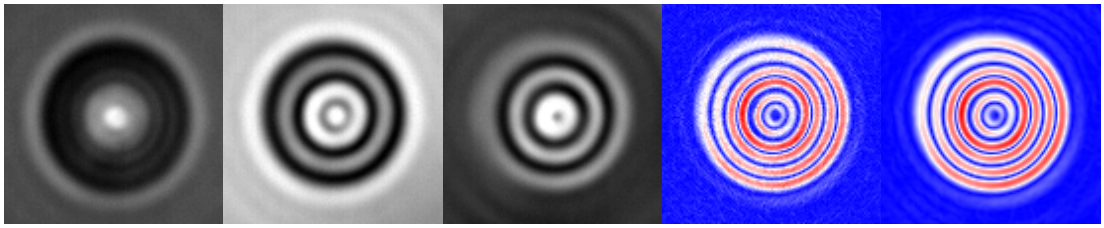

Figure 4.4: **1)** Fiber image I_{ref}. **2/3)** Interference images I_{int}. **4)** Imaged prepared for fitting $|I_{\text{fit}}|$ created with the MATLAB `gradient` routine. **5)** $|I_{\text{fit}}|$ created with `derivative7` routine by Farid and Simoncelli [127]. All images are normalized.

4.2.2 Interferometer Arm

As mentioned above, the interference visible on the camera is an overlap of the image of the fiber and the image of the reference mirror. To ensure that a planar fiber produces a constant interference signal the optical elements in the image and interferometer arm are identical. The aspheric lens in the interferometer arm is mounted in a xy-translation stage to align it to be illuminated at the same position as the lens in the imaging arm. If the position is not identical, the different beam path in the reference and imaging arm lead to a distorted interference signal.
The reference mirror is an uncoated wedged substate. It therefore has the same reflectivity as the fiber while the wedge removes residual light which would not create an interference signal but contribute to an overall offset.

4.3 Interferometer Signal Analysis

To extract the surface profile $f(x, y)$ of the fiber, at least three images of the processed fiber are taken. The first is the fiber image I_{f} with the interferometer arm blocked as can be seen in Figure 4.4 on the very left. The bright spot in the center of the image is a focussing effect of curved structure on the fiber tip. As the fiber is illuminated with near collimated light, the focus f of the curved structure is located at $f = r/2$ above the fiber end. Due to the small radius of curvature of $\approx 50\,\mu\text{m}$, the focus is within the depth of field of the imaging system and therefore visible on the camera.
Next to the fiber image, two interference images I_{int} with different phases are shown. It is possible to extract the surface profile directly from each interference image if the general shape is assumed. This procedure is described in Section 4.3.1. Using two images with two different phases enables a pixel-wise reconstruction of the complete surface profile without assuming a profile shape. This phase-shifting interferometry technique is described in Section 4.3.2.

4.3.1 Interference Fits

As already shown in Equation 4.4, the surface profile $f(x, y)$ is encoded in the interference fringes of the interferometer image I_{int}. To create a robust fit, the fiber image I_{f}

has to be removed. Rewriting Equation 4.4 leads to

$$\cos\left(2k \cdot f - \phi_0\right) = \frac{1}{2\sqrt{I_\mathrm{s}}} \cdot \left(\frac{I_\mathrm{int}}{\sqrt{I_\mathrm{f}}} - \frac{I_\mathrm{f} + I_\mathrm{s}}{\sqrt{I_\mathrm{f}}}\right). \tag{4.8}$$

Taking the derivative of Equation 4.8 enables us to neglect the second term.

$$\frac{\partial}{\partial i}\cos\left(2k \cdot f - \phi_0\right) = c_1 \cdot \frac{\partial}{\partial i}\left(\frac{I_\mathrm{int}}{\sqrt{I_\mathrm{f}}} - \frac{I_\mathrm{f} + I_\mathrm{s}}{\sqrt{I_\mathrm{f}}}\right) \tag{4.9}$$

$$\approx c_1 \cdot I^i_\mathrm{fit} \tag{4.10}$$

Here I_fit is the background removed image, suitable for fitting.

$$I^i_\mathrm{fit} = \frac{\partial}{\partial i}\frac{I_\mathrm{int}}{\sqrt{I_\mathrm{f}}}. \tag{4.11}$$

The reference substate image I_s is constant, the fiber image I_f only varies slowly compared to the interference image I_int. Therefore, the second term in Equation 4.8 is only a slowly varying background that is removed by the derivative. A comparison of the case including the substate image and not neglecting the second term of Equation 4.8 is shown in the appendix in Figure C.2.

The minimum of the profile f can be assumed to be a parabola of the form $f(x) = \alpha(x - x_0)^2$. Taking the derivative in x-direction leads to:

$$\partial_x \cos\left(2k \cdot \alpha(x - x_0)^2 - \phi_0\right) = c_1 \cdot I^x_\mathrm{fit} \tag{4.12}$$

$$\Leftrightarrow \quad x \cdot \sin\left(2k \cdot \alpha(x - x_0)^2 - \phi_0\right) = c_1' \cdot I^x_\mathrm{fit}. \tag{4.13}$$

The radius of curvature r of the profile an be calculated from the parameter α.

$$r = r(x_0) = \frac{1}{f''(x_0)} = \frac{1}{2\alpha}. \tag{4.14}$$

To improve the signal quality of the background corrected image I_fit we use a more sophisticated method compared to the MATLAB `gradient` function to calculate the derivative of the image. Shown on the right in Figure 4.4 is the norm

$$|I_\mathrm{fit}| = \sqrt{\left(I^x_\mathrm{fit}\right)^2 + \left(I^y_\mathrm{fit}\right)^2}. \tag{4.15}$$

of two background corrected images, the left is calculated with internal `gradient` routine from MATLAB, the right one uses `derivative7` from [127]. This routine is based on differentiating an interpolated continuous signal rather than the differential quotient of the sampled date. This is valid as long as the original signal contains no frequencies higher than $2\pi/T$ cycles per length at a sampling rate of T cycles per length [127], which can be assumed for the signals here. If this is the case, the Nyquist theorem states that the signal itself can be reconstructed from the sampled discrete signal.

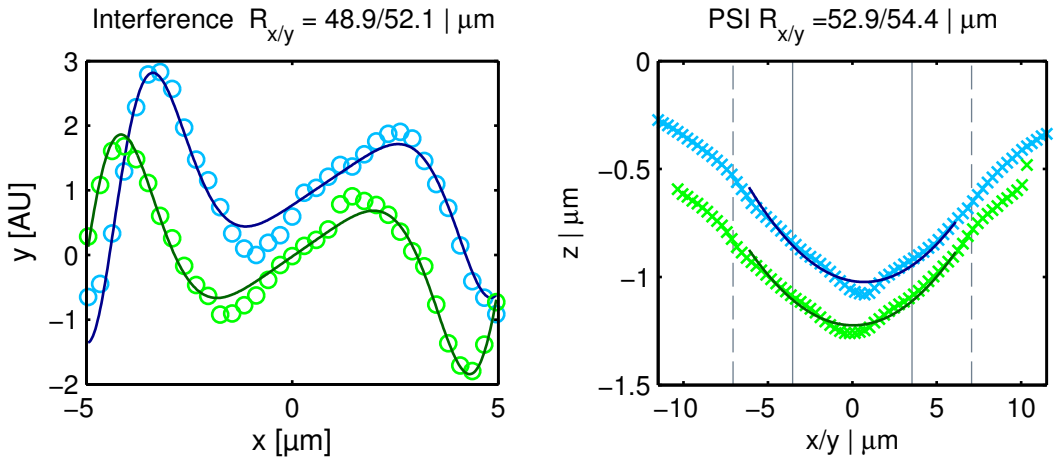

Figure 4.5: Left: Two perpendicular cuts through the background corrected image I_{fit} with the respective fits according to Equation 4.13. **Right:** Parabolic fit to the same two perpendicular axes of the surface profile reconstructed by PSI. The vertical lines (solid and dashed) correspond to the spot size on the curved mirror w_2 and $2w_2$ of a planar concave cavity with $L \approx 25\,\mu\text{m}$ and $r_2 = 50\,\mu\text{m}$.

An exemplary result of an interference fit based on Equation 4.13 for two perpendicular cuts through the image is shown in Figure 4.5 on the left. The blue line is offset vertically to increase the visibility. The fit agrees well with the data and corresponds to a radius of curvature of $r_{x/y} = 48.9/52.1\,\mu\text{m}$.

4.3.2 Phase-Shifting Interferometry and Phase Unwrapping

In contrast to the fringe fitting method presented above, phase-shifting interferometry (PSI) has distinct advantages. It enables the pixel-wise reconstruction of the wrapped phase $\Phi(x, y)$ (modulo 2π) of the interferometer. The interference signal in PSI is commonly written in the form

$$I_{\text{int}}(x, y)(t) = a(x, y) + b(x, y) \cos\left(\Phi(x, y) + \phi(t)\right) \tag{4.16}$$

with $\Phi(x, y) = 2k \cdot f(x, y)$ [125]. The parameter t corresponds to different phases of the interference image. Subsequent unwrapping of the wrapped phase $\Phi(x, y)$ (mod 2π) enables the pixel-wise reconstruction of the surface profile $f(x, y) = \Phi(x, y)/2k$.

The result of such an analysis is presented in Figure 4.5 next to the results from the interference fit. To extract the radius of curvature from the surface function $f(x, y)$, a parabola is fitted to the cuts in x and y direction. Both methods agree well, but the PSI analysis shows a visible oscillation in the reconstructed profile. The deviation from the parabolic shape is discussed in Section 4.4.

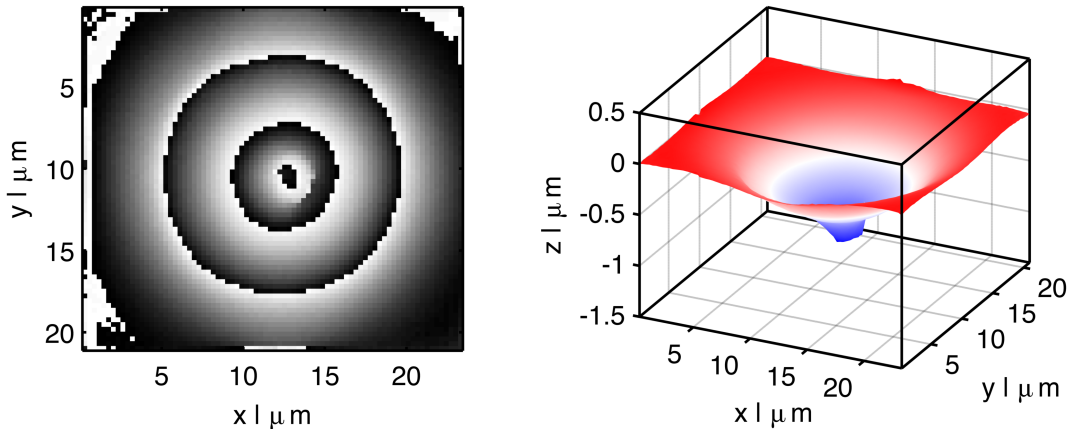

Figure 4.6: Left: Reconstructed phase $\Phi(x, y)$ from two interferometer images with different phases ϕ. **Right:** Complete surface profile $f(x, y)$ of the processed fiber, created by unwrapping the discontinuous phase shown on the left.

PSI

Extensive literature exists on this subject. A good overview are the books [125, 128, 129] and a short summary is given in Philipp Christophs master thesis [121]. Therefore, only a brief idea of this technique is presented here.
For each pixel, according to Equation 4.16, there are three unknowns: a, b and the phase of interest Φ. Assuming there are three images I_{int} for three different, equally spaced phases $\phi_{1,2,3} = [-\varphi, 0, \varphi]$. This system of equations can be solved to obtain the wrapped phase $\Phi(x, y) \pmod{2\pi}$:

$$\Phi \pmod{2\pi} = \tan^{-1}\left(\frac{1-\cos(\varphi)}{\sin(\varphi)}\frac{I_1 - I_3}{2I_2 - I_1 - I_3}\right). \tag{4.17}$$

This is the so called 3-step algorithm. One disadvantage of this technique is the requirement for the phase steps to be equidistant. Any deviation causes errors in the reconstructed phase $\Phi(x, y) \pmod{2\pi}$. In principle there exist four types of PSI algorithms: (1) Constant and known phase shift, (2) constant and unknown phase shift, (3) known but arbitrary phase shift, and (4) unknown and arbitrary phase shift [125].
For the result presented above, we employ a recently developed PSI algorithm of type (4) which uses only two images with arbitrary phase shift[7] [130]. The result of the PSI analysis prior to the unwrapping is shown in Figure 4.6 on the left. Note the discontinuities as the phase jumps from zero to 2π as the phase $\Psi(x, y)$ is only obtained modulo 2π from PSI.

Possible error sources of PSI analysis are miss-calibrations of the phase shifter for algorithms of typ (1 - 3), quadratic nonlinearities of the phase shifter (1 - 3), detector nonlinearities (all), quantization errors of the detector (all), and vibrations (all). In gen-

[7] Excluding an exact value of π.

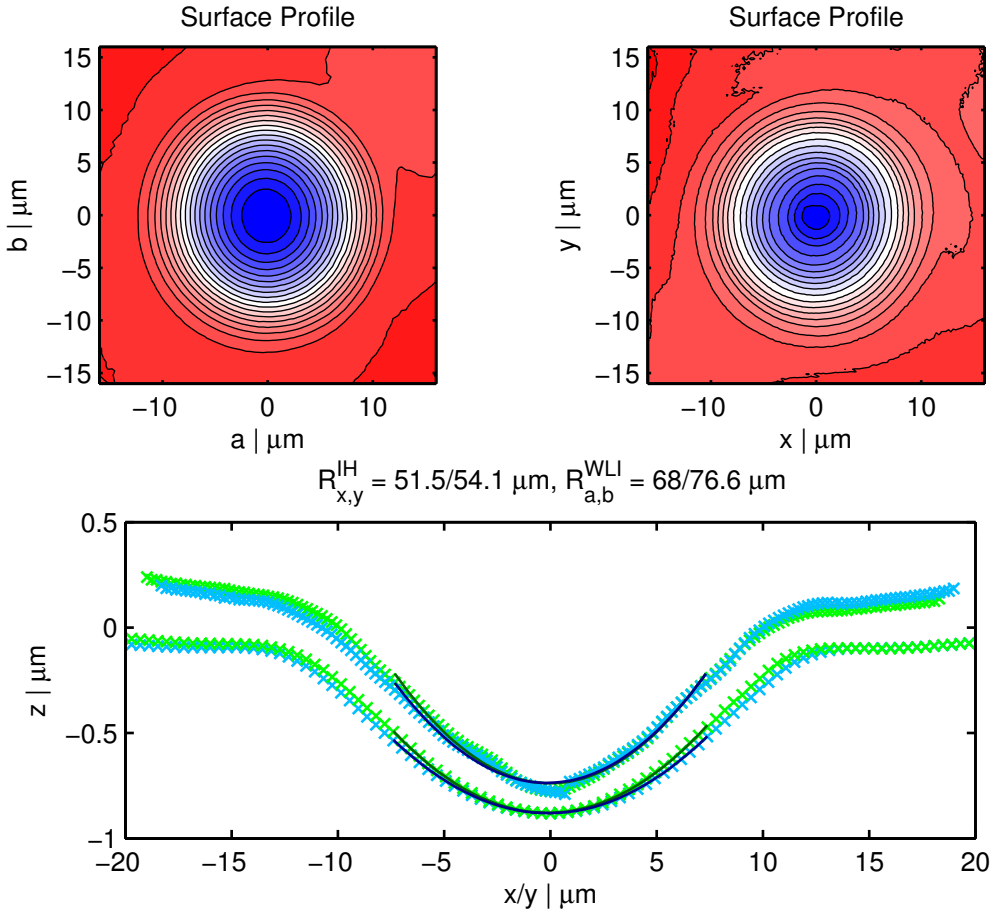

Figure 4.7: Left: Reconstructed surface profile of a fiber with $r \approx 60\,\mu\text{m}$ using a commercial profilometer. The cuts in the lower figure are offset for better visibility. **Right:** PSI analysis of the same fiber with the LIM. The cuts are offset for visibility. The different color of the planar part of the surface is caused by small spikes in the PSI analysis.

eral, algorithms with more images are less sensitive to errors. Interestingly, PSI also has applications in the detection of cold atomic samples [131, 132].

Phase Unwrapping

Subsequently the discontinuous wrapped $\Phi(x, y) \pmod{2\pi}$ phase obtained from PSI can be unwrapped to recover the true continuous phase $\Phi(x, y)$ of the interferometer. As for PSI, a large number of algorithms exist. An overview can be found in [128, 133, 134]. For the implementation presented here, we use an algorithm presented in [135]. The result of the unwrapping procedure is shown in Figure 4.6 on the right. This is the full surface profile $f(x, y)$, reconstructed from two interferometer images with different phases.

4.4 Interferometer Validation

As mentioned above, the reconstructed surface profile shows a residual oscillation. It was unclear if this is an effect of the PSI algorithm, the detection system or if the

structure is really present in the profile of the fiber. To validate the homebuilt interferometer, we compared the LIM with a commercial white light interferometer (WLI)[8]. A comparison with an atomic force microscope (AFM) is already presented in Philipp Christoph thesis [121], but for a much larger radius of curvature. Also there, residual oscillations in the PSI signal of the LIM were visible but less critical due to the large radius of curvature. As we moved to smaller radii of curvature, this effect became more pronounced and limits our ability to efficiently determine the radius of curvature.
The results of the comparison for a small radius of curvature are shown in Figure 4.7 side by side. On the left is the WLI data, on the right a PSI reconstruction of the LIM for the same fiber. The residual oscillations are not present in the data of the WLI, the processed fiber has a smooth concave feature with a radius of curvature of $r = 68.0/76.6\,\mu\text{m}$ in two perpendicular axes. The asymmetry is caused by a slight misalignment of the parabolic mirror[9]. For the LIM, the extracted radius of curvature depends strongly on the fit area. This is a result of the residual oscillation that always shows a dip in the center of the profile. Also visible in Figure 4.7 is a small phase jump in the center of the LIM profile, also degrading the determination or the radius.
To ensure that this is not an effect of the PSI algorithm we tried a different method using multiple images with unknown phases [136] with no improvement.

We believe that the performance of the interferometer is limited by the spatial resolution of the imaging system. With a magnification of twenty, a pixel corresponds to $5.2/20\,\mu\text{m} = 260\,\text{nm}$. The size of a concave feature is in the order of $20\,\mu\text{m}$ but the image changes from bright to dark over a distance of around eight pixels as can be seen in Figure 4.4. This is consistent with the measured resolution of $\approx 2\,\mu\text{m}$ of the imaging system. If the structures in the image are similar or smaller compared to the resolution of the system, the image is not the real image I_f of the fiber but rather the convolution of the fiber image with the point spread function PSF of the detection system I'_f [125]

$$I'_\text{f} = PSF * I_\text{f}. \tag{4.18}$$

This effect is only present in the imaging arm as the reference image I_ref is constant and therefore also the convolution with the PSF yields the original reference image[10]

$$I'_\text{ref} = PSF * I_\text{ref} = I_\text{ref}. \tag{4.19}$$

This convolution results in oscillations symmetric with respect to the shape of the processed feature. They are only present if there is a visible change in the image, not in the areas where the image is constant, e.g. outside the processed regions. This behavior is consistent with our observations.

[8] Nikon Eclipse LV150 with a CF Plan 20x/0.4 *NA* Mirau interferometer lens.
[9] A previous measurement with a well aligned parabolic mirror showed a near symmetric profile with $r = 65.8/66.8\,\mu\text{m}$.
[10] Each structure can be viewed as an effective aperture. A constant image is effectively an infinitely large aperture.

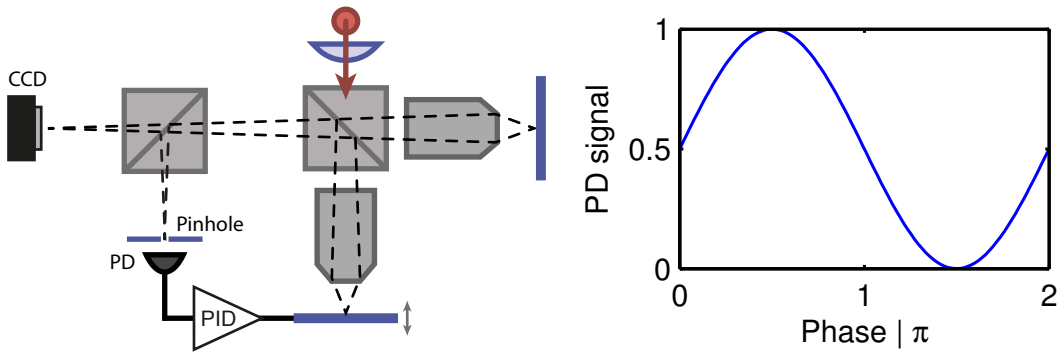

Figure 4.8: Left: Interferometer with added photodiode to set the phase of the interference image. **Right:** Expected photodiode signal

Therefore we plan to set up a dedicated detection LIM using high-*NA* microscope lenses. A *NA* of 0.5 would lead to a radial resolution of 0.793 µm at 650 nm detection wavelength, way beyond the currently realized system and even better than the commercial WLI where no oscillation was visible. Another benefit of a high-*NA* LIN is the decrease in depth of field. This will also reduce the focussing effect of the concave structure described above which may have a negative effect in the center of the profile.

4.5 Interferometer Improvement

One improvement which would pave the way for easy implementation of PSI algorithms with known phase steps is the use of a photodiode in combination with a piezo driven reference substrate as shown in Figure 4.8. A second beam splitter can be introduced to create a second image plane of the magnified fiber. This can be done by either installing it before or after the interference beam splitter (the case illustrated in Figure 4.8). A pinhole selects a small portion of the image, comparable to one pixel on the CCD camera and a photodiode is used to monitor the light. As the reference substrate is scanned, a sinusoidal oscillation should be visible. This signal could be used to calibrate and set the needed phases for a sequence of interference images used for PSI.

Furthermore, this setup could be used to lock the interferometer using the same short coherence source used for detection. Other implementations of locked LIM are based on a second light source like a He-Ne laser [137], a super luminescent diode [138] or a laser diode [139]. Locked interferometers can reduce the vibrations which are one mayor source of PSI errors. The rms error of the depth profile for a five step PSI algorithm is below 40 nm for low frequency vibrations with an amplitude of a quarter fringe [140] whereas PSI algorithms with less images are more sensitive.

For the application here, the lock might not be critical profile depth accuracy, it can be used to set the phase of the interferometer regardless of phase actuator non-linearity by changing the DC-offset of the lock.

4.6 Cleaving Angle

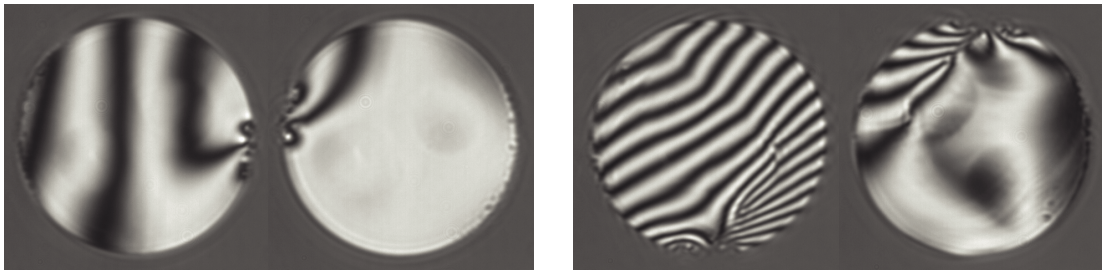

Figure 4.9: Left: Well cleaved PM fiber with an angle of $\theta \approx 0.2°$. Shown is the fiber and the fiber turned by 180°. **Right:** Cleaved PM fiber with an angle of $\theta \approx 0.7°$.

The interferometer is also used to determine the quality of the cleaved fiber. This angle is important if the fiber is to be used for a cavity as the beam is refracted away from the surface normal like in a APC fiber. The effect is discussed later on in Section 5.5.3. We use a Fujikura CT-04 manual cleaver which can produce nice clean cuts of $\theta < 0.3°$ as seen in Figure 4.9 if aligned properly. This realignment has to be done on a regular basis to ensure a good cleaving performance. The distortion on one side of the fiber is the crack caused by the cleaving process. Also visible are the stress cores of the PM fiber as circular structures in the interference fringes.

The cleave angle can be determined by comparing the number of interference fringes if the fiber is rotated by 180°. If there is no fringe visible in one setting and one fringe (dark to dark) if the fiber is rotated, the resulting cleaving angle is

$$2\theta = \arctan\left(\frac{\lambda/2}{d_{\text{fiber}}}\right) = 0.15°.$$

4.7 Conclusion

In the course of this thesis, a fiber processing and surface analysis system to fabricate and analyze concave features on fibertips with radii of curvature r from 25 µm to 500 µm [121] was set up. The results were validating using a commercial WLI and improvements to allow a more accurate determination of the radius of curvature are discussed.

Chapter 5

Asymmetric Fibercavities

In this chapter, all the necessary ingredients to realize asymmetric fiber cavities with high reflectivity on resonance are presented. An analytical model is developed, which gives insight into the optimal cavity parameters for different applications. Furthermore, this model is validated using numerical calculations. In the last part, the experimental realization of an asymmetric fiber Fabry-Pérot cavity is presented and compared to the analytical model.

The reflection and transmission properties of Fabry-Pérot cavities are based on the interference of light. It leads to the well known effect that all light of a symmetric, perfectly mode-matched cavity is transmitted on resonance.

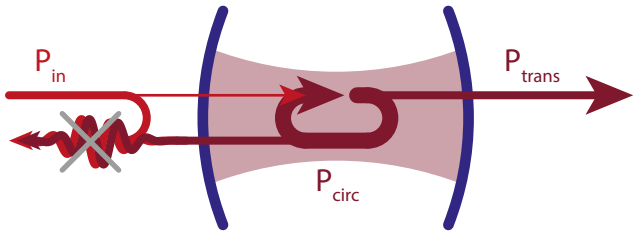

Figure 5.1: Sketch of a symmetric Fabry-Pérot cavity with perfect mode match. Shown is the input/circulating/transmitted power $P_{\mathrm{in}}/P_{\mathrm{circ}}/P_{\mathrm{trans}}$. The line thickness sketches the value of P.

Figure 5.1 shows a sketch of a symmetric Fabry-Pérot cavity. Most of the incoupling power, P_{in}, is promptly reflected off the incoupling mirror. A small part is transmitted and creates the amplified intra-cavity power P_{circ}. The intracavity power leaks through the incoupling and outcoupling mirror and interferes destructively on the incoupling side with the reflected part of P_{in} to zero. The transmitted power P_{trans} has the same value as P_{in} if losses are ignored and the mode match is perfect. If the cavity is asymmetric, which is realized by using an incoupling mirror with lower reflectivity, a larger part of the circulating power leaks out on the incoupling side. This results in a finite reflectivity on resonance.

In fiber-based cavities the in- and out-coupling fibers act as mode filters. This results in an unexpected behavior of asymmetric fiber cavities, which is discussed in detail in Section 5.2. The calculations were performed during this thesis and describe the parameters needed to create asymmetric fiber-based Fabry-Pérot cavities suited for the hybrid quantum system. As an introduction, some of the basic properties of Fabry–Pérot cavities are reviewed in Section 5.1 (see textbooks [116, 141]).

5.1 Properties of Fabry-Pérot Cavities

The shape and separation of the mirrors comprising a Fabry-Pérot cavity define the spatial mode in the cavity. At distinct distances between the two mirrors, the power transmitted through the incoupling mirror is enhanced creating the circulating intra cavity field. This periodic behavior is connected to the frequency modes of the cavity.

5.1.1 Spatial Mode

Fabry-Pérot cavities can be described by the dimensionless parameters g [141]:

$$g_i = 1 - \frac{L}{r_i}. \tag{5.1}$$

Here, r_i denotes the radius of curvature of the mirror i, $(i = 1, 2)$, and L the length of the cavity. A stable cavity must satisfy the stability equation:

$$0 < g_1 g_2 < 1. \tag{5.2}$$

The curvatures of the mirrors define the spatial mode by fixing the wavefront curvatures of the light field on the surfaces. Therefore, the waist w_0

$$w_0 = w_0\,(r_1, r_2, L) = \sqrt{\frac{L\lambda}{\pi}} \left(\frac{g_1 g_2 (1 - g_1 g_2)}{(g_1 + g_2 - 2 g_1 g_2)} \right)^{1/4} \tag{5.3}$$

of the spatial mode depends on the length, the radii of curvature r_i of the mirrors and the wavelength λ [141]. If the incoupling and outcoupling mirrors are concave, the waist of the mode is located in between the mirrors. The mode expands towards the mirrors, and the spot size on the mirror w_1 can be calculated by [141]:

$$w_1 = \sqrt{\frac{L\lambda}{\pi}} \left(\frac{g_2}{g_1 (1 - g_1 g_2)} \right)^{1/4}. \tag{5.4}$$

To determine the spot radius w_2 on mirror two, the indices have to be exchanged. In a planar concave (PC) cavity ($r_1 = \infty$, $r_2 > 0$) the waist w_0 is located on the planar mirror $w_0 = w_1$. Such a case is shown in Figure 5.2. Enlarging the distance between the two mirrors changes the waist w_0 as well as the spot size on the second mirror w_2. The waist has a maximum at $L = r_2/2$ and goes to zero when $L \to 0$ and $L \to r_2$. At these points, the cavity is unstable (see Equation 5.2).

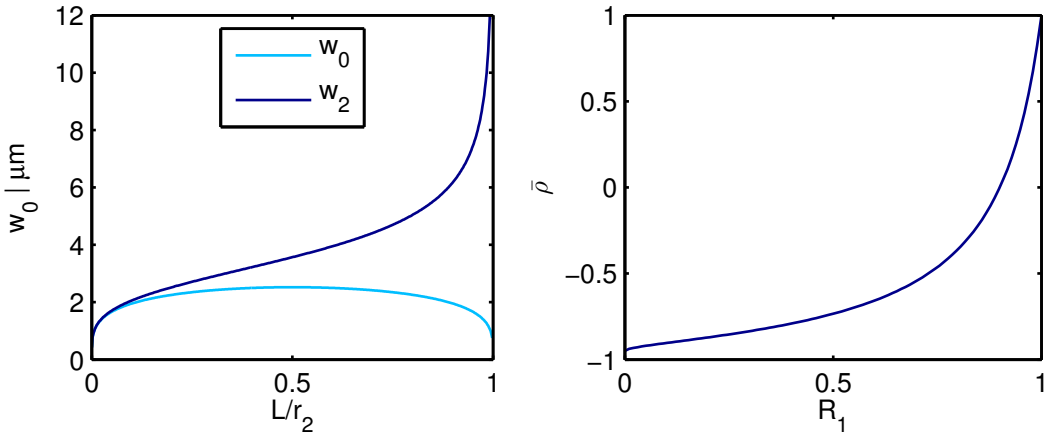

Figure 5.2: Left: Spot sizes on the mirrors of a planar concave cavity with a radius of curvature of $r_2 \approx 50\,\mu\text{m}$. For planar concave cavities the waist is located on the planar mirror. **Right:** Field reflectivity on resonance $\bar{\rho}$ plotted for $R_2 = 0.9$. If R_1 is smaller than R_2, $\bar{\rho}$ is negative. This is the case for an asymmetric cavity if the beam is coupled in the cavity through the less reflective mirror. For the case of a symmetric cavity ($R_1 = R_2$) the reflectivity on resonance is zero

For short cavity lengths the divergence of the cavity mode is small ($w_2 \approx w_0$). In contrast to the behavior of the waist w_0, the spot size w_2 does not have a maximum. It increases monotonically with the cavity length and diverges at $L = r_2$. For a PC geometry at the point of largest waist ($L = r_2/2$), the mode of the cavity on the outcoupling mirror is $w_2 = \sqrt{2}w_0$.

5.1.2 Frequency Modes

Dependent on the exact mirror distance, constructive interference can create the amplified intra cavity field that is the source of the on-resonance transmission effect.

Transmission

Mirrors are commonly described by the power reflectivity and transmittance rather than the field reflectivity and transmittance. In the following, all field properties are marked with a bar symbol, all power properties without:

$$R = \bar{R}^2 \qquad \text{and} \qquad T = \bar{T}^2.$$

If the mirrors are lossless, which we assume in this section, $R + T = 1$. Looking at the sum over $2 \cdot q + 1$ passings through a Fabry-Pérot, the transmitted field E_t is

$$E_\text{t} = \sum_{q=1}^{\infty} \bar{T}_1 \bar{T}_2 \left(\bar{R}_2 \bar{R}_1\right)^{q-1} e^{i(2q-1)\phi} e^{i2\pi(q-1)} E_\text{in} \tag{5.5}$$

$$= \frac{e^{i\phi} E_\text{in} \bar{T}_1 \bar{T}_2}{1 - e^{2i\phi} \bar{R}_1 \bar{R}_2}. \tag{5.6}$$

The incoupling mirror is marked with the index 1 whereas the outcoupling mirror is marked by the index 2. Here, the phase ϕ

$$\phi = 2\pi L/\lambda = kL = L\omega/c$$

is the phase shift per passing of the cavity. It is acquired by the field propagating over the length L with frequency ω. The resonance condition is fulfilled if $\phi = n \cdot 2\pi$ with $n \in \mathbb{N}$. In this case, the fields in the sum of Equation 5.5 add up, leading to constructive interference. The transmitted intensity $I_\mathrm{t} = |E_\mathrm{t}|^2$ is:

$$\frac{I_\mathrm{t}}{I_\mathrm{in}} = \left|\frac{E_\mathrm{t}}{E_\mathrm{in}}\right|^2 = \left|\frac{e^{i\phi}\sqrt{(R_1-1)(R_2-1)}}{1-e^{2i\phi}\sqrt{R_1R_2}}\right|^2. \tag{5.7}$$

Note that the transmission through the cavity is symmetric with respect to R_1 and R_2. Switching the two indices corresponds to a change of the incoupling side. If the cavity is asymmetric, the transmission signal can not be used to determine which is the higher and which is the lower reflecting mirror.

Reflection

The sum over the reflected fields yields

$$\begin{aligned} E_\mathrm{r} &= E_\mathrm{in}\bar{R}_1 + \sum_{q=2}^{\infty} \bar{T}_1\bar{T}_1 \left(\bar{R}_2\right)^{q-1} \left(\bar{R}_1\right)^{q-2} e^{i2(q-1)\phi} e^{i(2q-3)\pi} E_\mathrm{in} && (5.8)\\ &= E_\mathrm{in}\bar{R}_1 + \frac{e^{2i\phi}E_\mathrm{in}\bar{R}_1T_1}{-1+e^{2i\phi}\bar{R}_1\bar{R}_2}, && (5.9) \end{aligned}$$

and the reflected intensity $I_\mathrm{r} = |E_\mathrm{r}|^2$ can be calculated:

$$\frac{I_\mathrm{ref}}{I_\mathrm{in}} = \left|\frac{E_\mathrm{ref}}{E_\mathrm{in}}\right|^2 = \left|\frac{\sqrt{R_1}-e^{2i\phi}\sqrt{R_2}}{1-e^{2i\phi}\sqrt{R_1R_2}}\right|^2. \tag{5.10}$$

Again, the resonance condition is fulfilled if $\phi = n \cdot 2\pi$. In contrast to the field transmittance (equation 5.6), the field reflectivity (equation 5.9) is not symmetric with respect to a change of the incoupling side.

Reflectivity on Resonance

Taking a close look at Equation 5.10, we define the normalized field reflectivity on resonance $\bar{\rho}$

$$\bar{\rho} = \frac{\sqrt{R_1}-\sqrt{R_2}}{1-\sqrt{R_1R_2}}, \qquad \bar{\rho} \in [-1,1], \tag{5.11}$$

such that

$$\frac{E_\mathrm{ref}(\phi = n\cdot 2\pi)}{E_\mathrm{in}} = \bar{\rho}. \tag{5.12}$$

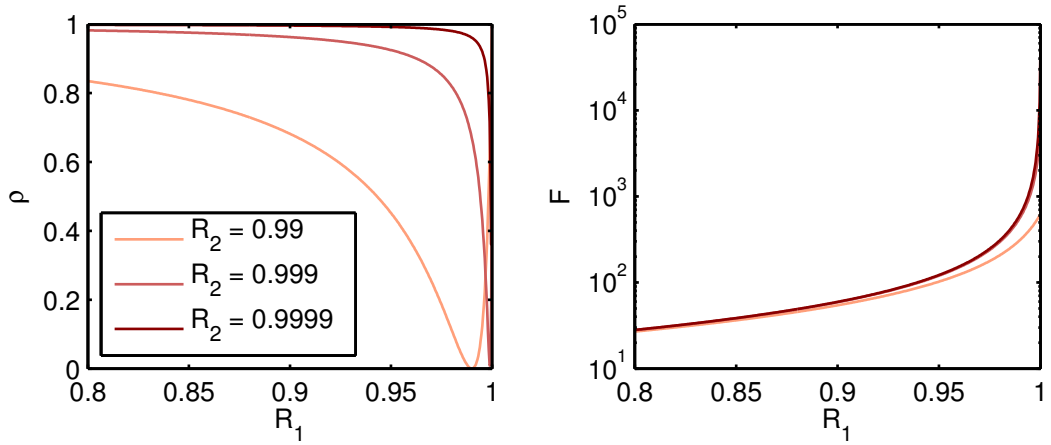

Figure 5.3: Left: Power reflectivity on resonance ρ for three different outcoupling mirror reflectivities R_2. The power reflectivity drops to zero for the case of a symmetric cavity ($R_1 = R_2$). **Right:** Finesse of the cavity for the same reflectivities R_2 as in the left plot. The curves for $R_2 = 0.999$ and $R_2 = 0.9999$ overlap.

The parameter $\bar{\rho}$ is plotted in Figure 5.2 for a reflectivity of the incoupling mirror $R_1 = [0, 1]$ and a fixed reflectivity of the outcoupling mirror $R_2 = 0.9$. If the incoupling mirror is less reflective than the outcoupling mirror ($R_1 < R_2$), the field reflectivity on resonance $\bar{\rho}$ is negative. The sign changes at the point of a symmetric cavity ($R_1 = R_2$) to a positive value ($R_1 > R_2$), which corresponds to a coupling into an asymmetric cavity from the higher reflecting side. In experimental signals the power reflectivity

$$\rho = \bar{\rho}^2$$

plays an important role. Figure 5.3 shows the power reflectivity on resonance for different values of R_2. It vanishes for $R_1 = R_2$, which corresponds to a symmetric cavity. The higher the reflectivity of the second mirror R_2, the more asymmetric the cavity becomes for a given value of R_1.

Finesse

The finesse $\mathcal{F}$ of a Fabry-Pérot cavity is defined as the rate $\mathcal{F} = \nu_{\mathrm{fsr}}/\delta\nu$ with the free spectral range $\nu_{\mathrm{fsr}} = c/2L$ and linewidth $\delta\nu$. It yields:

$$\mathcal{F} = \frac{\pi \sqrt[4]{R_1 R_2}}{1 - \sqrt{R_1 R_2}}. \tag{5.13}$$

The finesse is only a function of the reflectivity of the mirrors and symmetric with respect to R_1 and R_2. It is plotted in Figure 5.3 for the same parameters as the power reflectivity on resonance.
The achievable finesse of a cavity is limited by the dominant loss channel, which is the lower reflecting mirror in a lossless asymmetric cavity. In contrast to the power reflectivity on resonance plotted on the left in Figure 5.3, the finesse depends mostly on the

reflectivity of the lower reflecting mirror R_1.[1] As a result, the reflectivity R_2 sets a limit for the achievable finesse $\mathcal{F}$ at a given power reflectivity ρ.

If losses l are introduced into the cavity, the finesse is rewritten as

$$\mathcal{F} = \frac{\pi \sqrt[4]{R_1 R_2 (1-l)}}{1 - \sqrt{R_1 R_2 (1-l)}}. \tag{5.14}$$

Sources of these losses can be clipping of the beam or contaminations of the mirrors.

5.1.3 Higher Order Modes

In the case of imperfect mode match, the non-matched part can be described as a composition of higher order transverse modes. These modes have a different resonance frequency and are reflected by the cavity if it is resonant with the ground mode. This is true as long as the higher transverse modes with number l, m; ν_{lmn} [141],

$$\nu_{lmn} = \frac{c}{2L}\left[n + \frac{1+l+m}{\pi} \cdot \arccos\left(\sqrt{g_1 g_2}\right)\right] \tag{5.15}$$

have a larger shift in resonance frequency than the line width $\delta\nu$ of the cavity.

$$\frac{\nu_{010} - \nu_{000}}{\delta\nu} = \frac{\arccos\left(\sqrt{g_1 g_2}\right)}{\pi} \cdot \mathcal{F} > 1. \tag{5.16}$$

Equation 5.16 is valid if $\mathcal{F} > 4$ in the case of a PC cavity with $L = R_2/2$.

[1] The only clear deviation in the plot is for $R_2 = 0.99$ and for high R_1. In this case the cavity is almost symmetric. If $R_1 > R_2$, R_2 would be the dominant loss channel.

5.2 Asymmetric Fiber Cavities

To couple light efficiently into an optical fiber, the spatial mode of the beam and the fiber mode has to be matched. For a fiber-based cavity this means that the reflected and transmitted fields have to be overlapped with the respective fiber modes to calculate the reflected and transmitted intensities that can be measured at the end of the fiber.

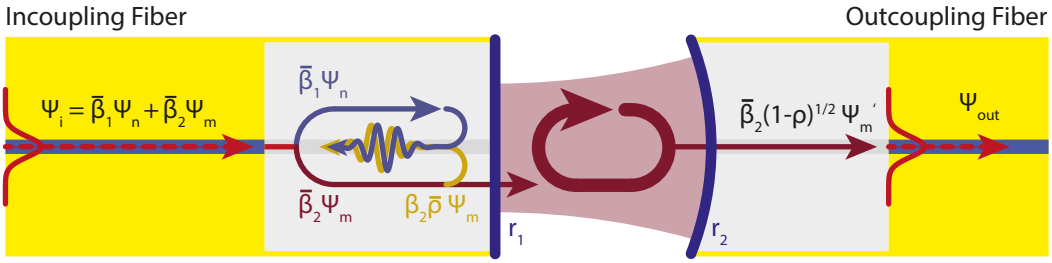

Figure 5.4: Sketch of the fields coupled into a fiber Fabry-Pérot cavity. The gray area indicates the virtual zone between the end of the fiber and the coating. The input field ψ_i is split into a mode-matched ψ_m and a non-mode-matched part ψ_n. While the first enters the cavity and is subsequently reflected with the field reflectivity on resonance $\bar{\rho}$, the latter is non-resonant and directly reflected. These two fields interfere. The field transmitted through the cavity ψ'_m has to be matched with the mode of the outcoupling fiber ψ_{out}.

Figure 5.4 shows an abstract picture of a fiber Fabry-Pérot cavity with imperfect mode match. The input field ψ_i, guided in the incoupling fiber, is split into a part matched with the cavity mode ψ_m and a non-mode-matched part ψ_n:

$$\psi_i = \bar{\beta}_1 \psi_n + \bar{\beta}_2 \psi_m. \tag{5.17}$$

This is valid as the higher spatial modes are non-resonant with the cavity (see section 5.1.3). They are reflected from the cavity with the off-resonant reflectivity, which is higher than the reflectivity of the incoupling mirror r_1. In this section, the following parameters are calculated:

- **The total reflected power.** It is the sum of the non-mode-matched part and the light reflected by the cavity. See Section 5.2.1.
- **The mode match of the reflected field and the fiber mode.** It is the interference of the non-mode-matched part and the light reflected by the cavity, overlapped with the incoupling fiber mode. See Section 5.2.2.
- **The transmitted power.** This can be calculated from the reflected power if losses are ignored. See Section 5.2.3.
- **The mode match of the transmitted field with the outcoupling fiber.** See Section 5.2.4.

The theory was developed during this thesis and is necessary to understand and realize asymmetric fiber-cavities, a system not yet reported in the literature. The focus here lies on PC cavities as this geometry is preferable for the application envisioned and

enables perfect mode match. The mode match is the critical parameter for asymmetric fiber cavities and much more important compared to symmetric fiber cavities as will become evident in this section.

The parameters $\bar{\beta}_i$, introduced in the field decomposition (see Equation 5.17), are complex numbers, which account for the mode match. The fields ψ_i, ψ_n, and ψ_m are normalized:

$$\int |\psi_i|^2 \, \mathrm{d}A = \left|\bar{\beta}_1\right|^2 \int |\psi_n|^2 \, \mathrm{d}A + \left|\bar{\beta}_2\right|^2 \int |\psi_m|^2 \, \mathrm{d}A = 1. \tag{5.18}$$

The mode match β is defined via the power in the mode-matched part of the light ψ_m; $\beta = 1$ corresponds to perfect mode match.

$$\beta = \left|\bar{\beta}_2\right|^2 = \left|\bar{\beta}_1\right|^2 - 1. \tag{5.19}$$

5.2.1 Power Reflectivity

The power of a field ψ can be calculated by its absolute square and integration over the area

$$P = \int |\psi|^2 \, \mathrm{d}A. \tag{5.20}$$

The mode-matched part of the light (the field that is interacting with the cavity) is reflected with the field reflectivity on resonance $\bar{\rho}$ as described by Equation 5.11. This part interferes with the non mode-matched part that is promptly reflected from the cavity as sketched in Figure 5.4. The reflected field ψ_r is therefore:

$$\psi_r = \bar{\beta}_1 \psi_n + \bar{\rho}\bar{\beta}_2 \psi_m. \tag{5.21}$$

The reflected power P_{ref} can therefore be calculated to

$$\begin{aligned} P_{\mathrm{ref}} &= \int |\psi_r|^2 \, \mathrm{d}A && (5.22)\\ &= \int \left|\bar{\beta}_1\right|^2 |\psi_n|^2 + \left|\bar{\rho}\bar{\beta}_2\right|^2 |\psi_m|^2 + 2\bar{\rho} \cdot \mathrm{Re}[\bar{\beta}_1 \bar{\beta}_2^* \psi_m \psi_n] \mathrm{d}A && (5.23)\\ &= 1 - \beta\,(1 - \rho)\,. && (5.24) \end{aligned}$$

The matched and not-matched functions are orthogonal, therefore also the integral of the real part is zero. P_{ref} is as expected from an asymmetric cavity and plotted in Figure 5.5 on the left side for three different values of ρ. A closer look at the reflected spatial intensity distribution $|\psi_r|^2$ of the cavity,

$$|\psi_r|^2 = \left|\bar{\beta}_1\right|^2 |\psi_n|^2 + \left|\bar{\rho}\bar{\beta}_2\right|^2 |\psi_m|^2 + 2\bar{\rho} \cdot \mathrm{Re}[\bar{\beta}_1 \bar{\beta}_2^* \psi_m \psi_n], \tag{5.25}$$

shows that the mixed term, which drops out during the integration, has an effect on the spatial mode of the reflected field. Remember that the field reflectivity on resonance $\bar{\rho}$ changes sign when the role of the mirrors R_1 and R_2 are reversed. This results in a dramatic change of the spatial mode of the reflected field. The total reflected power P_{ref}

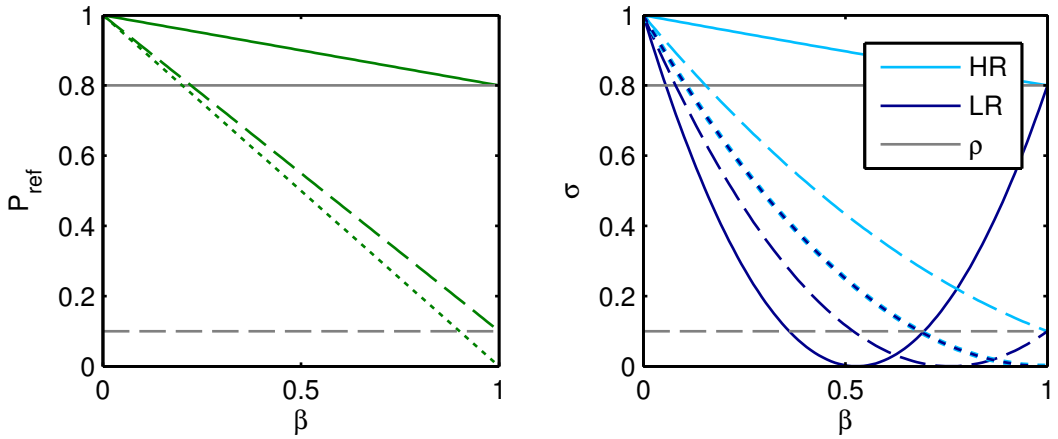

Figure 5.5: Left: Reflected power of an asymmetric Fabry-Pérot Cavity with imperfect mode match β for different asymmetries $\rho = 0.8/0.1/0$ (solid/dashed/short dashed). The gray horizontal line indicates the respective reflectivity on resonance ρ. **Right:** Effective reflectivity on resonance for an asymmetric FC with imperfect mode match for different asymmetries. The solid/dashed/short dashed lines show the observed signal for a field reflectivity of $\rho = 0.8/0.1/0$. Light blue shows the reflectivity when coupling from the higher reflective side, dark blue from the lower reflective side. For the case of $\rho = 0$, both lines overlap. The gray horizontal line indicates the respective reflectivity on resonance ρ.

is not affected as the expression scales with $\rho = \bar{\rho}^2$.

For a regular free-space cavity the change of the spatial mode is not very important. The reflected power, typically measured by a photodiode has the behaviour described by P_{ref}. In the case of a fiber cavity, the reflected mode ψ_r has to match the fiber mode to be guided and finally measured at the end of the fiber. Otherwise, light is lost in the fiber and the measured reflected power is lower than in the free space case. This mode overlap is discussed in the next section.

5.2.2 Reflection Mode Match

The power coupling efficiency η between two fields can be calculated by

$$\eta = \left| \int \psi_1 \psi_2^* \mathrm{d}A \right|^2 . \tag{5.26}$$

To calculate the reflection mode match η_{ref}, the reflected field ψ_r (equation 5.21) has to be overlapped with the fiber mode ψ_i (equation 5.17):

$$\begin{aligned} \eta_{\text{ref}} &= \left| \frac{1}{\sqrt{P_{\text{ref}}}} \int \psi_r \psi_i^* \mathrm{d}A \right|^2 && (5.27) \\ &= \left| \frac{1}{\sqrt{P_{\text{ref}}}} \int \left(\bar{\beta}_1 \psi_n + \bar{\rho}\bar{\beta}_2 \psi_m\right) \cdot \left(\bar{\beta}_1 \psi_n + \bar{\beta}_2 \psi_m\right)^* \mathrm{d}A \right|^2 && (5.28) \\ &= \frac{1}{P_{\text{ref}}} \left|1 - \beta + \bar{\rho}\beta\right|^2 . && (5.29) \end{aligned}$$

The mixed terms drop out during the integration as ψ_m and ψ_n are defined as orthogonal functions. Multiplying the reflected power P_{ref} with the mode match factor η_{ref} defines the signal σ_{ref} that can be measured after the reflected cavity mode is transmitted through the fiber:

$$\sigma_{\text{ref}} = \eta_{\text{ref}} P_{\text{ref}} = |1 - \beta + \bar{\rho}\beta|^2 \,. \tag{5.30}$$

This important result is shown in Figure 5.5 on the right side and illustrate the necessity for optimal mode match for asymmetric fiber cavities. Dependent on the sign of $\bar{\rho}$, which corresponds to a change of the incoupling side, a very different behavior is observed. For a asymmetric cavity, coupled from the lower reflective side, the interference effect can change the spatial mode of the field reflected by the cavity in such a way that the signal observed at the end of the fiber is zero. Only if $\beta = 1$, the reflectivity on resonance, defined by the asymmetry of the mirrors is achieved. This effect becomes more critical the smaller $\bar{\rho}$ (note that $\bar{\rho} < 0$).

5.2.3 Power Transmittance

The power transmittance can be easily calculated as $P_{\text{ref}} + P_{\text{trans}} = 1$ is fulfilled due to energy conservation.

$$\begin{aligned} P_{\text{trans}} &= 1 - P_{\text{ref}} && (5.31)\\ &= \beta\,(1 - \rho) && (5.32) \end{aligned}$$

5.2.4 Transmission Mode Match

In addition to the mode match of the reflected light, which is dominated by the interference effect, we can calculate the mode match of the transmitted light. The transmitted field is $\bar{\beta}_2\sqrt{1-\rho}\cdot\psi'_m$. No interference is present, leading to a more intuitive result:

$$\begin{aligned} \eta_{\text{trans}} &= \left| \frac{1}{\sqrt{P_{\text{trans}}}} \int \left(\sqrt{1-\rho}\cdot\bar{\beta}_2\psi'_m \right) \cdot \psi^*_{\text{out}} \mathrm{d}A \right|^2 && (5.33)\\ &= \left| \int \psi'_m \psi^*_{\text{out}} \mathrm{d}A \right|^2 . && (5.34) \end{aligned}$$

The total observed transmission signal is therefore:

$$\sigma_{\text{trans}} = \eta_{\text{trans}} P_{\text{trans}} = \eta_{\text{trans}} \beta\,(1 - \rho)\,. \tag{5.35}$$

The transmission signal into the curved fiber is also of interest as the cavity is intended to be used from both sides, e.g. for the PDH lock. The expected incoupling efficiency from the curved side will be very similar to the transmission signal. In a normal realization, the higher reflective fiber will be the curved one. Therefore any interference effects described above are uncritical and the reflected signal, when coupled from the higher reflective curved side, scales linearly with the mode match (see Figure 5.5).

5.2.5 Overlap of Gaussian Beams

The equations 5.30 and 5.35 are expressions for the transmission and reflection of an asymmetric fiber Fabry-Pérot cavity. They depend on the mode match β of the cavity mode with the mode emitted by the fiber and the overlap of the cavity mode and the mode of the outcoupling fiber η_2.

5.2.6 Incoupling Mode Match β

The mode overlap K_{ax} of two axially aligned gaussian beams can be calculated [142] when knowing the spot size w and the curvature R of the beams at a specific reference plane:

$$K_{\mathrm{ax}}(w_a, w_b, R_a, R_b) = \frac{4}{(w_b/w_a + w_a/w_b)^2 + (\pi w_a w_b/\lambda)^2 (1/R_b - 1/R_a)^2}. \tag{5.36}$$

If the waist of two beams is at the same position, which is used as the reference plane, the wave front curvature is $R = \infty$ for both beams. The overlap simplifies to

$$K_{\mathrm{ax}}(w_a, w_b) = \frac{4}{(w_b/w_a + w_a/w_b)^2}$$

for this case. The waist w_{f} of the beam emitted by a planar cut fiber fiber is fixed by the NA and the wavelength λ used:

$$w_{\mathrm{f}} = \frac{\lambda}{0.82 \cdot \pi \cdot NA}. \tag{5.37}$$

For the incoupling efficiency of a planar concave fiber cavity $w_a = w_{\mathrm{f}}$ whereas $w_b = w_0(L, r_2)$ is the cavity waist (see equations 5.37 and 5.3). The mode match β^{PC} is

$$\beta^{\mathrm{PC}} = \beta\,(L, r_2) = \frac{4}{(w_0(L, r_2)/w_{\mathrm{f}} + w_{\mathrm{f}}/w_0(L, r_2))^2} \tag{5.38}$$

and depends on the length L and the radius of curvature r_2 of the curved mirror.

5.2.7 Transmission Mode Match η_{trans}

To calculate the transmission mode match η_2 we have to consider the lensing effect of the outcoupling fiber, which is curved with r_2. It acts as a divergent lens and can be modeled as a thin lens with negative focal length $f = r_2/(n_f - 1)$ with n_f being the refractive index of the fiber. This can be described in terms of the complex beam parameter [142]

$$q = \frac{1}{R} - \frac{i\lambda}{\pi w_0^2} \tag{5.39}$$

before (q_1) and after (q_2) the lens as

$$\frac{1}{q_2} = \frac{1}{q_1} - \frac{1}{f} = \frac{1}{q_1} - \frac{n_f - 1}{r_2}. \tag{5.40}$$

The beam in the fiber (q_1) has a wavefront with infinite radius of curvature R, therefore $\mathrm{Re}\,[1/q_1] = 0$. The curved surface changes only the wavefront curvature, not the spot size. The wavefront radius of curvature R after refraction from the curved surface is therefore:

$$R = \left[\mathrm{Re}\left(\frac{1}{q_2}\right)\right]^{-1} = \frac{r_2}{n_f - 1}. \tag{5.41}$$

Now, η_2 can be calculated when taking the second mirror as the reference plane:

$$\eta_2 = K_{\mathrm{ax}}(w_2, w_{\mathrm{f}}, r_2, -r_2/(n_f - 1)). \tag{5.42}$$

Here, w_2 is the spot size of the cavity mode on the outcoupling mirror. The minus sign in Equation 5.42 is a result of the orientation of the surface r_2.

5.2.8 Radial Offset

If a radial offset of length x_0 is introduced, the mode match is reduced by an additional exponential factor. In this case, the mode match K_{offset} [142] is

$$K_{\mathrm{offset}} = K_{\mathrm{ax}} \exp\left(-2\left(\frac{x_0}{\delta_{\mathrm{off}}}\right)^2\right). \tag{5.43}$$

Here, δ_{off} is the offset parameter

$$\delta_{\mathrm{off}} = \sqrt{\frac{\left(w_{0a}^2 + w_{0b}^2\right)^2 + (\lambda \Delta z/\pi)^2}{w_{0a}^2 + w_{0b}^2}} \tag{5.44}$$

and depends on the waists w_{0a} and w_{0b} and the axial distance between the location of the two waists Δz. For the case of a PC cavity, the waist of the fiber w_{f} and the waist of the cavity mode w_0 are at the same axial position, therefore $\Delta z = 0$. The mode match $\beta_{\mathrm{offset}}^{\mathrm{PC}}$ can therefore be written as

$$\beta_{\mathrm{offset}}^{\mathrm{PC}}(L, r_2, x_0) = \beta^{\mathrm{PC}}(L, r_2) \cdot \exp\left(-2\left(\frac{x_0^2}{\sqrt{w_f^2 + w_0(L, r_2)^2}}\right)^2\right). \tag{5.45}$$

The exponential reduction of the mode match with radial misalignment poses restrictions to the radial alignment precision necessary for the cavity.

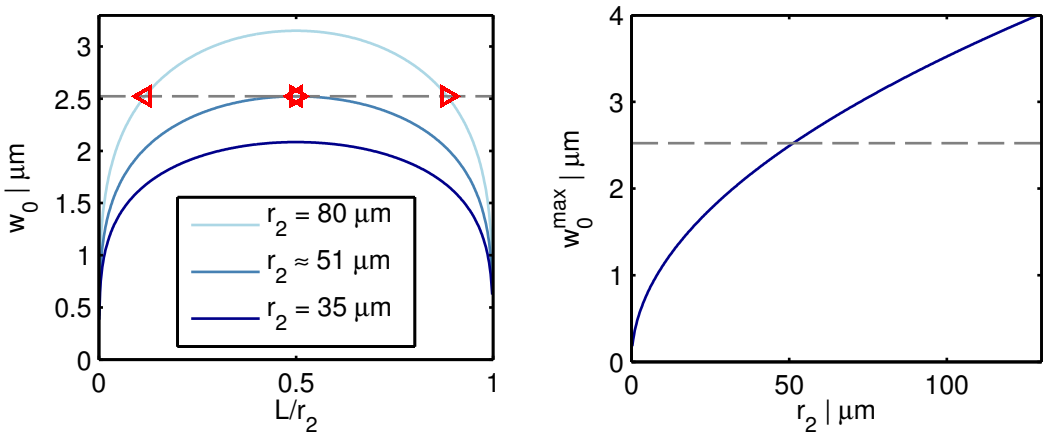

Figure 5.6: Left: Waist of a PC cavity for different r_2 with L scaled with their respective r_2. The maximal waist of the cavity is always located at $L = r_2/2$. The dashed line indicates the waist of a beam emitted from a PM780 fiber. ◁/▷ indicate the first/second mode match point. **Right:** Maximal waist at $L = r_2/2$ of a planar concave Fabry-Pérot cavity dependent on the radius of curvature of the second mirror r_2. The dashed line indicates the waist of a beam emitted from a PM780 fiber.

5.3 Optimal Cavity Parameters

The necessity of optimal mode match results in strong restrictions for the cavity geometry. In a concave-concave (CC) cavity, $\beta = 1$ is not possible due to the lensing effect mentioned above. It moves the virtual waist w_0 of the emitted beam into the fiber. The fiber and the cavity mode may have the same spot size w but the different sign of the wave front curvature R always results in $\beta < 1$ (see Figure 5.7).
In a PC fiber cavity $R = \infty$ is always valid at the planar incoupling mirror. Therefore $\beta = 1$ can be realized if the spot emitted by the fiber w_f has the same size as the cavity mode $w_1 = w_0$ on the incoupling mirror. We will concentrate on PC geometries first.

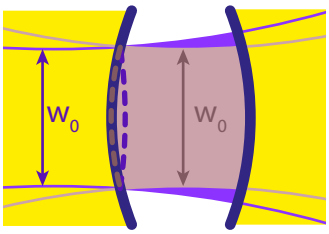

Figure 5.7: Sketch of the lensing effect caused by a curved incoupling fiber. The curved dashed lines indicate the wave front curvature.

As discussed above, the waist w_0 in a PC cavity depends on the length L and the radius r_2. Furthermore, it has a maximum at $L = r_2/2$. If the waist of the fiber is smaller or equal than this maximum, $\beta = 1$ is possible. This situation is depicted in Figure 5.6. The intersection points where $w_\mathrm{f} = w_0$ will be referred to as **mode match points**. The first mode match point is close to $L = 0$, the second mode match point close to $L = r_2$. If

$$w_0\,(L = r_2/2) = w_\mathrm{f}, \tag{5.46}$$

both mode match points overlap and the cavity has a **stable mode match**. In this geometry a length change only weakly affects the cavity waist as $w_0\,(L = r_2/2)$ is a

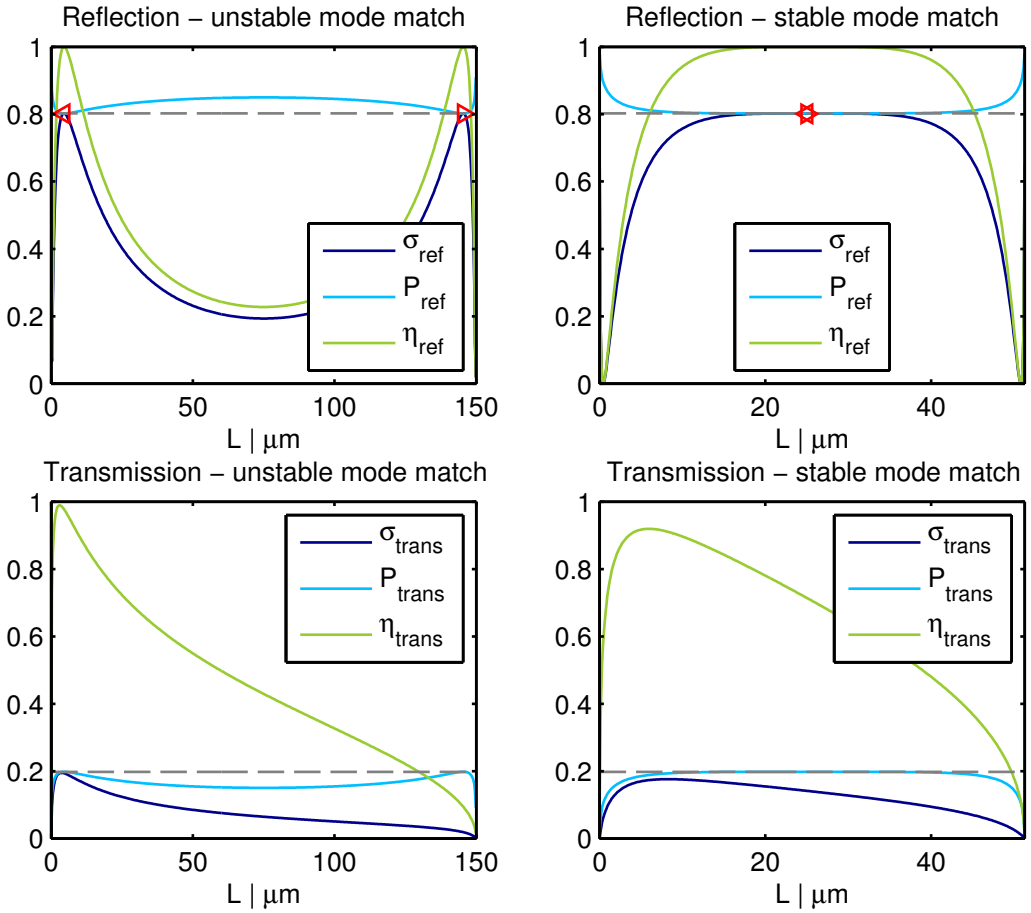

Figure 5.8: Expected asymmetric fiber Fabry-Pérot cavity signals for two different radii of curvature r_2. Shown is the reflected power P_{ref}, the mode match of the reflected field and the incoupling fiber mode η_{ref}, and the observed signal at the end of the fiber σ_{ref}. The transmission plots show the respective transmission properties. **Left column:** Unstably matched cavity with $r_2 = 150\,\mu\mathrm{m}$. **Right column:** Cavity with stable mode match ($r_2 = 51.28\,\mu\mathrm{m}$). The dashed gray line indicates the power reflectivity on resonance $\rho = 0.8$ in the reflection the corresponding $\rho = 1 - 0.8$ in the transmission. ◁/▷ indicate the first/second mode match point.

maximum. For Thorlabs PM-780 fiber at 780 nm this corresponds to

$$r_2 = 51.28\ \mu\mathrm{m} = r_s. \tag{5.47}$$

5.3.1 Reflection Signal

Asymmetric fiber cavities are **only** usable at the mode match points. This is the result of the interference effect that dominates the behavior of η_{ref}. The observed signal σ_{ref} as a function of the length L is illustrated in Figure 5.8. Only at the mode match point, the light reflected by the cavity is guided in the incoupling fiber and the reflectivity on resonance ρ, given by the reflectivities of the mirrors, is achieved. For a unstable matched cavity, the length has to be controlled precisely as the peak of σ_{ref} is very narrow. Dependent on the radius r_2, the observed signal σ_{ref} can go to zero in between

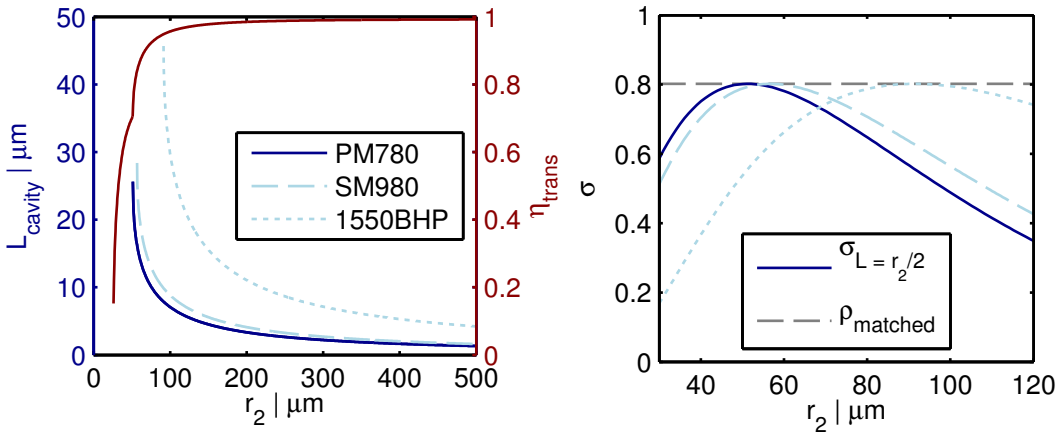

Figure 5.9: Left: Position of the first mode match point against the radius of the curved mirror in blue. The longest possible cavity is the stable matched one with $L = r_2/2$. In comparison the dashed/dotted line shows the same plot for a single mode fiber for 1064/1550 nm. The red curve shows the transmission mode match at the first mode match point for a PM780 incoupling fiber. **Right:** In contrast to the left plot, which shows the position of the mode-matched point, the observed signal at $L = r/2$ is plotted for the corresponding fibers.

the mode match points. For the cavity with stable mode match, the cavity is usable over a substantially broader length range.
The results presented here do not include losses in the cavity. At long cavity length, for example at the second mode match point for a cavity with unstable mode match, the spot size on the outcoupling mirror w_2 is very large. This can lead to clipping losses at the limited size of the processed structure and ultimately at the fiber diameter.

5.3.2 Transmission Signal

The transmission of the unstable and stable matched cavity have a similar behavior. With increasing length, the spot size on the outcoupling mirror w_2 increases. The aforementioned lensing effect of the curved fiber also negatively affects the transmission mode match. No interference effect is present resulting in an overall similar behavior between the stable and unstable matched cavity. The very low transmission for large L limits the usability at the second mode match point.
The outcoupling fiber used is a Thorlabs 780HP[2] fiber which, has a slightly smaller mode field diameter than the incoupling fiber.

5.3.3 Maximal Length

The stable matched cavity is the longest possible mode-matched PC cavity. Although a perfect mode match is possible at the first mode match point, the absolute position of the first mode match point moves to shorter length as r_2 increases (see Figure 5.9 on

[2]Single mode fiber with a NA of 0.13. If not mentioned otherwise, this fiber is used as the outcoupling fiber.

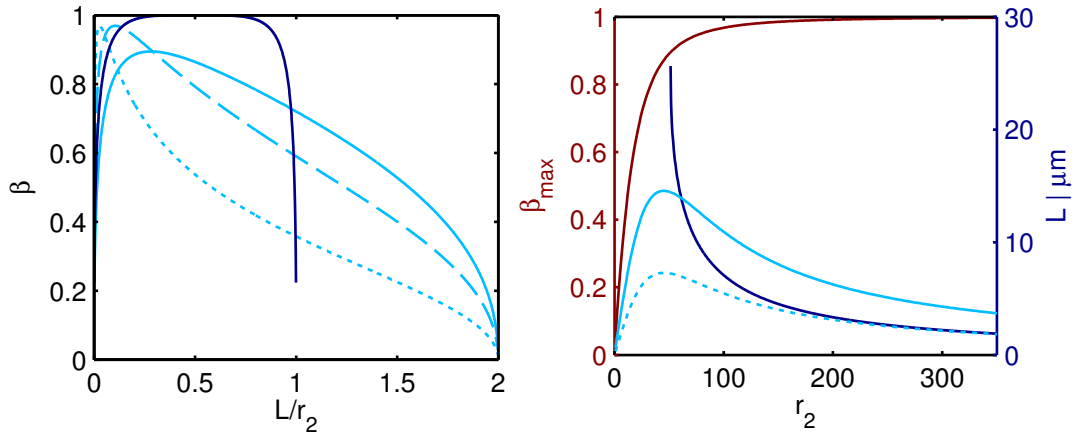

Figure 5.10: Left: Incoupling mode match β for PC and CC fiber cavity designs. Shown is a PC cavity with stable mode match ($r_2 = 51.28\,\mu\text{m} = r_m$) in dark blue and CC cavities with $r_1 = r_2$ for $r_2 = r_m/2r_m/4r_m$ respectively in blue (solid/dashed/dotted). For CC designs the total length L is double that of PC cavities. **Right:** Maximum of β for CC cavities shown in red. The length corresponding to the maximum of β is depicted in solid light blue and divided by two in dotted blue. The dark blue line corresponds to the length of a mode-matched PC cavity as shown in Figure 5.9.

the left). The maximal length depends on the fiber and wavelength used.

Unfortunately, the change in position of the first mode match point with respect to r_2 is very large. It is therefore interesting to analyze the deviation of $\sigma(L = r_2/2)$ with respect to r_2 (see Figure 5.9 on the right). If r_2 is 10 µm larger than r_s, the change of $\sigma(L = r_2/2)$ is about 3 pp. The first mode match point in this case moved from $L \approx 25\,\mu\text{m}$ to $L \approx 14\,\mu\text{m}$.

If a long cavity is not of interest and the cavity length can be precisely aligned, it can be beneficial to fabricate a cavity with unstable mode match for use at the first mode match point. In such a configuration the transmission of this cavity is better than the stable matched cavity since the maximum transmission and the first mode match point overlap. The behavior of the transmission mode match η_{trans} is shown alongside the position of the first mode match point in Figure 5.9. A transmission mode match close to one is possible in a geometry of $r_2 = 200\,\mu\text{m}$ and $L = 3.5\,\mu\text{m}$. In such a configuration, almost no light would be lost. The deviation from one for large r_2 is due to the slightly different NA of the outcoupling fiber compared to the incoupling fiber.

5.3.4 Planar Concave & Concave Concave Cavities

As mentioned above, in CC geometries β is always smaller than one due to the lensing effect of the curved fiber. Furthermore, a CC cavity only has one maximum of β compared to the two of a PC cavity if $r_2 > r_m$. The spot size on the incoupling mirror r_1 increases monotonically with the cavity length in contrast to the waist, which has a

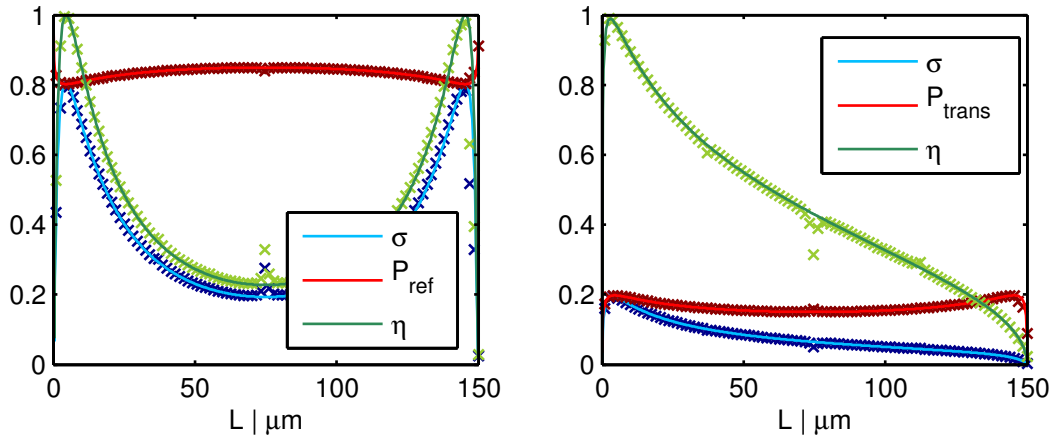

Figure 5.11: Comparison of the analytic solution (solid lines) for the observed signal σ, the reflected power P_{ref} and the mode match η with the numerical simulation (crosses). Shown **left** is the reflection signal, **right** the transmission signal for different cavity lengths.

maximum. This incoupling mode match $\beta^{\mathrm{CC}} = K_{\mathrm{ax}}(w_{\mathrm{f}}, w_1, -r_2/(n_f - 1), r_2)$ is depicted in Figure 5.10 on the left for a CC cavity with identical radius of curvature ($r_1 = r_2$) in comparison to the PC cavity geometry (β^{PC}, see Equation 5.38).

With increasing radius r_1, the maximum of β^{CC} increases as the lensing effect decreases. This maximal value of β^{CC} alongside the corresponding length L is shown in Figure 5.10 on the right. The longest realization of a CC cavity where β has a maximum is located at $r \approx 50\,\mu\mathrm{m}$. Unfortunately, at this length, the maximum of β^{CC} is still severely limited by the lensing effect and the length is only half that of the stable matched PC geometry. For large radius r, CC and PC cavities show an identical behavior but at $L^{\mathrm{CC}} = 2L^{\mathrm{PC}}$.

The findings can be summarized as:

- A stable matched PC cavity is the longest asymmetric fiber cavity.
- If high transmission or high incoupling efficiency from the higher reflective side are important it is beneficial to use the first stable mode match point and $r_2 > 200\,\mu\mathrm{m}$.
- A CC geometry increases the cavity length by a factor of two with little negative effect for the incoupling efficiency if $r_2 > 200\,\mu\mathrm{m}$, while still being significantly shorter than the PC cavity with stable mode match.

5.4 Numerical Simulations with OSCAR

To validate the model presented in the Section above we also performed numerical simulations with the MATLAB script OSCAR[3]. It is capable of calculating the spatial

[3] by Jerome Degallaix, v3.14. http://www.mathworks.com/matlabcentral/fileexchange/20607-oscar

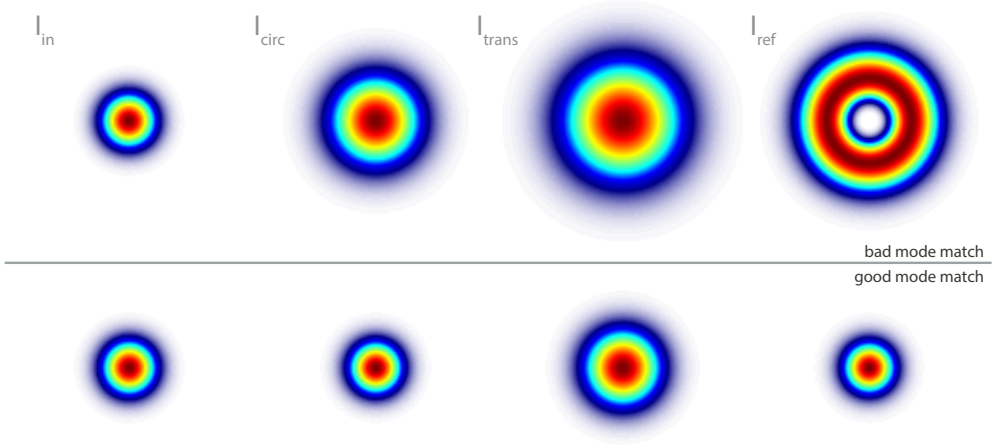

Figure 5.12: Left to right: Normalized input/circulating/transmitted/reflected field of an asymmetric planar concave cavity with bad mode match, calculated with OSCAR. **Upper line:** Asymmetric cavity with bad mode match ($r_2 = 150\,\mu m$, $L = 30\,\mu m$). **Lower line:** Asymmetric cavity with stable mode match ($r_2 = 50\,\mu m$, $L = 25\,\mu m$). The input, circulating, and the reflected mode are located at the incoupling mirror, whereas the transmitted mode is located after the outcoupling mirror. The incoupling field has a waist of $w = 2.5\,\mu m$.

modes of cavities formed by mirrors of arbitrary surface profile.
A comparison of the analytic expressions presented above for both the reflected and transmitted signal for different cavity lengths is shown in Figure 5.11. They show almost perfect agreement except at few distinct lengths ($L = r_2/2$, $L = r_2/4$, and $L = 3r_2/4$). The source of these deviations is unknown.

To gain further insight into the interference effect described in equation 5.25, Figure 5.12 shows the incoming, circulating, transmitted and reflected field as calculated by OSCAR for a badly mode-matched asymmetric cavity. The circulating mode, located at the incoupling mirror, is larger than the incoupling mode, indicating the bad mode match. In contrast, the reflected mode, also shown at the incoupling mirror, shows a significant dip in the center due to the interference effect. As described above, this reflected mode has to be overlapped with the incoupling mode which results in a large losses. For reference, the second line in Figure 5.12 shows the case for a stable matched cavity. Here, the reflected field and the input field overlap perfectly.

5.5 Experimental Realization

In the following Section experimental results of the realization of asymmetric fiber Fabry-Pérot cavities are presented. To test different incoupling and outcoupling fibers without glueing, the fiber were clamped[4] on a manual pitch/yaw[5], and a piezo driven xyz-stage[6] to position the fibers and scan the cavity along the x-axis. The processed and coated fiber were spliced to FC/APC connectors to couple light into them.

The measured transmission and reflection signal of an asymmetric PC fiber Fabry-Pérot cavity is shown in Figure 5.13. Each data point corresponds to a scan over at least two cavity resonance obtained with a oscilloscope. From these traces, of which two are included in Figure 5.13, the reflection and transmission on resonance (σ_{ref} and σ_{trans}), and the finesse are extracted. For each length, the cavity alignment was optimized using the yz-axes.

A good agreement with the theoretical model at short cavity lengths ($L < 20\,\mu\mathrm{m}$) is evident for a radius of curvature of $r_2 = 66\,\mu\mathrm{m}$. The transmission signal is scaled by a factor of 0.23, probably due to imperfect centering of the processed feature on the outcoupling fiber core. Such a reduction would correspond to a radial misalignment of $x_0 \approx 2.5\,\mu\mathrm{m}$ (see section 5.5.1). Note that the curved fiber used here is the one presented in Figure 4.5 with a measured radius of curvature of $r_2 \approx 50\,\mu\mathrm{m}$. Like in the validation section 4.4, the in-house interferometer seems to give a radius of curvature that is too small. The data shown in Figure 5.13 is more compatible with $r_2 = 66\,\mu\mathrm{m}$.

For the model, which is included as the solid line, the externally determined reflectivity of $R_2 \approx 0.9982$ (see appendix, Section D.5) is used, whereas the reflectivity of $R_1 \approx 0.928$ is calculated from the median of the finesse for $L < 20\,\mu\mathrm{m}$, $\mathcal{F} \approx 80$. These values differ slightly from the calculated reflectivities (see appendix, Section D.4) of $R_1 = 0.9208$ and $R_2 = 0.9996$, which is no surprise as the coatings are produced in a rather simple in-house soft coating machine.

The length of the cavity is determined by calibrating the differential drive using a microscope camera[7]. This measurement is shown in Figure 5.14. Each data point corresponds to one image of the microscope camera. For each image, the derivative along the fiber axis is taken, and the image is summed perpendicular to the cavity axis. This yields a vector with one peak and one dip for the two fiber ends. Therefore it is important to ensure that the fibers are aligned along one pixel axis of the camera. The distance of the fiber is determined by fitting gaussians to the peak and dip and taking the fiber width

[4] Thorlabs HFF001/M
[5] Thorlabs MBT401/M
[6] Thorlabs MAX311/M with BPC203 controller. The closed loop functionality of the MAX311/M was not used. The limited scan speed of $f \approx 100\,\mathrm{Hz}$ was not an issue and the clamped construction proved to be stable enough to perform reproducible measurements.
[7] Distelkamp-Electronic Di-Li 2001-P, measured resolution of $\delta_{\mathrm{m}} \approx 5.5\,\mu\mathrm{m}$.

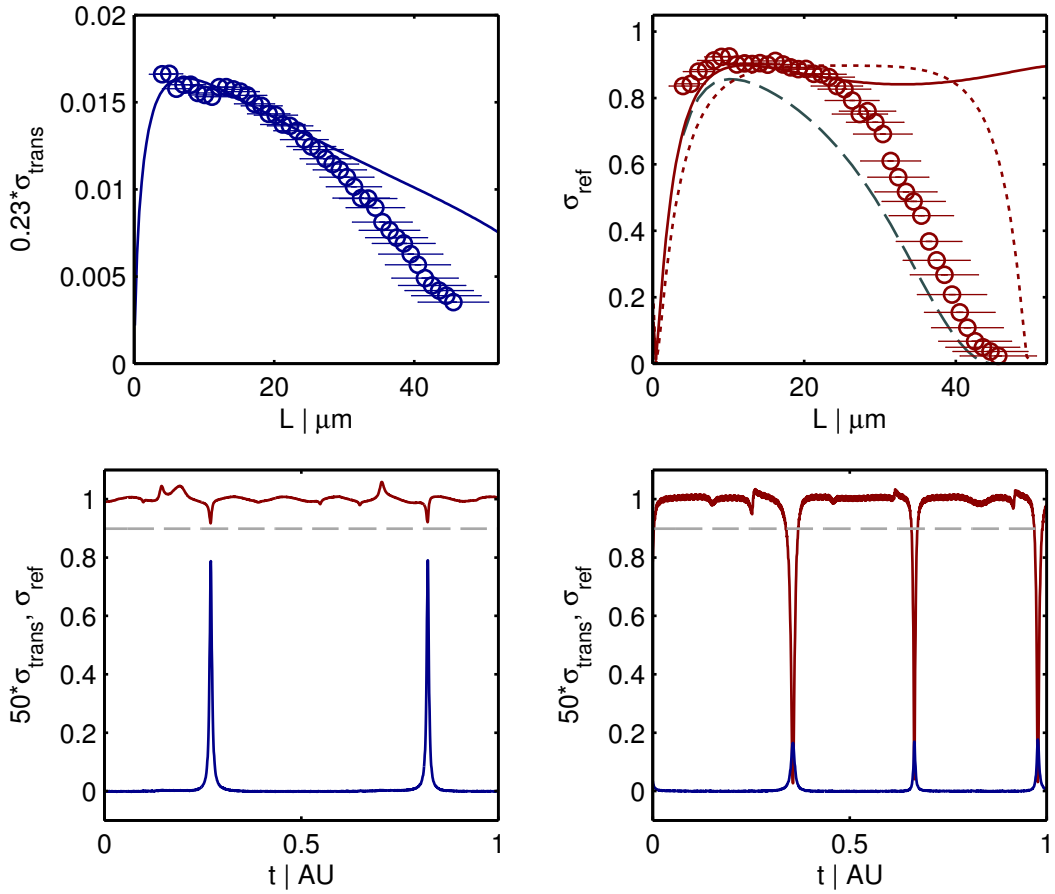

Figure 5.13: Experimental realization of a asymmetric PC fiber Fabry-Pérot cavity. **Top Left:** Transmission signal σ_{trans}. The incoupling fiber is coated with 9 (R_1), the outcoupling with 19 layers (R_2) of MgF and ZnS. The solid line is the theoretical model for $r_2 = 66\,\mu\text{m}$. The data points are the extracted transmission values from a scan across the cavity resonance. The error bars indicate the 50 % bounds of the length determination (Figure 5.14). **Top Right:** The corresponding reflection signal in red. Additionally, the dotted red line corresponds to $r_2 = 50\,\mu\text{m}$, the value determined by the LIM (Figure 4.5). The dashed grey line indicates the expected reflection signal if losses are introduced in the form $R_2(1-l)$ using the fit shown in Figure 5.14. **Bottom Left:** Scans of the cavity length for $L = (8 \pm 2)\,\mu\text{m}$. Shown in blue/red is the transmission/reflection signal. The transmission signal is scaled by a factor of 50. The dashed gray line indicates the expected reflectivity on resonance of $\rho \approx 0.9$. **Bottom Right:** As left but for $(46 \pm 5)\,\mu\text{m}$.

as a reference value of 125 µm. The uncertainty of the linear fit δ_{fit} used to calibrate the micrometer drives is the main uncertainty in the length determination. It is larger than errors induced by the limited knowledge of the reference length, which is specified as $\pm\delta_{\text{f}} = 2\,\mu\text{m}$. Adding this error with the limited resolution of the microscope δ_{m} results in a additional length error $\delta L' = \pm L \cdot (\delta_{\text{m}}^2 + \delta_{\text{f}}^2)^{0.5}/125\,\mu\text{m}$. This error is also included in Figure 5.14 but only has a very small effect. Therefore the 50 % uncertainty of the linear fit is given as the error value throughout this section.

The difference from the data and the model can be explained as an increase of losses with increasing cavity length (see Figure 5.14 on the right). A clear trend towards an

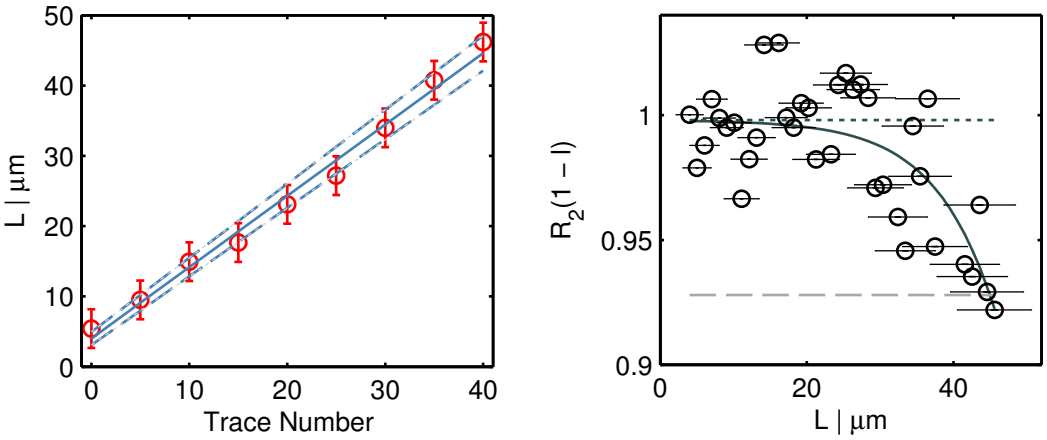

Figure 5.14: Left: Calibration of the differential drives using images of the fiber distance. Each data point shows an extracted length from an image. The error bars indicate the resolution of the microscope. The solid line is a linear fit to the data. The dashed lines indicate the 50 % error bounds δ_{fit} of the linear fit. The dotted light gray lines shows the bounds including the error of the width determination of the fiber due to the limited optical resolution. **Right:** Increase of losses for different cavity lengths. The dotted line indicates the externally determined reflectivity of R_2. For each cavity length, the finesse was determined using the traces shown in Figure 5.13. The dashed line shows the value of R_1 which was chosen to be $R_1 = 0.928$ compatible with the median of the finesse of $\mathcal{F} \approx 80$ for $L < 20\,\mu\text{m}$. The solid line indicates a fit of a Fermi distribution to $R_2(1-l)$ to determine the strength of the losses. The data points are measured values of $R_2(1-l)$ calculated from the finesse with $R_1 = 0.928$ using Equation 5.14. The error bars are the 50 % bounds of the length determination.

increase of l with increasing length L is present. For $L \approx 40\,\mu\text{m}$, the losses in the cavity and the losses due to the limited reflectivity of the incoupling mirror R_1 are identical, which results in an effective symmetric cavity with a reflection signal on resonance of zero. The analytic model with the fitted behavior of $R_2' = R_2(1-l)$, while keeping R_1 constant, is also included in Figure 5.13. It shows a gradual change from an asymmetric cavity with high reflectivity on resonance to a symmetric cavity. The shape qualitatively agrees with the behavior of the reflection signal.
In similarity to this feature, also the transmission signal deviates for $L > 20\,\mu\text{m}$. The drop of the transmission is lower than the theoretical curve while $\sigma_{\text{trans}} \neq 0$ for $\sigma_{\text{ref}} = 0$ is also consistent with the explanation that losses cause this deviation.

5.5.1 Radial Alignment

A radial change in position of the two fibers changes the mode match as discussed in Section 5.2.5. It is important to check for the robustness against radial misalignment. The relative position of the two fibers is analyzed using images obtained with the microscope camera and the fiber width as a length reference as described above. The results are presented in Figure 5.15 on the left side. A clear maximum at perfect alignment is visible. The transmission signal with a FWHM of $\Delta x^t_{\text{rad}} \approx 4.5\,\mu\text{m}$ is much less sensitive to radial misalignment than the reflectivity on resonance with a FWHM of $\Delta x^r_{\text{rad}} \approx 2\,\mu\text{m}$. This measurement shows that it is important to align the asymmetric

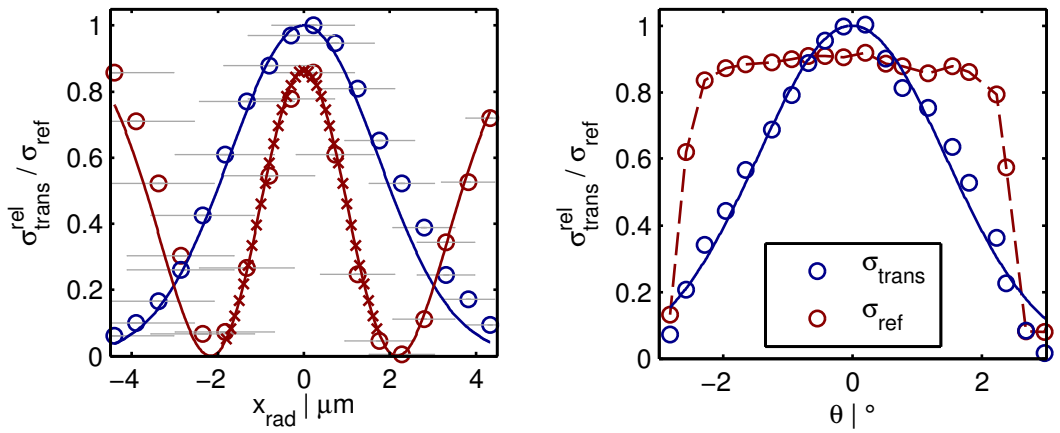

Figure 5.15: Left: Radial displacement as a function of the transmission (blue) and reflection (red) signal for $L \approx 25\,\mu m$. The error bars correspond to the 50 % bounds of the position uncertainty. The solid lines are the expected behavior according to Equation 5.45 with the transmission scaled to one. Additionally, the crosses indicate a numerical simulation of the reflection signal with OSCAR. **Right:** Angular dependence on the relative transmission and absolute reflection signal. The solid line is a gaussian fit to the transmission signal with the data and model scaled to one.

cavity with sub-micrometer precision. A radial misalignment of ± 200 nm already leads to losses of 3.2 %.

The decrease and subsequent increase of the reflectivity on resonance can be understood remembering the signal shown in Figure 5.5. If the fiber is radially displaced, the mode match decreases and σ_{ref} becomes smaller. Due to the minimum, σ_{ref} increases again if the radial displacement becomes large enough. Most of the light is promptly reflected off the incoupling mirror and not interacting with the cavity resulting in a high σ_{ref}. Figure 5.16 shows the reflected and transmitted mode of the cavity as the incoupling mode is moved from the bottom upwards. While the transmitted mode shape is not affected, the reflected mode shows a strong distortion. Again, the bad overlap of the reflected mode with the incoupling fiber mode leads to a stronger sensitivity for the reflected signal on resonance σ_{ref} compared to the transmitted signal σ_{trans}.

To ensure that these results are correct we performed a numerical calculation with a modified OSCAR code to radially move the grid on which the incoupling beam is defined on. These results show excellent agreement (see Figure 5.15).

5.5.2 Angular Alignment

To cover all degrees of freedom, robustness against angular misalignment was also studied. In this measurement the angle of the two fibers is changed by a defined value using the pitch/yaw stage and the cavity is realigned with the xy-translation stage. Positioning the fiber end at the rotation point of the pitch/yaw stage enables the measurement to be performed without changing the cavity length. Again a calibration was done using

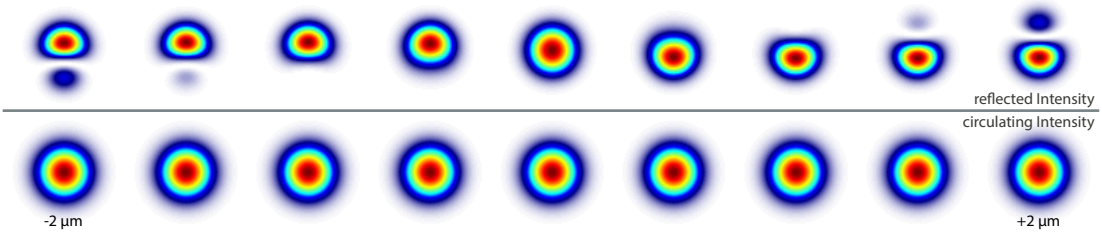

Figure 5.16: Upper line: Calculated normalized reflected mode for a misalignment of $x_{\mathrm{rad}} = -2\,\mu\mathrm{m}$ to $2\,\mu\mathrm{m}$ using OSCAR. **Lower line:** Corresponding transmitted mode.

images obtained with the microscope camera. The results are presented in Figure 5.15 on the right. A large plateau for the reflectivity on resonance is visible. It spans roughly over $\pm 2°$. In contrast to the radial misalignment, the transmission with a FWHM of $\Delta x_\theta^t \approx 3.4°$ is more sensitive to angular misalignment. As described above, the transmission signal measured here also corresponds to the efficiency that light can be coupled into the fiber cavity from the higher reflective side, which will be used in the setup later on. To ensure efficient incoupling a sub-degree angular alignment is necessary.

5.5.3 Cleave Angle

Unfortunately, the cleave angle has two negative effects on the mode match of the cavity. The beam is refracted away from the surface normal when the light is coupled into the cavity, similar to a FC/APC fiber but the geometric cavity axis is defined by the surface normal. Therefore efficient incoupling is not possible any more (see Figure 5.17).

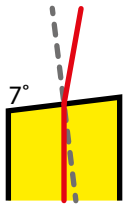

Figure 5.17: Effect of cleave angle. Grey is the surface normal that defines the cavity axis, red indicates the light path.

To get an idea of the cleave-angle importance of the incoupling fiber we created a fiber cavity from a coated outcoupling fiber with $R_2 \approx 0.998$ and $r_2 \approx 50\,\mu\mathrm{m}$ with two differently cut uncoated incoupling fibers ($R_1 = 0.04$). Such a cavity is highly asymmetric with $\rho = 0.997$ and has a very low finesse of $F = 1.75$.

One cleaved fiber has an angle of $\theta \approx 0.2°$ whereas the bad cleaved fiber has an angle of $\theta \approx 0.7°$. We chose to use non-coated incoupling fibers to avoid any effect of different coating qualities on the two fibers. The extracted reflection and transmission signals are shown in Figure 5.18. σ_{trans} is reduced by approximately 15 % for the fiber with $\theta \approx 0.7°$ compared to the fiber with $\approx 0.2°$. The reflection signal of the worse cut fiber does not reach the same level as the well cleaved one and has more jumps, probably due to the worse mode match.

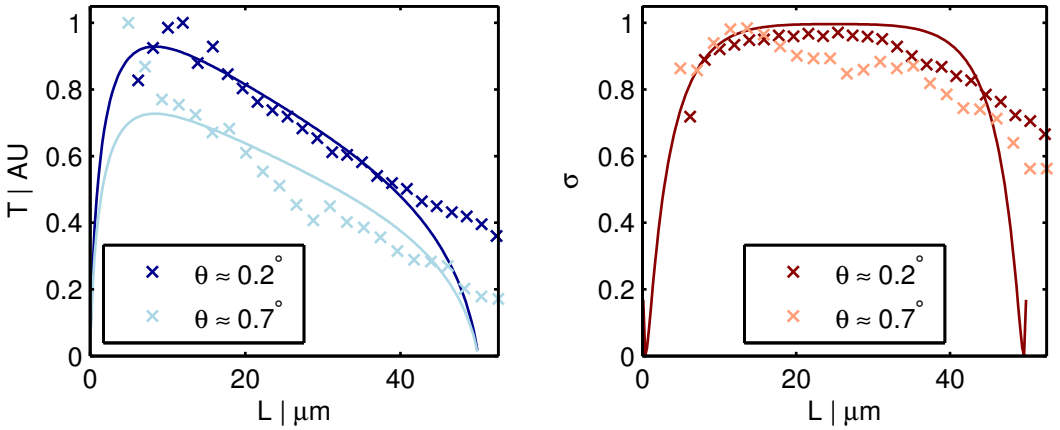

Figure 5.18: **Left:** Transmission signal of two different incoupling fibers with the identical outcoupling fiber. **Right:** Corresponding reflection signal. The crosses show to the measured data points, while the solid curves are the analytical model with $r_2 = 50\,\mu\text{m}$ and the reflectivities stated in this section. The fibers used here are shown in Figure 4.9.

5.6 Conclusion

In this chapter we presented all the necessary ingredients to create asymmetric fiber Fabry-Pérot cavities. With the asymmetry new challenges come into play, mainly the need for perfect mode match. Therefore planar concave cavities are ideally suited to create such asymmetric cavities. With the need for excellent mode match, the requirements for alignment are very high, too. The presented results show that radial alignment of $\pm 200\,\text{nm}$ and a sub-degree angular alignment is necessary to ensure a minimal amount of light loss.

Chapter 6

Room Temperature MiM System

In this chapter, the experimental realization of an asymmetric fiber-based MiM system is presented. The experimental setup is sketched and first measurements of key parameters such as the mechanical Q factor and the frequency shift of the cavity with respect to the membrane position are presented.

The asymmetric fiber cavities described above are used to create an asymmetric fiber-based MiM system. This is done in a room temperature vacuum chamber, which is sketched in Figure 6.1.

6.1 Experimental Setup

One fiber is glued into a v-groove[1] and onto a shearing piezo[2]. It is used to scan the cavity length and enables locking of the cavity to a laser. The second fiber is glued into a v-groove and clamped into a five-axis alignment stage. After the cavity is aligned, the v-groove is glued onto a aluminum block that is mounted onto a translation stage[3] using UV curable glue[4] and the alignment stage removed. The translation stage is used to retract the fiber to allow the insertion of a membrane. Fine positioning of the membrane is achieved using a ring piezo whereas the membrane can be coarsely moved by a second translation stage[5] (not shown in Figure 6.1). It was planned to mount the membrane in a mirror mount to enable angular alignment but the vacuum mirror mount[6] did not work properly so the membrane was mounted for a first trial experiment on a fixed mount.
The whole system is mounted in a vacuum chamber[7] with an IGP[8], two power feed

[1] OZ optics VGC-1-250-10.4-3.8-1-SW
[2] Noliac CSAP02 2 pieces stack
[3] Mechonics MS.030.3090
[4] Vacuum compatible EPO-TEK ET-OG154-1-0057
[5] Mechonics MS.030.0890
[6] Newport AG-M050NV6
[7] Kimball Sperical Octagon 2x160 8x40
[8] Agilent VacIon Plus 20

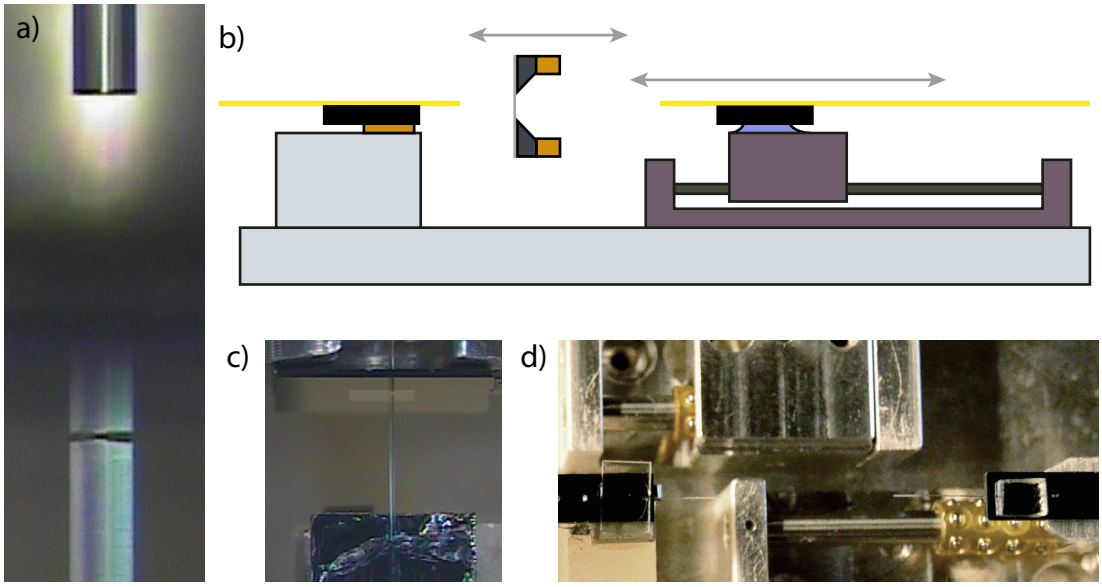

Figure 6.1: **a)** Image of the MiM system. Visible is the fiber mounted on the shearing piezo and its reflection in the membrane (lower fiber) and the fiber mounted on the translation stage (upper fiber). **b)** Sketch of the room temperature MiM system. Figure adapted from [144]. **c)** Smaller magnification version of a). Visible is the membrane frame, the groove which the fiber is glued into (lower end of the picture), and the fiber mounted on the translation stage (top). **d)** Picture of the fiber cavity assembly without the membrane holder and with retracted fiber (right). The membrane holder would be mounted on the translation stage at the top of the image.

throughs[9], a gauge[10], angle valve[11], and a swagelock flange[12]. The swagelock is used as a two-fiber feedthrough using a teflon ferrule [143], and the angle valve connects the system to a turbo pump for prepumping. A pressure of 1.7×10^{-7} mbar is achieved with the valve closed and the IGP active.

The strict alignment requirements described in Section 5.5.1 were not known during the design of this system [144] and make it very difficult to realize a asymmetric MiM system. Small contractions during the bonding sequence substantially affect the cavity alignment (see Figure 6.2).

At the start, the cavity shows a reflectivity on resonance of $\sigma_{\text{ref}} \approx 0.8$. After three minutes, the cavity was realigned using the five axis stage as a degradation was already visible. Once the clamp was removed at minute fourteen, σ_{ref} dropped to 0.64. The cavity degraded further to an unusable $\sigma_{\text{ref}} = 0.16$ over the course of three days. It was possible to realign the cavity with one of the base plate screws used to mount the plate to the bottom flange of the vacuum chamber. The observed σ_{ref} dependent on the torque used to mount the screw is shown in Figure 6.2 on the right. This alignment was also reproducible as can be seen at the data point with the error bar. Using this technique, it was possible to realize a MiM system in this setup by retracting the fiber, inserting

[9] Each 8 pins, 5kV DC, 50 Ampere, Pfeiffer
[10] Pfeiffer PKR251
[11] VAT 54032-GE02-0002
[12] DN40CF, 1/8 inch

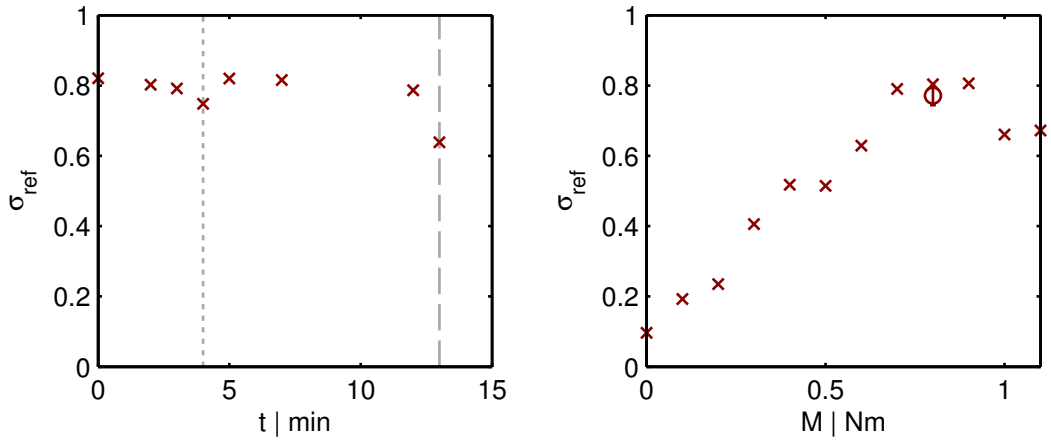

Figure 6.2: **Left:** Reflectivity on resonance σ_{ref} against the curing time of the UV epoxy. At the three minutes, (dotted vertical line) the cavity was realigned and at fourteen minutes (dashed vertical line) the clamp was removed. **Right:** Possibility to realign the cavity using one screw of the base plate. Visible is the reflection on resonance σ_{ref} against the torque setting of the wrench. The cross with error bar shows the reproducibility of four attempts to realign the cavity.

the membrane mount, approaching the membrane to the fixed fiber, and closing the cavity again.

6.2 Coupling Laser System

The first measurements were performed with parts of the coupling laser system, based on a TiSa[13] laser. Solid state lasers are a superior choice for optomechanics compared to ECDL lasers as they exhibit quantum-limited performance for high frequencies ($> 10\,\text{MHz}$) [145]. Excess phase noise acts as an effective thermal bath, limiting the achievable mode occupancy in cooling experiments [146]. Filter cavities can be used to later on improve the noise characteristics at lower frequencies [75, 147]. Furthermore, the broad frequency-tuning range of the TiSa allows to change the atomic decoherence rate over a large range.
A sketch of the partly planned, partly already realized system is shown in Figure 6.3. The TiSa is locked internally to a temperature-isolated reference cavity to increase the stability. Small frequency drifts of the laser change the lattice depth that the atoms experience, especially if the lattice is close to the resonance frequency [87]. This is the case for the calculated coupling parameters (see Figure 2.4). To allow an absolute frequency stability, the TiSa is furthermore locked to a transfer cavity[14] via PDH lock, visible at the top of Figure 6.3. The sidebands are created with a home-built EOM at $\approx 10\,\text{MHz}$.

The transfer cavity itself is locked, also via PDH, to the ^{87}Rb cooling laser (see Figure 3.4). Since the laser already has sidebands from the PDH lock to the atomic transition,

[13] Coherent MBR 110 pumped by a Coherent Verdi V18.
[14] Toptica FPI 100-0750-3V0

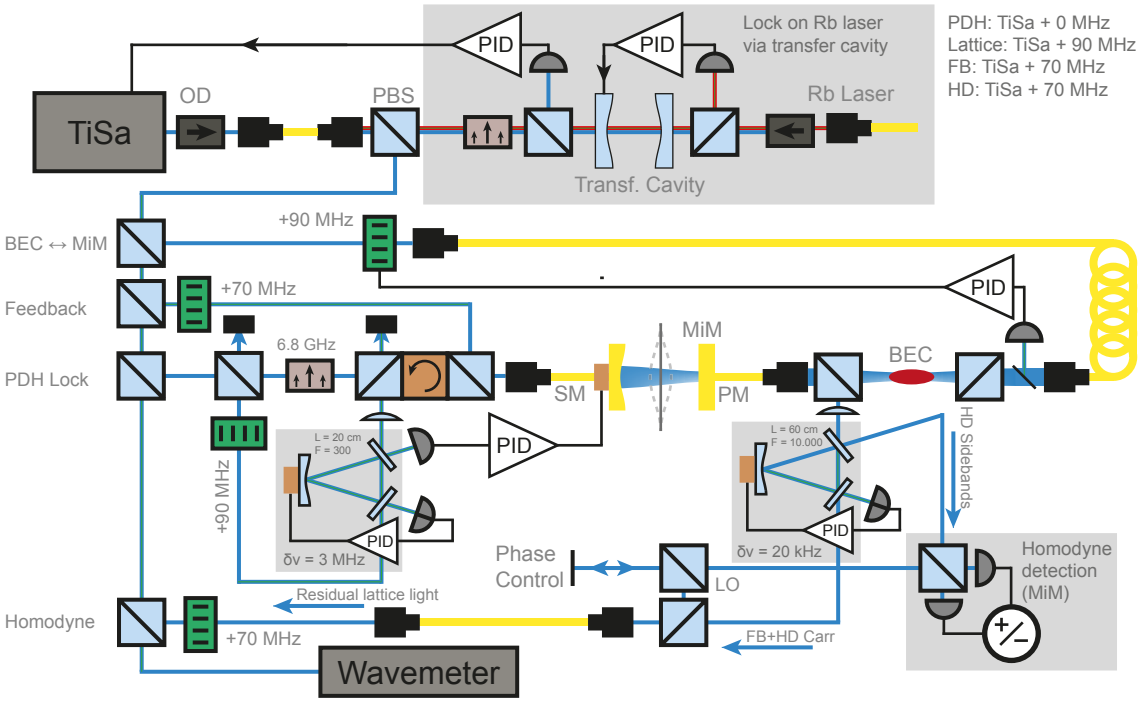

Figure 6.3: Sketch of the planned coupling laser system.

these sidebands are used to lock the transfer cavity to the laser. The TiSa can therefore be locked to the atomic resonance in units of the cavity-FSR. This also increases the short-term laser stability. Locking the laser to every FSR from -9 to $+6$ with respect to the cooling laser and measuring the beat signal of the two, a linear fit can be used to extract the FSR of the transfer cavity:

$$\Delta\nu = \#_{\mathrm{FSR}} \cdot (997.5437 \pm 0.0036)\,\mathrm{MHz}. \tag{6.1}$$

The error is the 50 % confidence interval of the fit. Knowing this, the TiSa laser frequency can be determined with sub-MHz accuracy using a wavemeter. A comparison of the transfer locked and unlocked TiSa is shown in Figure 6.4. Short term fluctuations as well as long term drifts of $\approx 50\,\mathrm{MHz}$ in two hours are present if the laser it not transfer-locked. Note that during this measurement, the laser was still locked to the internal reference cavity. The fitted short term fluctuation, measured as $f \approx 1\,\mathrm{Hz}$, are most likely the highly undersampled 90 kHz oscillations of the laser-internal etalon. The acquisition rate of the measurement was limited by the transfer time ($\approx 0.15\,\mathrm{s}$) from the spectrum analyzer to the data acquisition computer.
The transfer locked case shows a much improved stability, only a small sub-MHz drift is present. This is most likely caused by a drift in the DC offset of the lock. Sources can be an electronical drift or a polarization change in the EOM, leading to a change in residual amplitude modulation.

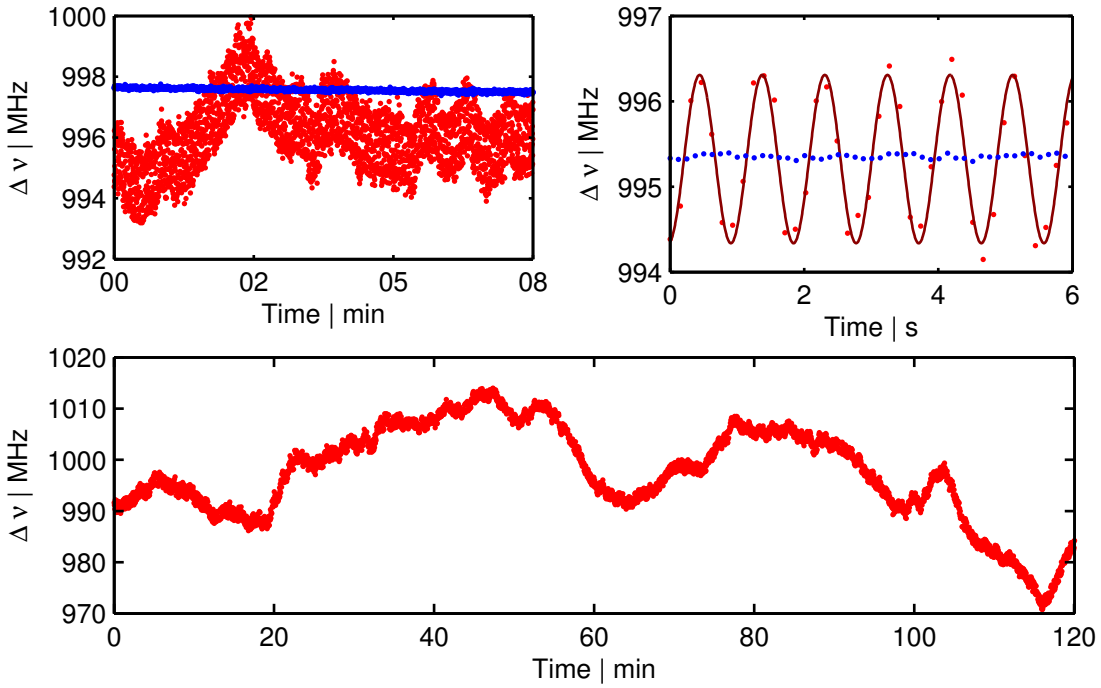

Figure 6.4: Top Left: Comparison of the locked TiSa (blue) to the unlocked TiSa (red). **Top Right:** Short term stability. **Bottom:** Long term drift of the unlocked laser.

The rest of the laser system, PDH lock of the MiM to the TiSa laser, homodyne detection, feedback cooling, and ring cavities to filter and overlap beams will be described in the upcoming thesis of Christina Staarmann.

6.3 First Optomechanical Signals

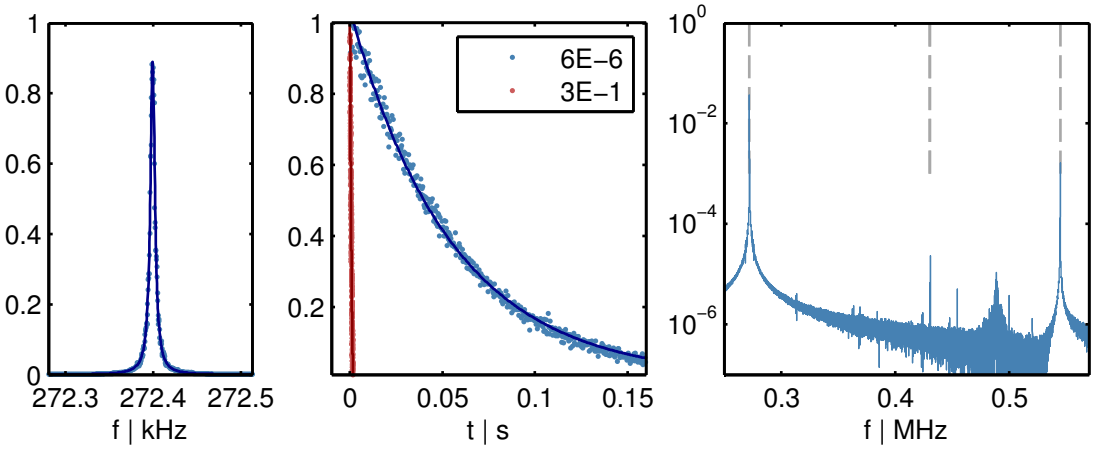

Figure 6.5: **Left:** Noise PSD of the cavity transmission signal, obtained with 60 averages at 1 Hz bandwidth. The pressure in the chamber is 1.6×10^{-6} mbar. The solid line is a fitted lorentzian peak. **Center:** Ring down measurements for two different pressure levels. The data points corresponds to the maxima of the ring down oscillations. Solid lines are a fitted exponential decay to determine the quality factor Q. **Right:** Single sided PSD obtained by fourier transforming the ringdown measurement at 6×10^{-6} mbar. The vertical lines correspond to the calculated higher mode frequencies according to Equation 6.3.

6.3.1 Mechanical Quality Factor

To validate the good mechanical properties of the Si_3N_4 membrane, the cavity was locked to a TiSa laser using a side-of-fringe lock. The bandwidth of the lock was limited by the used piezo amplifier[15], which has a no-load bandwidth of 32 kHz, well below the membrane frequency. The side of fringe lock is therefore not capable to regulate the high frequency membrane oscillations. Shown in Figure 6.5 is the observed noise power spectral density (PSD) of the transmission signal, obtained after averaging 60 traces with a 1 Hz bandwidth. The mechanical Q-factor is defined as [148]

$$Q = \frac{\omega}{\gamma} = \frac{f}{\Delta f_{\mathrm{FWHM}}}. \tag{6.2}$$

A fit to the power noise spectrum yields a $Q_{\mathrm{spec}} = 4.3 \times 10^4$.

As an alternative method, the ring down of the driven membrane can be measured to determine the mechanical Q-factor. Knowing the decay time τ and the frequency f, the mechanical Q-factor can be calculated as $Q = \pi \cdot f\tau$ [67]. Shown in Figure 6.5 on the right is the mechanical ringdown for two different pressures in the vacuum chamber. The mechanical Q increases as the pressure becomes lower. At $p < 1 \times 10^{-6}$ mbar, the background pressure is not the limiting factor any more [77]. The mechanical Q

[15] MadCity Labs PA25

extracted from the fit ob $Q_{\text{ring}} = 4.7 \times 10^4$ is consistent with the value obtained from the width of the PSD peak. The values obtained here are still below $Q \approx 2 \times 10^6$, the highest values reported in the literature [67]. It has to be noted that just one membrane was tested here and any small amount of contamination can cause a significant reduction of the mechanical Q.

6.3.2 Higher Membrane Modes

Beside the basic drum mode, the membrane can also oscillate with higher order modes. The frequencies of the (j,k)-mode of a thin square mechanical oscillator can be calculated according to thin plate theory as [67]

$$\omega_{j,k} = 2\pi\sqrt{\frac{\sigma\,(j^2+k^2)}{4\rho L^2}}, \tag{6.3}$$

where L is the lateral dimension, σ the tensile stress and ρ the density. Included in Figure 6.5 is the single-sided power spectrum of the above mentioned ringdown measurement. A peak at the driven (0,0) ground mode with a frequency of $\approx 272\,\text{kHz}$, and double the frequency, corresponding to the (1,1) mode is present. Furthermore a peak corresponding to the degenerate (0,1) and (1,0) is observed.
The broad peak slightly below 500 kHz is compatible with the expected resonance frequency of the scan piezo.

6.3.3 Membrane-induced Frequency Shift

In a second proof of principle experiment, the change of resonance frequency with respect to the membrane position was measured. A common technique is to scan the laser frequency over several FSR and simultaneously scan the membrane position [9, 37]. Due to the large FSR, this is not possible in the setup presented here. At length of $L = 25\,\mu\text{m}$, the free spectral range for a cavity is

$$\nu_{\text{FSR}} = \frac{c}{2L} \approx 6\,\text{THz}. \tag{6.4}$$

If the cavity is locked to a 780 nm laser, the next higher mode is approximately 12 nm away. It is necessary to scan the cavity length and simultaneously slowly scan the position of the membrane. The position of the cavity resonance with respect to the scan ramp of the cavity length gives an indication of the frequency shift caused by the membrane.

The calculated behavior, using the experimental parameters, is shown in Figure 6.6. It was obtained by solving the system of linear equations (similar to Section D.1 in the appendix) describing a free-space MiM system with length $L = L_1 + L_2$ [85]. For the case of good mode match, the fiber-based system should behave the same way. The position of the membrane x_{m} changes the length of the two coupled sub-cavities of the MiM according to $L_1 - x_{\text{m}}$ and $L_2 + x_{\text{m}}$. In Figure 6.6 on the left, only L_2, the outcoupling

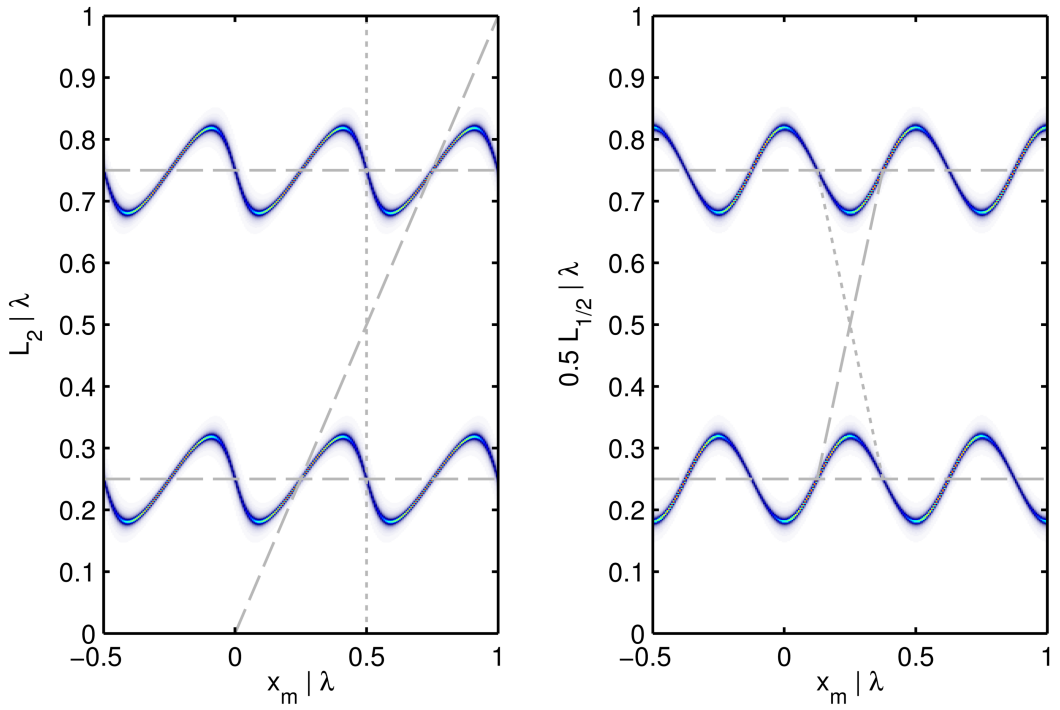

Figure 6.6: **Left:** Cavity length L_2 dependent on the position of the membrane x_m for $r_\mathrm{m} = 0.42$. L_2 corresponds to the length of the sub-cavity that is formed by the membrane and the outcoupling mirror. Visible are two ground modes, M_1 and M_2 (lower/upper). **Right:** As left but changing the length (L_1 and L_2) of the MiM system.

side, is varied as it was done in the experiment. An asymmetry of the ascending and descending slope is present in the signal. This asymmetry depends on the reflectivity of the membrane. For $r_\mathrm{m} = 0$, the signal is flat, whereas for $r_\mathrm{m} \to 1$, the signal approaches maximal asymmetry, converging towards the dashed diagonal and dotted vertical line shown in Figure 6.6.

The right side shows the case where L_1 and L_2 are both varied. This situation is similar to a frequency scan as the two fold symmetry of the higher modes is visible (see Figure 2.3). For this situation, as $r_\mathrm{m} \to 1$, the signal converges to the diagonal dashed and dotted lines in Figure 6.6 on the right.

The inherent asymmetry of the signal makes a position determination of the membrane in the MiM system according to [86] more difficult. For a frequency scan or simultaneous change of L_1 and L_2, the asymmetry is only caused by the off-center position of the membrane. It should nonetheless be possible to determine the position if the membrane if the reflectivity is known as an off center position should lead to an increased asymmetry. Note that a tilt of the membrane can also create an asymmetry [149].

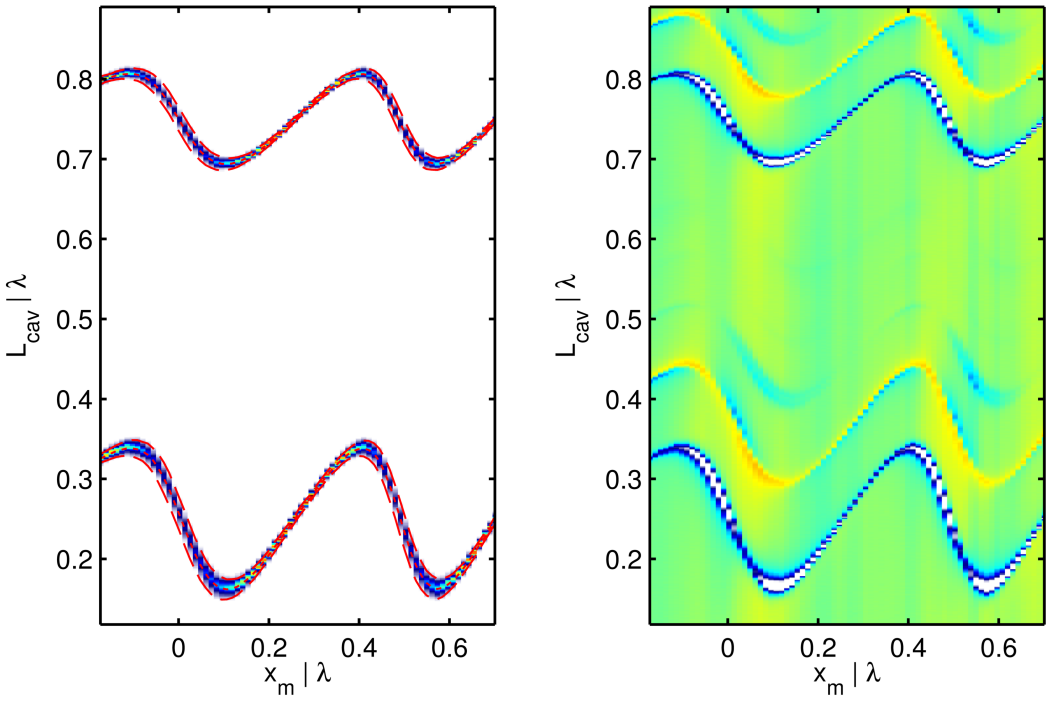

Figure 6.7: Left: Measured transmission signal of the asymmetric MiM system. The position of the M_1 and M_2 modes with respect to the length L_2 of the MiM cavity, dependent on the membrane position x_m is shown. The short/long dashed red lines indicate the fitted position/width of the resonance. **Right:** Corresponding reflection signal.

In the experiment, the cavity length was scanned using an HV-amp[16] at $\approx 70\,\mathrm{Hz}$ with a triangular linear ramp, the total length of the trace is 10 s. The result is shown in Figure 6.7. Each vertical line corresponds to one length scan of the cavity. Due to a hysteresis of the scan piezo, only the scans with the same sign of the scan slope are used. A clear shift of the resonance position with respect to the membrane position is observed.
The vertical axis is scaled to $\lambda/2$ between the two modes, the horizontal to the periodicity of the signal of $\lambda/2$. Comparing the signal to the theoretical prediction shown in Figure 6.6 yields a good agreement. The different amplitude of the M_1 and M_2 mode oscillations are caused by the nonlinearity of the scan piezo.
A lorentzian fit to both modes is used to extract the position, height and width of the resonances. The position and width has also been added to Figure 2.3.

6.3.4 Length Determination

Due to limited optical access, especially in a cryogenic implementation, it can be difficult to optically determine the length of the cavity in fiber-based MiM systems. The position of the higher order transversal modes, visible in the reflection signal, is a function of the cavity length for a fixed r_2 (see Equation 5.15). This is shown in Figure 6.8. The

[16] A. A. Lab Systems A-301HS, gain of 20

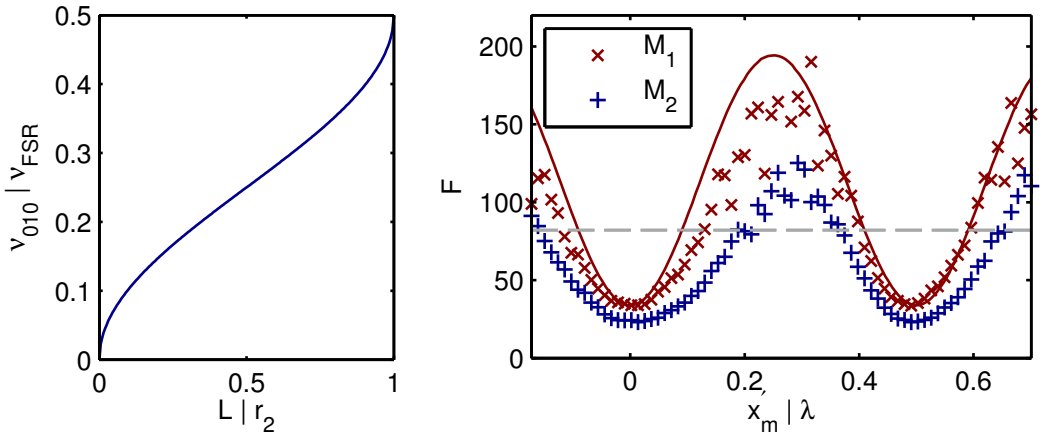

Figure 6.8: Left: Frequency of the first higher-order transversal mode with respect to the FSR in a PC cavity as a function of the length L. **Right:** Finesse of the M_1 and M_2 mode dependent on the membrane position. The difference between the two can be attributed to a nonlinearity of the scan piezo. The solid line is the finesse extracted from Figure 6.6.

corresponding length L of the measurement shown in Figure 6.7 with $\nu_{010} \approx 0.25 \cdot \nu_{\mathrm{FSR}}$ is $L \approx 0.4 \cdot r_2 \approx 25\,\mu\mathrm{m}$.

6.3.5 Finesse

The finesse in an asymmetric cavity depends on the membrane position. The ascending and descending slope, as shown in Figure 6.7, correspond to the light predominantly stored in the two different sub-cavities [37]. The finesse is calculated as the width of the fitted transmission peak divided by the distance of the two modes (see Figure 6.7) and is shown in Figure 6.8. The corresponding theoretical model is calculated from the signal shown in Figure 6.6. At $x_{\mathrm{m}} = 0$, the light is stored in the planar-planar sub-cavity formed by the low reflecting incoupling mirror and the membrane, resulting in a low finesse. For the experimentally more interesting point, the position of the membrane resulting in a higher finesse, the light is predominantly stored in the sub-cavity at the outcoupling side. The signal agrees well with the theoretical model. The deviation for the M_2 mode are to be attributed to the nonlinearity of the scan piezo.

6.3.6 Reflectivity and Transitivity

Like the finesse, the transmission and reflection signals of an asymmetric MiM system also depend on the membrane position. The experimental data is shown in Figure 6.9 and demonstrates the finite reflectivity on resonance, alongside the position dependence. A distinct difference between a free space realization of an asymmetric MiM [77] is present in the reflection signal σ_{ref}. It should look similar to $1 - \sigma_{\mathrm{trans}}$ but a strong deviation of σ_{ref} at the minima of σ_{trans} is observed. This is most likely resulting from a change of the spatial mode in the cavity, which is caused by a misaligned membrane [149]. The interference effect results in light loss of the reflected light in the incoupling fiber. The

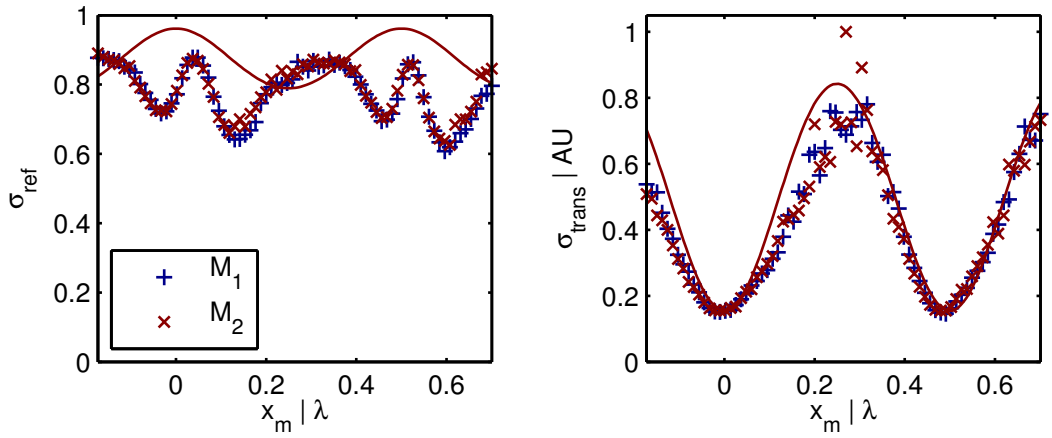

Figure 6.9: Left: Measured reflectivity on resonance for the two modes. The solid line is the value extracted from Figure 6.6. **Right:** Transitivity on resonance for the two modes. The solid line is the value extracted from Figure 6.6.

deviation is strongest at the membrane position where the light is predominantly stored in the planar-planar sub-cavity at the incoupling side (see Figure 6.8). Such a cavity is critically affected by the membrane angle, which is not optimized here.

6.4 Conclusion

The measurements presented in this section prove that is possible to realize an asymmetric fiber-based MiM with finite reflectivity on resonance. In the next step, the fiber-based MiM system can be used as part of the long-distance coupled hybrid quantum system. Later in the experiment both fibers are mounted in self designed five-axis goniometer [82], which enable nanometer position and sub-degree angular resolution alongside realignment possibility in cryogenic UHV situations. Then, the effect of the membrane tilt can be analyzed and the source of the deviation in Figure 6.9 can be studied.

It seems unlikely that it is possible to realize a cryogenic asymmetric fiber cavity by alignment and subsequent glueing at room temperature. The cool down will most likely destroy the alignment and therefore induce massive losses in the system.

Chapter 7

Future Perspectives

With the two constituents of the hybrid quantum system experimentally realized, both systems can be brought together and coupled to observe ground state cooling and coherent interaction of the cryogenic MiM system and the sample of ultracold atoms. This will, hopefully, already allow to cool the mechanical oscillator down to its motional ground state and therefore expand the experiments in room temperature presented in [46]. A far detuned 2D optical lattice reduces losses by light-induced collisions [50] and an optical dipole trap for coupling to internal states [41] are already set up and ready to be installed (see the bachelors thesis of Benjamin Abeln [150]). Afterwards, internal coupling schemes, sketched in Section 2.4, will be studied. For these experiments, it might be very beneficial use a BEC due to the high optical density.

The large FSR of a short fiber cavity could be used to do optomechanical experiments on the D_1 and D_2 line of ^{87}Rb simultaneously. A cavity with a length $L \approx 21\,\mu\text{m}$ can be resonant with the D_1 line while the D_2 line is exactly one FSR away. Placing the membrane at the slope close to the center of the cavity would realize a different sign for the interaction with the two atomic transitions with near identical interaction strengths. This maybe useful to mediate a coupling between the two atomic states.

As future perspectives, a few ideas for this setup come to mind. The coupling schemes sketched in Section 2.3 and 2.4 require the cavity to operate in the bad cavity limit ($\delta\nu_{\text{cav}} > f_{\text{m}}$). For this case, the reflected field of the cavity adiabatically follows the position of the membrane and the mediating light field can be eliminated. However, from a pure optomechanical point of view, resolved sideband systems have been more successful to cool mechanical oscillators [5, 6]. The use of a resolved sideband MiM system may lead to interesting effects for the hybrid quantum system. For this case, the adiabatic elimination of the light field [40, 41] is not possible any more and retardation effects become important.
This poses new challenges, as fiber-based MiM systems are difficult to bring into the resolved sideband regime due to their short length. Nevertheless, using a large mode area (LMA) incoupling fiber and a high finesse, it should be possible. The larger waist results in a smaller divergence and allows a longer cavity. In a PC geometry with stable

mode match, a length of $L = 450\,\mu\text{m}$ with $r_2 \approx 900\,\mu\text{m}$ is possible[1]. The benefit of the PC geometry is that no processing of the LMA is necessary, which may be difficult especially for a large r_2 (see PM fiber processing in [121]). A line width of $\delta\nu_{\text{cav}} \approx 4\,\text{MHz}$ is feasible, using a finesse of $\mathcal{F} = 80000$. Note that although not realized yet, the surface quality of processed fiber ends is good enough to allow such a high finesse [47]. In comparison, the highest reported finesse to date is $\mathcal{F} = 37000$ [47].

Using ultra-low mass nanomechanical oscillators with $m \lesssim 1 \times 10^{-21}\,\text{kg}$ and high frequency such as carbon nanotubes [151, 152], it may be possible to bring the system into the regime of nonlinear optomechanics. Note that it is feasible to use sub-wavelength oscillators in a MiM system [61]. In such a system it would be possible to observe the granularity of the photon stream [153], study a gradual transition from the quantum to the classical world [154], or an optomechanically-induced photon blockade [155] (see [83] for a review). In such a system, the BEC could be used to store [53] and detect quantum information [95].

In addition to the long-distance coupled hybrid quantum system discussed in this thesis, the cryostat is also UHV capable to house a hybrid quantum system based on short-range interaction. In such a setup, a MOT would be created outside of the cryostat and magnetically transported [35, 156] into a superconducting two-bar Ioffe trap [157] to create a BEC close to the mixing chamber. All magnetic coils for the horizontal and vertical transport and the Ioffe trap are already designed and the system will be modified after the external coupling experiments are concluded. In this type of system a large amount of interesting proposals like the measurement of the membrane position using the spin of a BEC [158], probing the quantum coherence of an oscillator with a BEC [159], using the atoms to probe the Wigner distribution of an oscillator [160], the controlled creation of ripples on a graphene sheet [161], the use of lattice-trapped atoms for quantum information processing [162], or the creation of a phonon laser by coupling a BEC to a magnetic oscillator [163] are presented in the literature. All these proposals are based on short range interactions and allow for further interesting research perspectives on this project.

[1] Using a LMA-25 fiber from NKT photonics ($w_{\text{f}} = 10.3\,\mu\text{m}$). Such large r_2 are already reported in the literature [117].

Appendix A

Membrane Properties

A.1 Thermal Conductivity

To get an idea of the expected membrane temperatures, which are closely connected to the thermal conductivity, Figure A.1 gives an overview of different papers stating thermal conductivity for SiN. Reference [164] states a range of

$$\kappa(T) = 0.01 \cdot T^2\,\mathrm{W\,m^{-1}\,K^{-1}} \qquad \text{to} \qquad \kappa(T) = 0.2 \cdot T^2\,\mathrm{W\,m^{-1}\,K^{-1}} \tag{A.1}$$

for all amorphous solids, of which SiN is one. Comparing this range to the thermal conductivity used in [40] reveals the value is most likely too optimistic compared to available literature. However, it has to be noted that to our best knowledge, no measurement of a membrane made from stoichiometric Si_3N_4 exist at cryogenic temperatures.

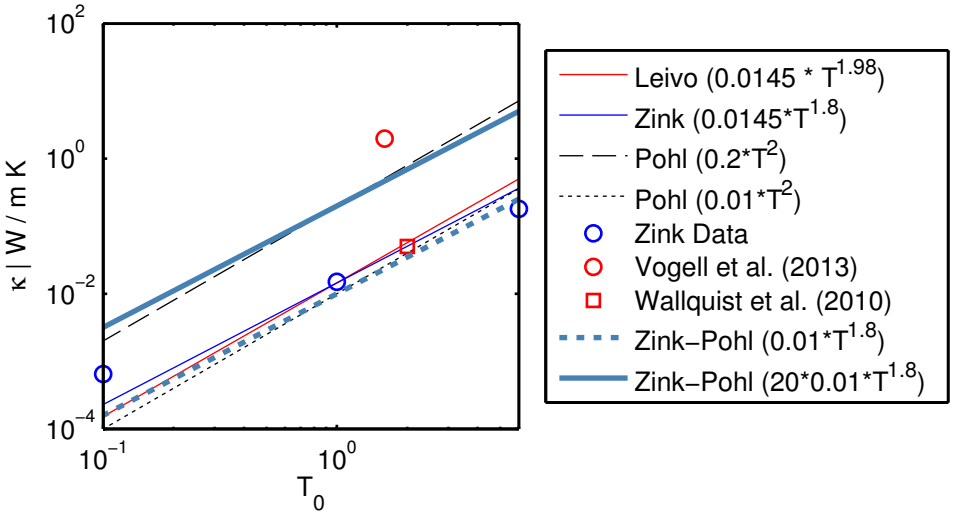

Figure A.1: Left: Overview of the thermal conductivity for silicon or silicon nitride reported and used in the literature. Leivo [165], Zink [166], Pohl [164], Zink-Pohl is the Pohl intercept with Zink scaling, Vogell et al [40], Wallquist et al [167].

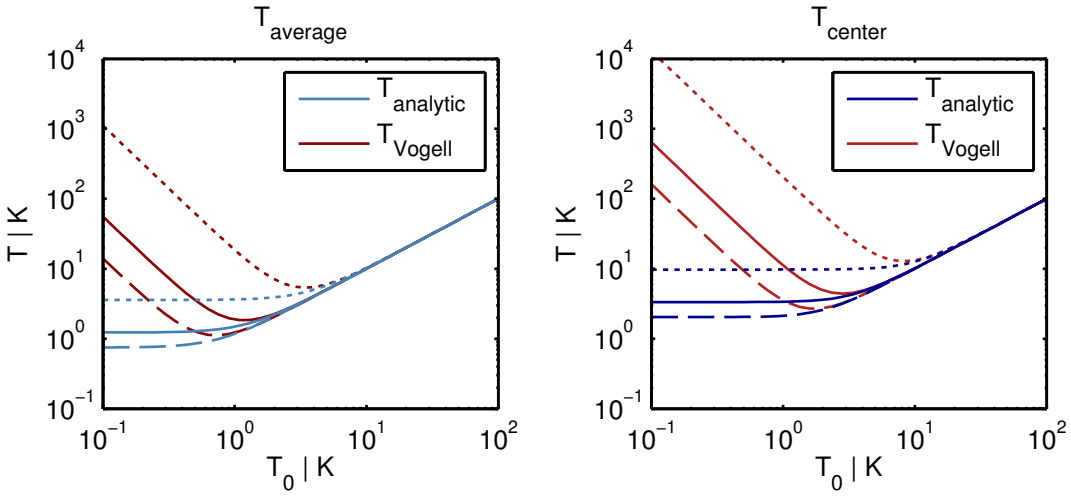

Figure A.2: Left: Average temperature of the membrane, modeled as a thin disk. The solid (dotted) lines correspond to $\kappa(T) = 0.01 \cdot T^{1.8}$ ($\kappa(T) = 0.2 \cdot T^{1.8}$) $\mathrm{W\,m^{-1}\,K^{-1}}$, the dashed line corresponds to the value used in [40]. See also Figure A.1. **Right:** As left, shown here is the center temperature.

A.2 Membrane Temperature

To obtain a more realistic estimation of the membrane temperature, we solve the heat equation for a temperature dependent $\kappa(T)$. As shown in Figure A.1, it is commonly modeled as:

$$\kappa(T(r)) = \kappa_\mathrm{i} T(r)^{\kappa_\mathrm{s}}. \tag{A.2}$$

The heat transport equation in cylinder coordinates is [168]

$$\frac{1}{r}\frac{\partial}{\partial r}\left(r \cdot \kappa(T(r))\frac{\partial}{\partial r}T(r)\right) = -Q(r) \tag{A.3}$$

with the source term $Q(r)$. The source

$$Q(r) = \frac{4\mathcal{F}}{\pi} \cdot \frac{P_0 \mathfrak{a}^2}{d} \cdot \frac{2}{\pi w^2} e^{-\frac{r^2}{w^2}} \tag{A.4}$$

is modeled as a normalized gaussian beam. It is scaled with the circulating power for a maximally asymmetric cavity (see Equation D.9) and multiplied by the absorbed power with input power P_0 and power absorption $\mathfrak{a}^2$, similar to [40]. The solution of this equation gives the temperature profile

$$T(r) = \left(\frac{\mathfrak{a}^2 \mathcal{F} P_0 \left(\mathrm{Ei}\left(-\frac{2r^2}{w^2}\right) - \mathrm{Ei}\left(-\frac{2R^2}{w^2}\right) - 2\left(\log\left(\frac{r}{R}\right)\right)\right)}{\kappa_\mathrm{i} d} \ldots \right. \tag{A.5}$$

$$\left. \ldots + \pi^2 \left((\kappa_\mathrm{s}+1)^{-\frac{1}{\kappa_\mathrm{s}+1}} T_0\right)^{\kappa_\mathrm{s}+1}\right)^{\frac{1}{\kappa_\mathrm{s}+1}} \pi^{-\frac{2}{\kappa_\mathrm{s}+1}} (\kappa_\mathrm{s}+1)^{\frac{1}{\kappa_\mathrm{s}+1}}. \tag{A.6}$$

The solution depends on the exponential integral function defined as:

$$\mathrm{Ei}(x) = -\int_{-x}^{\infty} \frac{e^{-t}}{t} \mathrm{d}t. \tag{A.7}$$

The two integration constants are chosen to fix the boundary temperature to the base temperature T_0

$$T(R/2) = T_0 \tag{A.8}$$

and to remove the pole at $r = 0$ present in the exponential integral function and the logarithm:

$$\left.\frac{\partial T(r)}{\partial r}\right|_{r=0} = 0. \tag{A.9}$$

The comparison of the complete solution and the approximation used in [40] is shown in Figure A.2. Only the complete solution shows a meaningful behavior at low base temperatures. The minimum and subsequent increase of both the center and average temperature with decreasing base temperature is a result of the fixed thermal conductivity. This leads to a shielding effect, preventing the energy to be transported through the membrane to the frame. The complete model shows a saturation of the center and average power as the base temperature decreases. This saturation value depends on $\kappa(T)$.

A.3 Membrane Reflectivity

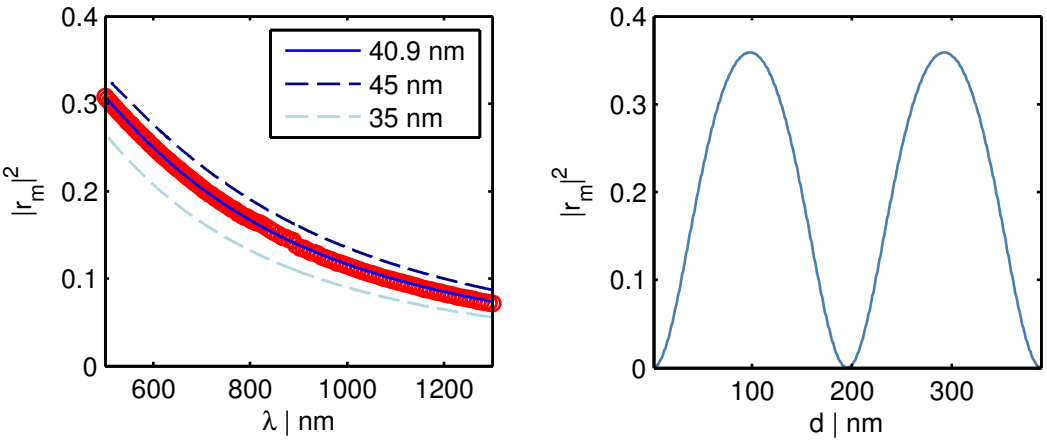

Figure A.3: Left: Power reflectivity of a 1.5 mm x 1.5 mm x 50 nm Si_3N_4 membrane from Norcada in red, calculated from the measured power transmission. Only every 15th data point is shown. The solid blue line is a fit to the data for an etalon with wavelength dependent refractive index. **Right:** Calculated reflection dependent on the membrane thickness.

One important property to know is the thickness of the membrane and the resulting reflectivity as the frequency shift of the cavity depends on it (see Equation 2.7). To characterize the membrane, we measured the transmission of a 1.5 mm x 1.5 mm x 50 nm

Si_3N_4 membrane from Norcada from 500 nm to 1300 nm using a spectrophotometer[1]. The result is shown in Figure A.3. The membrane can be model as Fabry-Pérot etalon (see Equation 5.9) with reflectivity

$$r_i = \frac{n_1 - n_2}{n_1 + n_2}, \tag{A.10}$$

where n_1 and n_2 are the refractive indices of air and Si_3N_4. The wavelength-dependent refractive index as given in [169] by the Sellmeier equation

$$n^2_{Si_3N_4} - 1 = \frac{2.8960\lambda^2}{\lambda^2 - 140.102} \tag{A.11}$$

was used. A fit yields a thickness of 40.9 nm, consistent with the values given in [19, 46] and slightly below the specification of 50 nm $\pm$7%. The measured thickness corresponds to a field reflectivity of $|r_m| = 0.416$ at 780 nm.

[1] Agilent Cary 5000 UV-Vis-NIR

Appendix B

BEC System

B.1 Glass Cell FEM Analysis

To ensure that the air pressure does not bend the walls of the glass cell to much and therefore does not negatively affect the imaging performance, a finite element calculation was performed. For a thickness of 3 mm, the maximal deviation and therefore also the curvature is small enough to not negativly affect the detection performance.

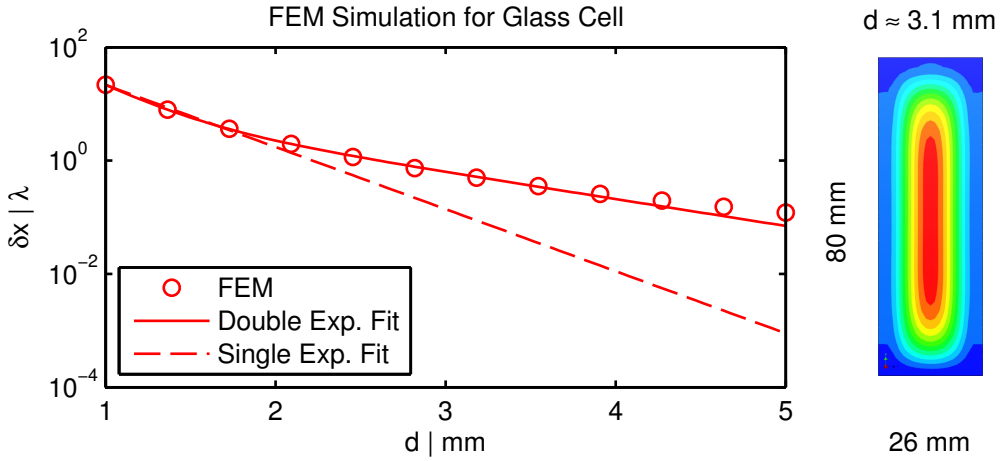

Figure B.1: FEM results of the maximal displacement perpendicular to the surface.

B.2 Trap Switching

The atoms are commonly detected via time of flight measurements [96]. It maps the in-trap momentum distribution to a spatial distribution, which can be detected with a CCD camera. Any uncontrolled momentum kick, caused by field gradients from the trap switch-off, can disturb the momentum distribution. Additionally a kick along the detection axis can move the atoms out of focus leading to an unsharp image. It is therefore important to quickly switch the magnetic trap off with minimal disturbance of the atoms.

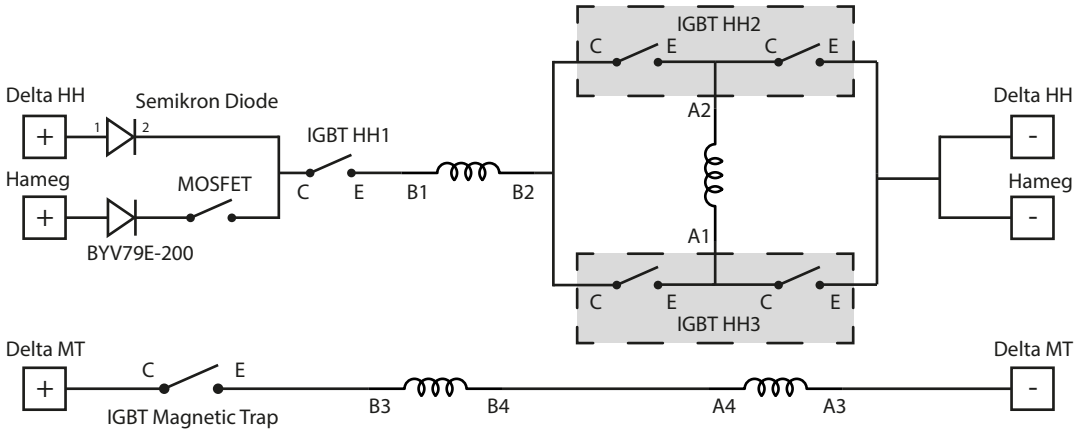

Figure B.2: Sketch of the used configuration to switch the HH coils and magnetic trap.

This is realized with several dual insulated-gate bipolar transistors (IGBT), which are capable of handling the high currents driving the coils. In use at this experiment are dual IGBTs[1], which consist each of two IGBTs where the emitter and collector are connected internally. This enables the realization of an H-bridge with two dual IGBTs. They are protected from high voltages with a varistor[2], which is connected in parallel to collector and emitter. A sketch of the connections is shown in Figure B.2. To enable the use of the HH coils in HH and anti-HH configuration, one of the coils is mounted in the H-bridge. A third IGBT, IGBT 3, is connected in series of the second coil and the H-bridge, acting as an additional switch. The measured switch off times are shown in Figure B.3. Shown is the voltage measured over the varistor with a high-voltage probe[3]. Switching only IGBT 3 has proven to be not sufficient to switch-off the anti-HH coils efficiently (see Figure B.3). The switch off time using only IGBT 3 is considerably longer than switching with the IGBT and the H-bridge simultaneously, probably due to reduced induction in the coils.

B.3 Watercooling

The HH coils and the magnetic trap have to be water cooled to avoid overheating. We use a commercial water/water chiller[4] to cool the magnetic trap, the HH coils and also the IGBTs. To avoid any damage to the coils in case of a water leaks or pump failure an interlock system is installed, which switches off the power supplies and/or the pump depending of the specific failure. In addition to the error-out electrical contact of the

[1] Mitsubishi 200A/1200V Dual IGBT (CM200DX-24S) in combination with VLA536-01R driver boards. These boards are soldered directly onto the IGBT. This technique proved to be much better than designing the drivers ourselves and soldering the driver ICs by hand. In contrast to other experiments all of the driver boards worked without a hassle.

[2] EPCOS B40K320

[3] Hameg HZ115

[4] Van der Heijden - 210-B400 SON WA-WA. The chiller has a cooling power of 3.2 kW @ $\Delta T = 3°$ and a flow of 800 L h^{-1} @ 5.3 bar. A 100 L tank enables a slow response of the cooling cycle. The pressure can be controlled by manually opening and closing an internal bypass.

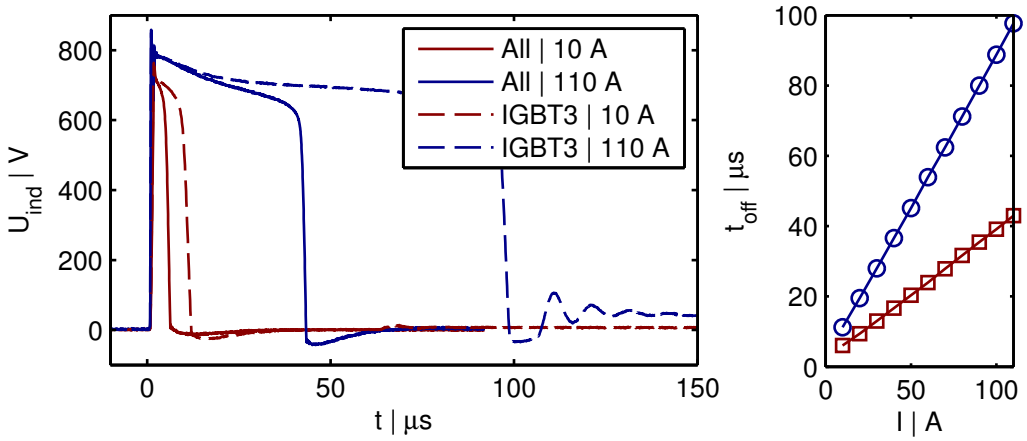

Figure B.3: Left: Switch-off time in anti-HH configuration of the MOT coils for two currents. The dashed line indicate just switching off IGBT 3 whereas leaving the H-bridge open. **Right:** Measured switch-off times. The blue line indicates switching only IGBT 3, red indicates a switch-off using all IGBTs.

water/water chiller, flow guards, as listed in Table B.1, are installed before and after the magnetic trap and HH coils. Temperature sensors on the IGBT boards are also included in the interlock system. The error conditions are listed in Table B.2. Both power supplies for the magnetic trap and the HH coils have interlock inputs which are connected to the interlock system. For the water/water chiller we use the remote start function to switch off the pump in case of a leak detected by the flow guards.

Flow guard	max flow
FW 1.0	15 l
FW 1.1-1.4	3.5 l
FW IGBT	5 l

Table B.1: Flow guards used in the interlock system. They open a contact if the flow value drops below a value set at the guard.

Error	Pump	Trap
Flow guard	x	x
Airpax		x
Spill guard	x	x
Chiller	x	x
X1,X2,X4	x	x
X3		x

Table B.2: Effect of an error in one of the interlock parts. A "x" denotes that the part is switched off. The X1 to X4 connections are additional ports which can be used later on if necessary.

B.4 Magnetic Trap

For reference, the resistance and inductivity of the HH coils and the magnetic trap for both sides (A and B) were measured.

	L | µH	R | mΩ
A HH @ 20 Hz	625.7/609.1	0.136/0.133
A MT	124.5/124.8	0.083/0.081
B HH	625.8/611.9	0.136/0.134
B MT	124.7/124.9	0.084/0.082
A HH @ 1 kHz	614.8/607.6	0.214/0.182
A MT	124.5/125.5	0.098/0.099
B HH	614.8/608.9	0.224/0.190
B MT	124.7/124.2	0.098/0.099
A HH @ 100 kHz	538.0/628.7	11.5/86.99
A MT	97.2/98.4	3.87/4.81
B HH	534.4/611.0	11.56/86.47
B MT	97.6/98.6	3.81/4.74

Table B.3: Measured inductivity L and resistance R of the two magnetic trap (MT) and Helmholtz (HH) coils (side A and B). The left value is the coils without water, the right was taken once the coil was filled with water. All values were measured with a Hameg HM8118 LCR bridge.

Appendix C

Fiber Processing

C.1 CO_2 Laser

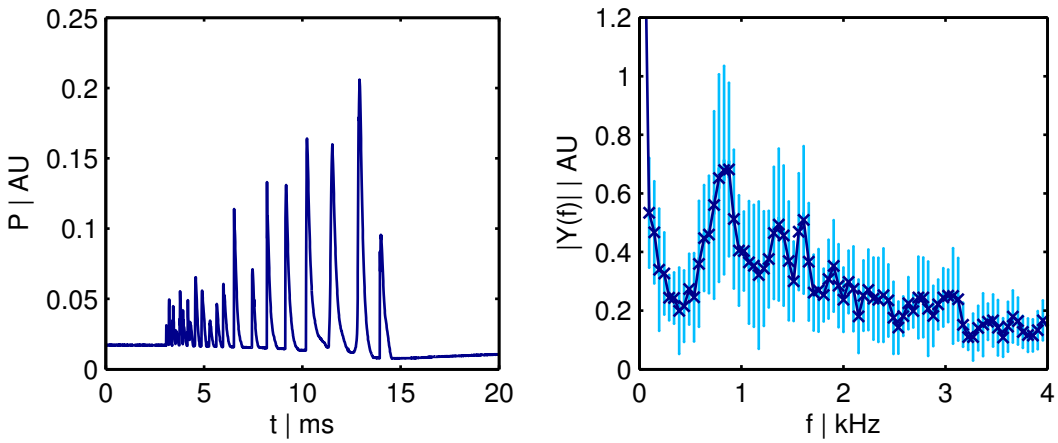

Figure C.1: **Left**: Exemplary trace of the CO_2 laser output. **Right:** Absolute square of the mean single sided power spectrum obtained by a FFT transformation of ten traces. The error bars indicate the standard deviation.

The output of the CO_2 laser is intrinsically pulsed as can be seen in Figure C.1. The fast fourier transform, shown in Figure C.1 on the right, has a peak at $f \approx 0.8\,\text{kHz}$, significantly lower than the 20 kHz reported in [117] for a Synrad Firestar v20. The data was acquired with a photovoltaic multiple junction detector[1].
As a result, the number of pulses for a given pulse length is much lower and therefore pulse fluctuations become more critical. This is consistent with the observation that sometimes two processing pulses are necessary to get the desired depth and radius of curvature.

[1] VIGO PVM-10.6-1x1-BNC-ZnSeAR

C.2 Interferometer Analysis

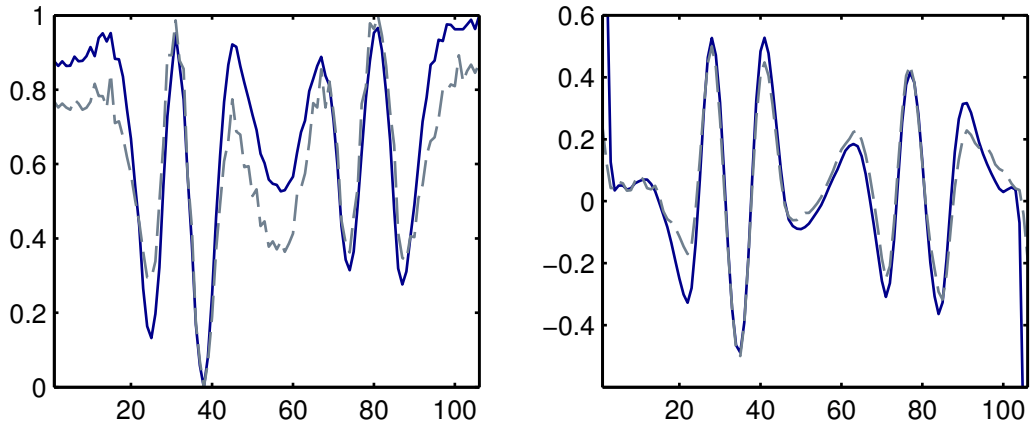

Figure C.2: Left: Exemplary cuts of the right side of expression 4.8 in blue and with dropped second term in dashed gray. **Right:** Derivative of the traces shown on the left image without substrate image (equation 4.10) in blue and for the complete expression with substate image (Equation 4.9) in dashed gray.

To evaluate the importance of the reference image, we took exemplary fiber images with and without the substate image. This difference is shown in Figure C.2. For the raw expression according to Equation 4.8, a strong deviation is visible. Once the derivative is applied, as shown on the right side, the effect of the substrate image becomes negligible due to the slow oscillation compared to the interference image as discussed in Section 4.3.1.

C.3 Interferometer Alignment

A detailed discussion of the alignment procedure is already presented in the thesis of Philipp Christoph [121] and will not be repeated here. However as it became evident later on how important it is to determine the radius of curvature with high accuracy, some further optimization is presented here.

Figure C.3 shows three different situations: The first row is a well aligned interferometer signal. If the parabolic mirror is properly aligned it can be assumed that the processed feature is symmetric in it self (see Section 4.4). Therefore the interference signal also has to be symmetric. Any asymmetry degrades the radius of curvature fit and especially makes the determination of the center very difficult. The well aligned interferometer images in the first row are very symmetric and therefore usable.

Misalignment of the interferometer can substantially deform the interference signal of the fiber as can be seen in row two and three of Figure C.3. The first row shows an image where the resonant cavity LED is slightly misaligned horizontally, e.g. by tilting the mirror mount the RCLED is mounted in. For such a misalignment, the overall phase

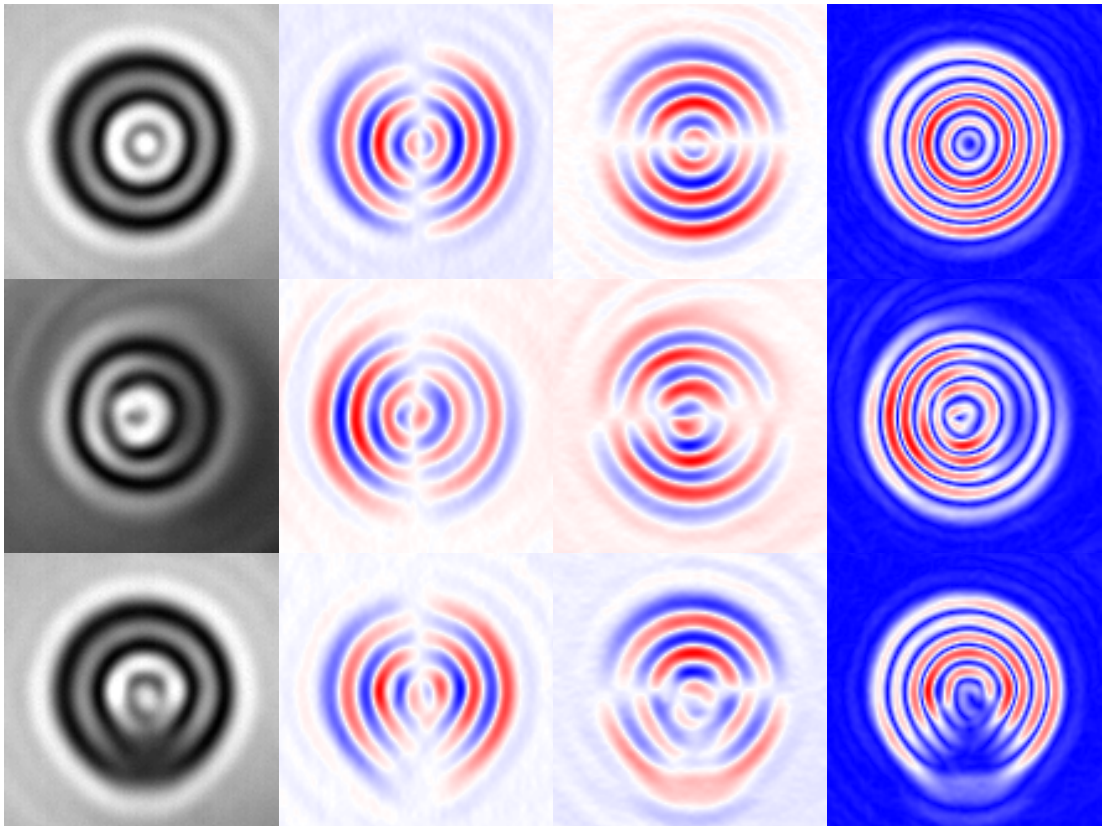

Figure C.3: Top to bottom: Well aligned interferometer, offset RCLED, clipping of the interferometer. **Left to right:** Raw image, I^x_{fit}, I^y_{fit} and $|I_{\text{fit}}|$. Each image width is 33 µm and is normalized.

on the fiber is still constant but a strong horizontal deformation of the background corrected image is visible.

The last row in Figure C.3 shows the effect if the silver mirror interfacing the interferometer and processing setup clips part of the beam. Whereas the horizontal cut through the image may be usable almost all information in the lower part of the image is lost.

Appendix D

Asymmetric Cavity

D.1 Intracavitity Fields

Alternatively to the sum of the fields propagating in a cavity as done in Equation 5.6 and 5.9, the transmission and reflection signal of a cavity can also be calculated by solving a system of linear equations [85, 86, 170]:

$$\begin{pmatrix} -1 & -e^{i\phi}r_1 & 0 & 0 \\ -e^{i\phi}r_2 & -1 & 0 & 0 \\ 0 & e^{i\phi}t_1 & -1 & 0 \\ e^{i\phi}t_2 & 0 & 0 & -1 \end{pmatrix} \cdot \begin{pmatrix} E_1 \\ E_2 \\ E_{\text{ref}} \\ E_{\text{trans}} \end{pmatrix} = \begin{pmatrix} -t_1 E_{\text{in}} \\ 0 \\ -r_1 E_{\text{in}} \\ 0 \end{pmatrix}. \tag{D.1}$$

The different fields are sketched in Figure D.1 and are connected by the reflectivities r and transmitivities t of the mirrors.

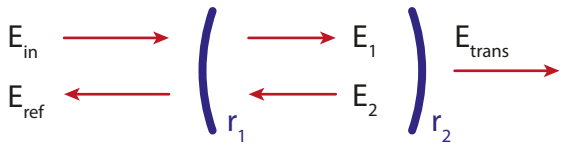

Figure D.1: Fields as used in Equation D.1.

The solution of this system of linear equations is

$$\left\{ \frac{E_{\text{in}} t_1}{1 - e^{2i\phi} r_1 r_2}, \frac{E_{\text{in}} e^{i\phi} r_2 t_1}{-1 + e^{2i\phi} r_1 r_2}, E_{\text{in}} \left(r_1 + \frac{e^{2i\phi} r_2 t_1^2}{-1 + e^{2i\phi} r_1 r_2} \right), \frac{E_{\text{in}} e^{i\phi} t_1 t_2}{1 - e^{2i\phi} r_1 r_2} \right\} \tag{D.2}$$

and is consistent for the reflected and transmitted field with the expression given in Equation 5.6 and 5.9 but also contains solutions for the intra cavity field used to calculate the circulating power in Section D.2.

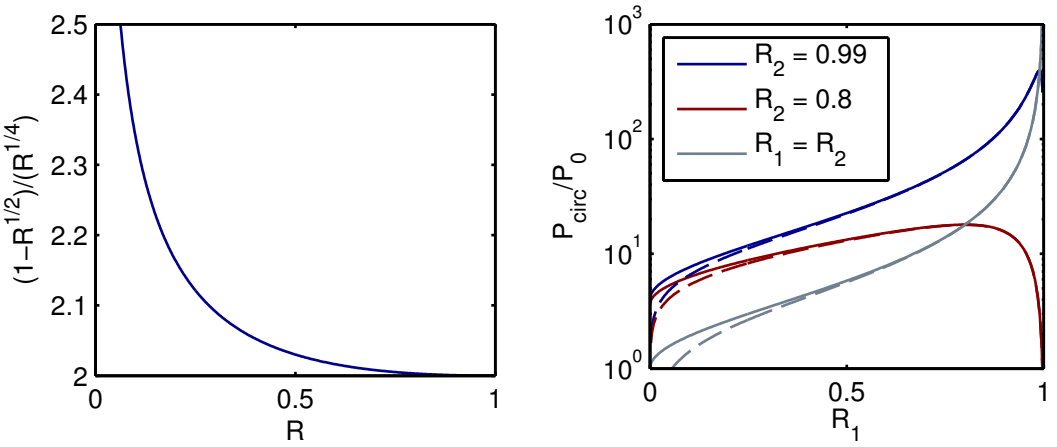

Figure D.2: Left: Validity of the taylor series $\left(1+\sqrt{R_2}\right)/\sqrt[4]{R_2} \approx 2+\mathcal{O}(2)$ around $R = 1$. **Right:** Circulating cavity power shown for different values of R_2. The solid line is the corresponding complete expression according to D.5. The dashed lines correspond to the taylor approximated solution given in Equation D.9. The gray line indicates the circulating power for the symmetric case of $R_1 = R_2$.

D.2 Intracavity Power

The intracavity power is the important parameter when thinking about the coupling of a membrane inside the cavity to the light field. The circulating power P_{circ}

$$\frac{P_{\mathrm{circ}}}{P_0} = \left|\frac{E_1 - E_2}{2}\right|^2 \tag{D.3}$$

in a cavity can be calculated as the mean of the right and left propagating fields, E_1 and E_2, as defined in the Section D.1. Inserting the expressions for the fields E, Equation D.3 can be written as

$$\frac{P_{\mathrm{circ}}}{P_0} = -\frac{1}{4}\frac{(R_1-1)(1+\sqrt{R_2})^2}{(1-\sqrt{R_1R_2})^2} \tag{D.4}$$

$$= -\frac{\mathcal{F}}{4\pi}\cdot\frac{(R_1-1)(1+\sqrt{R_2})}{(1-\sqrt{R_1R_2})\sqrt[4]{R_1}}\cdot\frac{1+\sqrt{R_2}}{\sqrt[4]{R_2}}. \tag{D.5}$$

Here, $\mathcal{F}$ is the Finesse as defined in Equation 5.13. The last factor can be taylor expanded around $R = 1$ to first order

$$\left.\frac{1+\sqrt{R_2}}{\sqrt[4]{R_2}}\right|_{R_2=1} \approx 2+\mathcal{O}(2), \tag{D.6}$$

leading to an approximated relation for the circulating power

$$\frac{P_{\mathrm{circ}}}{P_0} \approx -\frac{\mathcal{F}}{2\pi}\cdot\frac{(R_1-1)(1+\sqrt{R_2})}{(1-\sqrt{R_1R_2})\sqrt[4]{R_1}}. \tag{D.7}$$

The taylor series in Equation D.6 is shown in Figure D.2 on the left side. Note that the first order of the taylor series is zero, therefore the approximation is valid over a broad range.
Using the taylor expansion two more times, Equation D.7 can be simplified further, and ultimately be expressed in terms of the field reflectivity on resonance $\bar{\rho}$ as

$$\frac{P_{\text{circ}}}{P_0} \approx \frac{\mathcal{F}}{\pi}\left[1 - \frac{(\sqrt{R_1} - \sqrt{R_2})}{(1 - \sqrt{R_1 R_2})}\right] \tag{D.8}$$

$$= \frac{2\mathcal{F}}{\pi}\left(\frac{1-\bar{\rho}}{2}\right). \tag{D.9}$$

This approximated expression is compared with the full expression of Equation D.5 in Figure D.2 on the right side for two different values of R_2. Both expressions agree very well if R_1 is larger than 0.5. Therefore, Equation D.9 is a very useful expression to calculate the circulating power of an asymmetric cavity on resonance. It is consistent with the expression used in [40], which corresponds to the limit of a maximally asymmetric cavity ($\bar{\rho} = -1$).

Looking at Equation D.9, it is easy to see that, for an asymmetric cavity, the circulating power depends on the incoupling side. The amplification inside the cavity scales with the finesse, which is independent of the incoupling side, but there is a distinct difference for the circulating power P_{circ}. If the incoupling mirror is the less reflective one ($\bar{\rho} < 0$) more light enters the cavity and is amplified. If the incoupling mirror is the higher reflective one ($\bar{\rho} > 0$), more light is promptly reflected, subsequently less enters the cavity and the circulating power is smaller.

For the special case of a symmetric cavity ($\bar{\rho} = 0$), the circulating power $P_{\text{circ}}^{\text{sym}}$ is

$$\frac{P_{\text{circ}}^{\text{sym}}}{P_0} \approx \frac{\mathcal{F}}{\pi}. \tag{D.10}$$

If the reflectivity of the mirrors is high ($R \approx 1$), expression D.10 can be approximated as the part of the circulating power that is transmitted $T = 1 - R$ through the outcoupling mirror leading to the simple expression

$$\frac{P_{\text{circ}}^{\text{sym}}}{P_0} \approx \frac{1}{1-R}, \tag{D.11}$$

consistent with [171, 172]. Due to the standing wave present in the cavity, the peak power P_{peak} is

$$P_{\text{peak}} = 4 \cdot P_{\text{circ}}, \tag{D.12}$$

whereas the power at the slope of the intra cavity field P_{slope} is half the peak power:

$$P_{\text{slope}} = 2 \cdot P_{\text{circ}}. \tag{D.13}$$

D.3 Phase Gradient on Resonance

The imaginary part of the reflected field on resonance vanishes as can be seen in Equation 5.12. Therefore, the phase φ of the reflected field can be approximated as

$$\mathrm{Im}\left[E_{\mathrm{ref}}/E_{\mathrm{in}}\right] = \sin\left(\varphi\right) \approx \varphi. \tag{D.14}$$

The steepness of the phase feature can therefore be calculated as the derivative with respect to a length change L.

$$\frac{\mathrm{d}}{\mathrm{d}L}\,\mathrm{Im}\left[\frac{E_{\mathrm{ref}}}{E_{\mathrm{in}}}\right] \approx \frac{\mathrm{d}\varphi}{\mathrm{d}L} \tag{D.15}$$

Inserting the fields calculated in Equation 5.9 gives the expression

$$\frac{\mathrm{d}\varphi}{\mathrm{d}L} = \frac{4\pi}{\lambda}\cdot\frac{\left(R_1-1\right)\sqrt{R_2}}{\left(1-\sqrt{R_1R_2}\right)^2}, \tag{D.16}$$

which looks similar to the circulating power given in D.4. Dividing both equations and using the taylor expansion of Equation D.6 yields

$$\frac{\mathrm{d}\varphi}{\mathrm{d}L}\Big/\frac{P_{\mathrm{circ}}}{P_0} = \frac{16\pi}{\lambda}\cdot\frac{\sqrt{R_2}}{\left(1-\sqrt{R_2}\right)^2} = \frac{16\pi}{\lambda}\cdot\left(\frac{\sqrt[4]{R_2}}{1-\sqrt{R_2}}\right)^2 \tag{D.17}$$

$$\approx \frac{4\pi}{\lambda}. \tag{D.18}$$

As expected, the phase steepness and the circulating power are closely connected. Again, the phase feature is steeper if the beam coupled into the cavity from the less reflective side ($\bar{\rho} < 0$). The final result for the slope of the phase at resonance is

$$\frac{\mathrm{d}\varphi}{\mathrm{d}L} = \frac{8\mathcal{F}}{\lambda}\left(\frac{1-\bar{\rho}}{2}\right). \tag{D.19}$$

D.4 Coatings

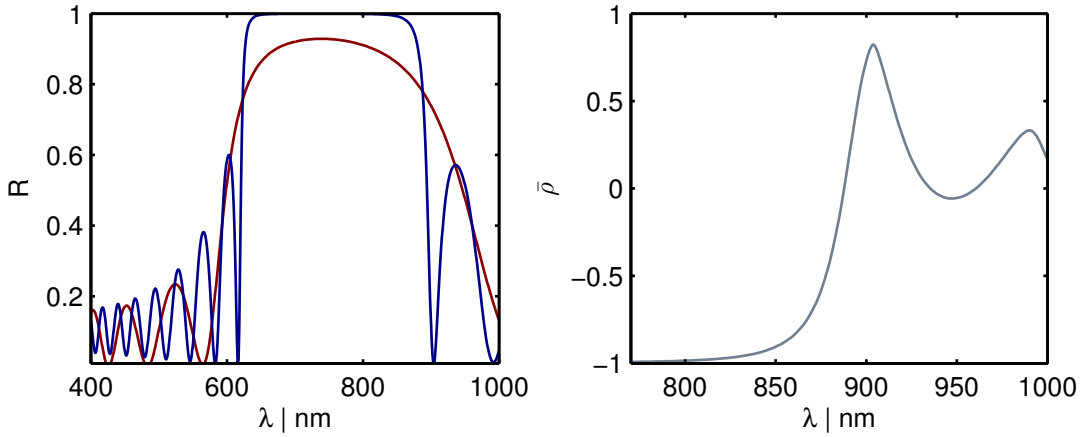

Figure D.3: Left: Calculated reflectivities for the higher/lower reflective side R_1/R_2 (blue/red). The coatings consist of 9/19 alternating layers of MgF and ZnS. **Right:** Calculated field reflectivity on resonance $\bar{\rho}$ from the reflectivities shown on the right. Note the different horizontal axis.

To create a cavity, the fiberends are coated with dielectric soft coatings, consistent of alternating layers of magnesium fluoride (MgF) and zinc sulfide (ZnS). Shown in Figure D.3 are two calculated reflectivity curves for the coatings used for the measurements in Section 5.5 with 9 layers of MgF/ZnS for the incoupling side and 19 layers of MgF/ZnS for the outcoupling side. The 9 layer coating has a calculated reflectivity of $r = 0.9208$, whereas the 19 layer coating has the higher reflectivity with a calculated value of $r = 0.9996$ at 780 nm.

As the reflectivity changes with the wavelength used, it should be possible to change the sign of $\bar{\rho}$ using a different wavelength. Shown in Figure D.3 on the right is the reflectivity on resonance, calculated from the theoretical reflectivities of the mirrors in the range where the Thorlabs PM-780 fiber is usable (770 nm to 1100 nm). In this range there are several points where a symmetric cavity with low finesse could be realized or the asymmetry be inverted ($\lambda \approx 910$ nm). Although the exact position of these points are not well known due to small uncertainties of the refractive index at higher wavelengths, both coatings only differ by the amount of layers. This should only result in an absolute shift in wavelength of ≈ 15 nm.

D.5 R_2 Measurment

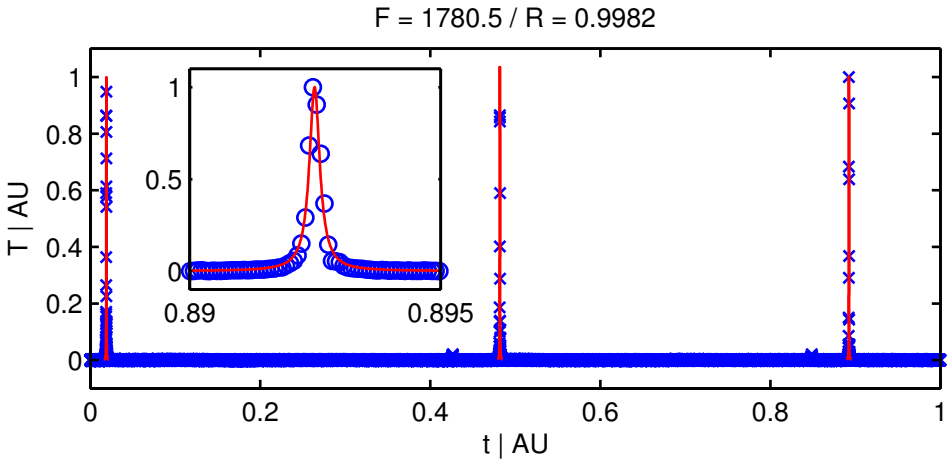

Figure D.4: Transmission of a symmetric fiber cavity to determine the reflectivity of the 19 layer coating. The fit to the free spectral range and line width yields $R = 0.9982$ or $F = 1780$.

As discussed in Section 5.1.2, the reflectivity on resonance is very dependent on the reflectivity R_2. To independently measure this reflectivity we built a symmetric (with respect to the reflectivity and radius of curvature) CC fiber cavity and measured the finesse by fitting the line width and free spectral range. The measurement is shown in Figure D.4. In this measurement the time axis had to be rescaled because the scan piezo used here showed a nonlinear behavior. The fit yields a reflectivity of $R = 0.9982$ which corresponds to a finesse of $F = 1780$. This value is below the calculated value of $R = 0.9996$, which is common, but consistent with the expectations and previous measurements.

Bibliography

[1] F. Diedrich, J. Bergquist, W. Itano and D. Wineland: "Laser Cooling to the Zero-Point Energy of Motion", Physical Review Letters **62**, 403–406 (1989), ISSN 0031-9007.

[2] K. B. Davis, M. Mewes, M. Andrews *et al.*: "Bose-Einstein Condensation in a Gas of Sodium Atoms", Physical Review Letters **75**, 3969–3973 (1995), ISSN 0031-9007.

[3] M. H. Anderson, J. R. Ensher, M. R. Matthews, C. E. Wieman and E. A. Cornell: "Observation of Bose-Einstein Condensation in a Dilute Atomic Vapor.", Science **269**, 198–201 (1995), ISSN 1095-9203.

[4] I. Chiorescu, Y. Nakamura, C. J. P. M. Harmans and J. E. Mooij: "Coherent quantum dynamics of a superconducting flux qubit.", Science (New York, N.Y.) **299**, 1869–71 (2003), ISSN 1095-9203.

[5] J. D. Teufel, T. Donner, D. Li *et al.*: "Sideband cooling of micromechanical motion to the quantum ground state.", Nature **475**, 359–63 (2011), ISSN 1476-4687.

[6] J. Chan, T. P. M. Alegre, A. H. Safavi-Naeini *et al.*: "Laser cooling of a nanomechanical oscillator into its quantum ground state.", Nature **478**, 89–92 (2011), ISSN 1476-4687.

[7] V. B. Braginsky and A. B. Manukin: "Ponderomotive effects of electromagnetic radiation", Soviet Physics JETP **25**, 653–655 (1967).

[8] S. Gröblacher, J. B. Hertzberg, M. R. Vanner *et al.*: "Demonstration of an ultracold micro-optomechanical oscillator in a cryogenic cavity", Nature Physics **5**, 485–488 (2009), ISSN 1745-2473.

[9] J. C. Sankey, C. Yang, B. M. Zwickl, a. M. Jayich and J. G. E. Harris: "Strong and tunable nonlinear optomechanical coupling in a low-loss system", Nature Physics **6**, 707–712 (2010), ISSN 1745-2473.

[10] P. Cohadon, a. Heidmann and M. Pinard: "Cooling of a Mirror by Radiation Pressure", Physical Review Letters **83**, 3174–3177 (1999), ISSN 0031-9007.

[11] a. Schliesser, R. Rivière, G. Anetsberger, O. Arcizet and T. J. Kippenberg: "Resolved-sideband cooling of a micromechanical oscillator", Nature Physics **4**, 415–419 (2008), ISSN 1745-2473.

[12] A. H. Safavi-Naeini, J. Chan, J. T. Hill *et al.*: "Observation of Quantum Motion of a Nanomechanical Resonator", Physical Review Letters **108**, 033602 (2012), ISSN 0031-9007.

[13] J. T. Hill, A. H. Safavi-Naeini, J. Chan and O. Painter: "Coherent optical wavelength conversion via cavity optomechanics.", Nature communications **3**, 1196 (2012), ISSN 2041-1723.

[14] A. H. Safavi-Naeini, S. Gröblacher, J. T. Hill *et al.*: "Squeezed light from a silicon micromechanical resonator.", Nature **500**, 185–9 (2013), ISSN 1476-4687.

[15] T. P. Purdy, P.-L. Yu, R. W. Peterson, N. S. Kampel and C. A. Regal: "Strong Optomechanical Squeezing of Light", Physical Review X **3**, 031012 (2013), ISSN 2160-3308.

[16] T. Rocheleau, T. Ndukum, C. Macklin *et al.*: "Preparation and detection of a mechanical resonator near the ground state of motion", Nature **463**, 72–75 (2010).

[17] R. Rivière, S. Deléglise, S. Weis *et al.*: "Optomechanical sideband cooling of a micromechanical oscillator close to the quantum ground state", Physical Review A **83**, 063835 (2011), ISSN 1050-2947.

[18] D. Lee, M. Underwood, D. Mason *et al.*: "Observation of Quantum Motion in a Nanogram-scale Object", arXiv page 26 (2014).

[19] T. P. Purdy, R. W. Peterson, P.-L. Yu and C. A. Regal: "Cavity optomechanics with Si 3 N 4 membranes at cryogenic temperatures", New Journal of Physics **14**, 115021 (2012), ISSN 1367-2630.

[20] P. Treutlein, D. Hunger, S. Camerer, T. Hänsch and J. Reichel: "Bose-Einstein Condensate Coupled to a Nanomechanical Resonator on an Atom Chip", Physical Review Letters **99**, 1–4 (2007), ISSN 0031-9007.

[21] D. Rugar, R. Budakian, H. J. Mamin and B. W. Chui: "Single spin detection by magnetic resonance force microscopy.", Nature **430**, 329–32 (2004), ISSN 1476-4687.

[22] M. Aspelmeyer, T. J. Kippenberg and F. Marquardt (editors): *Cavity Optomechanics*, Springer Berlin Heidelberg, Berlin, Heidelberg (2014), ISBN 978-3-642-55311-0.

[23] A. D. O'Connell, M. Hofheinz, M. Ansmann *et al.*: "Quantum ground state and single-phonon control of a mechanical resonator.", Nature **464**, 697–703 (2010), ISSN 1476-4687.

[24] S. Chu: "Cold atoms and quantum control.", Nature **416**, 206–10 (2002), ISSN 0028-0836.

[25] D. McClelland, N. Mavalvala, Y. Chen and R. Schnabel: "Advanced interferometry, quantum optics and optomechanics in gravitational wave detectors", Laser & Photonics Reviews **696**, n/a–n/a (2011), ISSN 18638880.

[26] O. Arcizet, V. Jacques, a. Siria *et al.*: "A single nitrogen-vacancy defect coupled to a nanomechanical oscillator", Nature Physics **7**, 879–883 (2011), ISSN 1745-2473.

[27] P. Rabl, P. Cappellaro, M. Dutt *et al.*: "Strong magnetic coupling between an electronic spin qubit and a mechanical resonator", Physical Review B **79**, 041302 (2009), ISSN 1098-0121.

[28] S. Kolkowitz, A. C. B. Jayich, Q. P. Unterreithmeier *et al.*: "Coherent sensing of a mechanical resonator with a single-spin qubit.", Science (New York, N.Y.) **335**, 1603–6 (2012), ISSN 1095-9203.

[29] a. André, D. DeMille, J. M. Doyle *et al.*: "A coherent all-electrical interface between polar molecules and mesoscopic superconducting resonators", Nature Physics **2**, 636–642 (2006), ISSN 1745-2473.

[30] P. Rabl, D. DeMille, J. Doyle *et al.*: "Hybrid Quantum Processors: Molecular Ensembles as Quantum Memory for Solid State Circuits", Physical Review Letters **97**, 033003 (2006), ISSN 0031-9007.

[31] J. Verdú, H. Zoubi, C. Koller *et al.*: "Strong Magnetic Coupling of an Ultracold Gas to a Superconducting Waveguide Cavity", Physical Review Letters **103**, 043603 (2009), ISSN 0031-9007.

[32] D. Petrosyan and M. Fleischhauer: "Quantum Information Processing with Single Photons and Atomic Ensembles in Microwave Coplanar Waveguide Resonators", Physical Review Letters **100**, 170501 (2008), ISSN 0031-9007.

[33] S. Bernon, H. Hattermann, D. Bothner *et al.*: "Manipulation and coherence of ultra-cold atoms on a superconducting atom chip.", Nature communications **4**, 2380 (2013), ISSN 2041-1723.

[34] F. Jessen, M. Knufinke, S. C. Bell *et al.*: "Trapping of ultracold atoms in a 3He/4He dilution refrigerator", Applied Physics B **116**, 665–671 (2013), ISSN 0946-2171.

[35] S. Minniberger, F. Diorico, S. Haslinger *et al.*: "Magnetic conveyor belt transport of ultracold atoms to a superconducting atomchip", Applied Physics B **116**, 1017–1021 (2014), ISSN 0946-2171.

[36] S. Ritter, C. Nölleke, C. Hahn *et al.*: "An elementary quantum network of single atoms in optical cavities.", Nature **484**, 195–200 (2012), ISSN 1476-4687.

[37] J. D. Thompson, B. M. Zwickl, a. M. Jayich *et al.*: "Strong dispersive coupling of a high-finesse cavity to a micromechanical membrane.", Nature **452**, 72–5 (2008), ISSN 1476-4687.

[38] K. Hammerer, K. Stannigel, C. Genes *et al.*: "Optical lattices with micromechanical mirrors", Physical Review A **82**, 021803 (2010), ISSN 1050-2947.

[39] B. Vogell: "Hybrid Quantum Systems: Interfacing a Micromechanical Resonator with Ultracold Atoms", Masters thesis (2012).

[40] B. Vogell, K. Stannigel, P. Zoller *et al.*: "Cavity-enhanced long-distance coupling of an atomic ensemble to a micromechanical membrane", Physical Review A **87**, 023816 (2013), ISSN 1050-2947.

[41] B. Vogell, T. Kampschulte, M. T. Rakher *et al.*: "Long Distance Coupling of a Quantum Mechanical Oscillator to the Internal States of an Atomic Ensemble", page 14 (2014).

[42] J. S. Bennett, L. S. Madsen, M. Baker, H. Rubinsztein-Dunlop and W. P. Bowen: "Coherent control and feedback cooling in a remotely coupled hybrid atom–optomechanical system", New Journal of Physics **16**, 083036 (2014), ISSN 1367-2630.

[43] F. Bariani, S. Singh, L. F. Buchmann, M. Vengalattore and P. Meystre: "Hybrid optomechanical cooling by atomic L systems", Physical Review A **90**, 033838 (2014), ISSN 1050-2947.

[44] K. Hammerer, M. Aspelmeyer, E. Polzik and P. Zoller: "Establishing Einstein-Poldosky-Rosen Channels between Nanomechanics and Atomic Ensembles", Physical Review Letters **102**, 1–4 (2009), ISSN 0031-9007.

[45] S. Camerer, M. Korppi, A. Jöckel *et al.*: "Realization of an Optomechanical Interface Between Ultracold Atoms and a Membrane", Physical Review Letters **107**, 223001 (2011), ISSN 0031-9007.

[46] A. Jöckel, A. Faber, T. Kampschulte *et al.*: "Sympathetic cooling of a membrane oscillator in a hybrid mechanical–atomic system", Nature Nanotechnology (2014), ISSN 1748-3387.

[47] D. Hunger, T. Steinmetz, Y. Colombe *et al.*: "A fiber Fabry–Perot cavity with high finesse", New Journal of Physics **12**, 065038 (2010), ISSN 1367-2630.

[48] W. Allers, a. Schwarz, U. D. Schwarz and R. Wiesendanger: "A scanning force microscope with atomic resolution in ultrahigh vacuum and at low temperatures", Review of Scientific Instruments **69**, 221 (1998), ISSN 00346748.

[49] S. Chu, L. Hollberg, J. Bjorkholm, A. Cable and A. Ashkin: "Three-dimensional viscous confinement and cooling of atoms by resonance radiation pressure", Physical Review Letters **55**, 48–51 (1985), ISSN 0031-9007.

[50] A. Kerman, V. Vuletić, C. Chin and S. Chu: "Beyond Optical Molasses: 3D Raman Sideband Cooling of Atomic Cesium to High Phase-Space Density", Physical Review Letters **84**, 439–442 (2000), ISSN 0031-9007.

[51] W. Ketterle and N. J. van Druten: "Evaporative Cooling of Trapped Atoms", Advances in Atomic, Molecular, and Optical Physics **37**, 181–236 (1996).

[52] M. Wolke, J. Klinner, H. Keß ler and A. Hemmerich: "Cavity cooling below the recoil limit.", Science (New York, N.Y.) **337**, 75–8 (2012), ISSN 1095-9203.

[53] S. Riedl, M. Lettner, C. Vo *et al.*: "Bose-Einstein condensate as a quantum memory for a photonic polarization qubit", Physical Review A **85**, 022318 (2012), ISSN 1050-2947.

[54] M. Lettner, M. Mücke, S. Riedl *et al.*: "Remote Entanglement between a Single Atom and a Bose-Einstein Condensate", Physical Review Letters **106**, 210503 (2011), ISSN 0031-9007.

[55] M. Lukin, S. Yelin and M. Fleischhauer: "Entanglement of Atomic Ensembles by Trapping Correlated Photon States", Physical Review Letters **84**, 4232–4235 (2000), ISSN 0031-9007.

[56] C. H. van der Wal, M. D. Eisaman, A. André *et al.*: "Atomic memory for correlated photon states.", Science (New York, N.Y.) **301**, 196–200 (2003), ISSN 1095-9203.

[57] M. Poot and H. S. van der Zant: "Mechanical systems in the quantum regime", Physics Reports **511**, 273–335 (2012), ISSN 03701573.

[58] B. Abbott, R. Abbott, R. Adhikari *et al.*: "Observation of a kilogram-scale oscillator near its quantum ground state", New Journal of Physics **11**, 073032 (2009), ISSN 1367-2630.

[59] D. Kleckner, B. Pepper, E. Jeffrey *et al.*: "Optomechanical trampoline resonators", Optics Express **19**, 19708 (2011), ISSN 1094-4087.

[60] V. Ilchenko, P. Volikov, V. Velichansky *et al.*: "Strain-tunable high-Q optical microsphere resonator", Optics Communications **145**, 86–90 (1998), ISSN 00304018.

[61] I. Favero, S. Stapfner, D. Hunger *et al.*: "Fluctuating nanomechanical system in a high finesse optical microcavity", Optics Express **17**, 12813 (2009), ISSN 1094-4087.

[62] K. Srinivasan, P. Barclay, M. Borselli and O. Painter: "An optical-fiber-based probe for photonic crystal microcavities", IEEE Journal on Selected Areas in Communications **23**, 1321–1329 (2005), ISSN 0733-8716.

[63] S. M. Meenehan, J. D. Cohen, S. Gröblacher *et al.*: "Silicon optomechanical crystal resonator at millikelvin temperatures", Physical Review A **90**, 011803 (2014), ISSN 1050-2947.

[64] V. R. Almeida, R. R. Panepucci and M. Lipson: "Nanotaper for compact mode conversion", Optics Letters **28**, 1302 (2003), ISSN 0146-9592.

[65] J. D. Cohen, S. M. Meenehan and O. Painter: "Optical coupling to nanoscale optomechanical cavities for near quantum-limited motion transduction.", Optics express **21**, 11227–36 (2013), ISSN 1094-4087.

[66] D. O'Shea, C. Junge, S. Nickel, M. Pöllinger and A. Rauschenbeutel: "Ultra-high Q whispering-gallery-mode bottle microresonators: properties and applications", in A. V. Kudryashov, A. H. Paxton and V. S. Ilchenko (editors), "Proc. SPIE 7913, Laser Resonators and Beam Control XIII, 79130N", pages 79130N–79130N–11 (2011).

[67] S. Chakram, Y. Patil, L. Chang and M. Vengalattore: "Dissipation in Ultrahigh Quality Factor SiN Membrane Resonators", Physical Review Letters **112**, 127201 (2014), ISSN 0031-9007.

[68] G. D. Cole: "Cavity optomechanics with low-noise crystalline mirrors", volume 8458, page 845807 (2012).

[69] S. Gröblacher: "Quantum opto-mechanics with micromirrors: combining nano-mechanics with quantum optics", Ph.D. thesis (2010).

[70] U. Kemiktarak, M. Metcalfe, M. Durand and J. Lawall: "Mechanically compliant grating reflectors for optomechanics", Applied Physics Letters **100**, 061124 (2012), ISSN 00036951.

[71] D. Rugar, H. J. Mamin and P. Guethner: "Improved fiber-optic interferometer for atomic force microscopy", Applied Physics Letters **55**, 2588 (1989), ISSN 00036951.

[72] S. Stapfner, I. Favero, D. Hunger *et al.*: "Cavity nano-optomechanics: a nanomechanical system in a high finesse optical cavity", in V. N. Zadkov and T. Durt (editors), "Proc. SPIE 7727", volume 7727, pages 772706–772706–12 (2010).

[73] S. Stapfner, L. Ost, D. Hunger *et al.*: "Cavity-enhanced optical detection of carbon nanotube Brownian motion", Applied Physics Letters **102**, 151910 (2013), ISSN 00036951.

[74] N. E. Flowers-Jacobs, S. W. Hoch, J. C. Sankey *et al.*: "Fiber-cavity-based optomechanical device", Applied Physics Letters **101**, 221109 (2012), ISSN 00036951.

[75] A. M. Jayich, J. C. Sankey, K. Bø rkje *et al.*: "Cryogenic optomechanics with a Si 3 N 4 membrane and classical laser noise", New Journal of Physics **14**, 115018 (2012), ISSN 1367-2630.

[76] E. Gil-Santos, D. Ramos, V. Pini *et al.*: "Optical back-action in silicon nanowire resonators: bolometric versus radiation pressure effects", New Journal of Physics **15**, 035001 (2013), ISSN 1367-2630.

[77] M. Korppi: "Optomechanical Coupling between Ultracold Atoms and a Membrane Oscillator", Phd thesis (2014).

[78] R. Kitamura, L. Pilon and M. Jonasz: "Optical constants of silica glass from extreme ultraviolet to far infrared at near room temperature", Applied Optics **46**, 8118 (2007), ISSN 0003-6935.

[79] A. Eichler, J. Moser, J. Chaste *et al.*: "Nonlinear damping in mechanical resonators made from carbon nanotubes and graphene.", Nature nanotechnology **6**, 339–42 (2011), ISSN 1748-3395.

[80] R. R. Nair, P. Blake, A. N. Grigorenko *et al.*: "Fine structure constant defines visual transparency of graphene.", Science (New York, N.Y.) **320**, 1308 (2008), ISSN 1095-9203.

[81] C. Biancofiore, M. Karuza, M. Galassi *et al.*: "Quantum dynamics of an optical cavity coupled to a thin semitransparent membrane: Effect of membrane absorption", Physical Review A **84**, 1–12 (2011), ISSN 1050-2947.

[82] H. Zhong, A. Schwarz and R. Wiesendanger: "Miniaturized high-precision piezo driven two axes stepper goniometer.", The Review of scientific instruments **85**, 045006 (2014), ISSN 1089-7623.

[83] M. Aspelmeyer, T. J. Kippenberg and F. Marquardt: "Cavity Optomechanics", arXiv page 65 (2013).

[84] G. Milburn and M. Woolley: "An Introduction to Quantum Optomechanics", Acta Physica Slovaca. Reviews and Tutorials **61**, 483–601 (2011), ISSN 1336-040X.

[85] a. M. Jayich, J. C. Sankey, B. M. Zwickl *et al.*: "Dispersive optomechanics: a membrane inside a cavity", New Journal of Physics **10**, 095008 (2008), ISSN 1367-2630.

[86] D. Wilson: "Cavity optomechanics with high-stress silicon nitride films", Phd thesis (2012).

[87] R. Grimm, M. Weidemüller and Y. B. Ovchinnikov: "Optical dipole traps for neutral atoms", arXiv **physics.at** (1999).

[88] G. Raithel, W. Phillips and S. Rolston: "Collapse and Revivals of Wave Packets in Optical Lattices", Physical Review Letters **81**, 3615–3618 (1998), ISSN 0031-9007.

[89] a. Görlitz, M. Weidemüller, T. Hänsch and a. Hemmerich: "Observing the Position Spread of Atomic Wave Packets", Physical Review Letters **78**, 2096–2099 (1997), ISSN 0031-9007.

[90] T. P. Purdy, R. W. Peterson and C. A. Regal: "Observation of Radiation Pressure Shot Noise on a Macroscopic Object", Science **339**, 801–804 (2013), ISSN 0036-8075.

[91] J. P. Gordon and A. Ashkin: "Motion of atoms in a radiation trap", Physical Review A **21**, 1606–1617 (1980), ISSN 0556-2791.

[92] K. Ruschmeier: "Aufbau eines für die 300mK-10T-UHV-Kryostatsystems Rasterkraftmikroskopie und Analyse der Kraftsensortemperatur", Phd thesis (2014).

[93] K. Hammerer, A. S. Sø rensen and E. S. Polzik: "Quantum interface between light and atomic ensembles", Reviews of Modern Physics **82**, 1041–1093 (2010), ISSN 0034-6861.

[94] F. Kaminski: "Coherent Atom-Light Interaction in an Ultracold Atomic Gas Experimental Study of Faraday Rotation Imaging and Matter-Wave Superradiance", Phd thesis (2012).

[95] Y.-J. Lin, K. Jiménez-García and I. B. Spielman: "Spin-orbit-coupled Bose-Einstein condensates.", Nature **471**, 83–6 (2011), ISSN 1476-4687.

[96] W. Ketterle, D. S. Durfee and D. M. Stamper-Kurn: "Making, probing and understanding Bose-Einstein condensates", arXiv **cond-mat** (1999).

[97] K. Dieckmann, R. Spreeuw, M. Weidemüller and J. Walraven: "Two-dimensional magneto-optical trap as a source of slow atoms", Physical Review A **58**, 3891–3895 (1998), ISSN 1050-2947.

[98] H. Hess, G. Kochanski, J. Doyle *et al.*: "Magnetic trapping of spin-polarized atomic hydrogen", Physical Review Letters **59**, 672–675 (1987), ISSN 0031-9007.

[99] R. van Roijen, J. Berkhout, S. Jaakkola and J. Walraven: "Experiments with Atomic Hydrogen in a Magnetic Trapping Field", Physical Review Letters **61**, 931–934 (1988), ISSN 0031-9007.

[100] N. Masuhara, J. Doyle, J. Sandberg *et al.*: "Evaporative Cooling of Spin-Polarized Atomic Hydrogen", Physical Review Letters **61**, 935–938 (1988), ISSN 0031-9007.

[101] H. Schmaljohann: "Spindynamik in Bose-Einstein Kondensaten", Phd thesis, Hamburg (2004).

[102] S. E. Dörscher: "Creation of ytterbium gases with a compact 2D/3D-MOT setup", Ph.D. thesis (2013).

[103] J. Struck: "Artificial Gauge Fields in Driven Optical Lattices", Ph.D. thesis (2013).

[104] J. Heize: "From Higher Bands to Higher Spins: Ultracold Fermions in Novel Regimes", Ph.D. thesis (2013).

[105] A. Grote: "Aufbau eines Ultrahochvakuumsystems und einer 2D-3D-Fallenkombination eines Quantengasmessplatzes für Forschung und Lehre", Diploma thesis (2011).

[106] M. Weidemüller and C. Zimmermann: *Interactions in Ultracold Gases*, Wiley-VCH Verlag GmbH & Co. KGaA, Weinheim, FRG (2003), ISBN 9783527603411.

[107] D. A. Steck: "Rubidium 87 D Line Data", pages 1–31 (2001).

[108] E. D. Black: "An introduction to Pound–Drever–Hall laser frequency stabilization", American Journal of Physics **69**, 79 (2001), ISSN 00029505.

[109] S. Ospelkaus-Schwarzer: "Quantum Degenerate Fermi-Bose Mixtures of 40K and 87Rb in 3D Optical Lattices", Ph.D. thesis (2006).

[110] R. Dinter: "Aufbau und Charakterisierung einer Magnetfalle zur simultanen Speicherung von K und Rb", Diploma thesis (2004).

[111] C. Ospelkaus: "Fermi-Bose mixtures - From mean-field interactions to ultracold chemistry", Ph.D. thesis (2006).

[112] M. Erhard: "Experimente mit mehrkomponentigen Bose-Einstein-Kondensaten", Phd thesis (2004).

[113] B. Hundt: "Momentum-Resolved Optical Lattice Modulation Spectroscopy on Bose-Fermi Mixtures Impulsaufgelöste Modulations-Spektroskopie an Bose-Fermi-Mischungen in optischen Gittern", Diploma thesis (2011).

[114] M. Jambor: "A Diffraction Limited Objective Lens for the Detection of Bose-Einstein Condensates Coupled to Micro-Mechanical Devices", Bachelors thesis (2012).

[115] C. Staarmann: "Higher Orbital Physics in Spin-Dependent Hexagonal Optical Lattices", Diploma thesis (2011).

[116] E. Hecht: *Optik*, Oldenbourg (2009), ISBN 3-486-58861-3.

[117] D. Hunger, C. Deutsch, R. J. Barbour, R. J. Warburton and J. Reichel: "Laser micro-fabrication of concave, low-roughness features in silica", AIP Advances **2**, 012119 (2012), ISSN 21583226.

[118] F. Vega: "Laser application for optical glass polishing", Optical Engineering **37**, 272 (1998), ISSN 0091-3286.

[119] K. M. Nowak, H. J. Baker and D. R. Hall: "Efficient laser polishing of silica micro-optic components", Applied Optics **45**, 162 (2006), ISSN 0003-6935.

[120] T. Steinmetz, Y. Colombe, D. Hunger *et al.*: "Stable fiber-based Fabry-Perot cavity", Applied Physics Letters **89**, 111110 (2006), ISSN 00036951.

[121] P. Christoph: "Fiber Cavities for Quantum Optomechanics: Concepts, Manufacturing and Characterization", Masters thesis (2013).

[122] M. D. Feit and A. M. Rubenchik: "Mechanisms of CO2 laser mitigation of laser damage growth in fused silica", in G. J. Exarhos, A. H. Guenther, N. Kaiser *et al.* (editors), "Proc. SPIE 4932, Laser-Induced Damage in Optical Materials: 2002 and 7th International Workshop on Laser Beam and Optics Characterization", pages 91–102 (2003).

[123] B. Petrak, K. Konthasinghe, S. Perez and A. Muller: "Feedback-controlled laser fabrication of micromirror substrates.", The Review of scientific instruments **82**, 123112 (2011), ISSN 1089-7623.

[124] N. Thau: "Optical fiber cavities", Masters thesis (2012).

[125] F. Träger (editor): *Springer Handbook of Lasers and Optics*, Springer New York, New York, NY (2007), ISBN 978-0-387-95579-7.

[126] W. Drexler and J. G. Fujimoto (editors): *Optical Coherence Tomography*, Biological and Medical Physics, Biomedical Engineering, Springer Berlin Heidelberg, Berlin, Heidelberg (2008), ISBN 978-3-540-77549-2.

[127] H. Farid and E. Simoncelli: "Differentiation of Discrete Multidimensional Signals", IEEE Transactions on Image Processing **13**, 496–508 (2004), ISSN 1057-7149.

[128] D. Malacara, M. Servín and Z. Malacara: *Interferogram Analysis For Optical Testing, Second Edition*, CRC Press (2005), ISBN 978-1-57444-682-1.

[129] D. Malacara (editor): *Optical Shop Testing*, John Wiley & Sons, Inc., Hoboken, NJ, USA (2007), ISBN 9780470135976.

[130] J. Vargas, J. A. Quiroga, C. O. S. Sorzano, J. C. Estrada and J. M. Carazo: "Two-step interferometry by a regularized optical flow algorithm.", Optics letters **36**, 3485–7 (2011), ISSN 1539-4794.

[131] T.-p. Ku, C.-y. Huang, B.-w. Shiau and D.-j. Han: "Phase shifting interferometry of cold atoms.", Optics express **19**, 3730–41 (2011), ISSN 1094-4087.

[132] P. S. Light, C. Perrella and A. N. Luiten: "Phase-sensitive imaging of cold atoms at the shot-noise limit", Applied Physics Letters **102**, 171108 (2013), ISSN 00036951.

[133] M. Peck: "Interferometry mathematics, algorithms, and data", pages 1–50 (2010).

[134] D. C. Ghiglia and M. D. Pritt: *Two-dimensional phase unwrapping: theory, algorithms, and software*, Wiley-Interscience publication, Wiley (1998), ISBN 9780471249351.

[135] M. Costantini: "A novel phase unwrapping method based on network programming", IEEE Transactions on Geoscience and Remote Sensing **36**, 813–821 (1998), ISSN 01962892.

[136] Z. Wang and B. Han: "Advanced iterative algorithm for phase extraction of randomly phase-shifted interferograms", Optics Letters **29**, 1671 (2004), ISSN 0146-9592.

[137] H. Iwai, C. Fang-Yen, G. Popescu *et al.*: "Quantitative phase imaging using actively stabilized phase-shifting low-coherence interferometry", Optics Letters **29**, 2399 (2004), ISSN 0146-9592.

[138] X. Li, T. Yamauchi, H. Iwai *et al.*: "Full-field quantitative phase imaging by white-light interferometry with active phase stabilization and its application to biological samples", Optics Letters **31**, 1830 (2006), ISSN 0146-9592.

[139] T. Yamauchi, H. Iwai, M. Miwa and Y. Yamashita: "Measurement of topographic phase image of living cells by white-light phase-shifting microscope with active stabilization of optical path difference", in J. G. Fujimoto, J. A. Izatt and V. V. Tuchin (editors), "Proc. SPIE 6429, Coherence Domain Optical Methods and Optical Coherence Tomography in Biomedicine XI", volume 6429, pages 64291Q–64291Q–8 (2007).

[140] P. J. D. Groot: "Vibration in phase-shifting interferometry", Journal of the Optical Society of America A **12**, 354 (1995), ISSN 1084-7529.

[141] O. Svelto: *Principles of Lasers*, Springer US, Boston, MA (2010), ISBN 978-1-4419-1301-2.

[142] P. F. Goldsmith: *Quasioptical Systems*, IEEE (1998), ISBN 9780470546291.

[143] E. R. Abraham and E. a. Cornell: "Teflon feedthrough for coupling optical fibers into ultrahigh vacuum systems.", Applied optics **37**, 1762–3 (1998), ISSN 0003-6935.

[144] P. Rothfos: "Untersuchungen zum Aufbau eines optischen Faserresonators im Vakuum", Bachelor thesis (2013).

[145] T. J. Kippenberg, A. Schliesser and M. L. Gorodetsky: "Phase noise measurement of external cavity diode lasers and implications for optomechanical sideband cooling of GHz mechanical modes", New Journal of Physics **15**, 015019 (2013), ISSN 1367-2630.

[146] D. Kleckner and D. Bouwmeester: "Sub-kelvin optical cooling of a micromechanical resonator", Nature **444**, 75–78 (2006).

[147] O. Arcizet, P.-F. P.-F. Cohadon, T. Briant, M. Pinard and A. Heidmann: "Radiation-pressure cooling and optomechanical instability of a micromirror.", Nature **444**, 71–4 (2006), ISSN 1476-4687.

[148] C. Yang: "Progress Toward Observing Quantum Effects in an Optomechanical System in Cryogenics", Phd thesis (2011).

[149] J. T. Karpel: "Alignment Tolerance of a Dielectric Membrane in a Fabry-Perot Cavity", Bachelor thesis (2014).

[150] B. Abeln: "Aufbau und Charakterisierung einer gekreuzten Dipolfalle für kalte Atome", Bachelors thesis (2014).

[151] A. K. Hüttel, G. A. Steele, B. Witkamp *et al.*: "Carbon nanotubes as ultrahigh quality factor mechanical resonators.", Nano letters **9**, 2547–52 (2009), ISSN 1530-6992.

[152] B. Lassagne, Y. Tarakanov, J. Kinaret *et al.*: "Coupling mechanics to charge transport in carbon nanotube mechanical resonators.", Science (New York, N.Y.) **325**, 1107–10 (2009), ISSN 1095-9203.

[153] K. W. Murch, K. L. Moore, S. Gupta and D. M. Stamper-Kurn: "Observation of quantum-measurement backaction with an ultracold atomic gas", Nature Physics **4**, 561–564 (2008), ISSN 1745-2473.

[154] M. Ludwig, B. Kubala and F. Marquardt: "The optomechanical instability in the quantum regime", New Journal of Physics **10**, 095013 (2008), ISSN 1367-2630.

[155] P. Rabl: "Photon Blockade Effect in Optomechanical Systems", Physical Review Letters **107**, 063601 (2011), ISSN 0031-9007.

[156] M. Greiner, I. Bloch, T. Hänsch and T. Esslinger: "Magnetic transport of trapped cold atoms over a large distance", Physical Review A **63**, 1–4 (2001), ISSN 1050-2947.

[157] C. Silber, S. Günther, C. Marzok *et al.*: "Quantum-Degenerate Mixture of Fermionic Lithium and Bosonic Rubidium Gases", Physical Review Letters **95**, 170408 (2005), ISSN 0031-9007.

[158] S. Steinke, S. Singh, M. Tasgin *et al.*: "Quantum-measurement backaction from a Bose-Einstein condensate coupled to a mechanical oscillator", Physical Review A **84**, 1–12 (2011), ISSN 1050-2947.

[159] N. Lo Gullo, T. Busch, G. Palma and M. Paternostro: "Probing mechanical quantum coherence with an ultracold-atom meter", Physical Review A **84**, 1–7 (2011), ISSN 1050-2947.

[160] S. Singh and P. Meystre: "Atomic probe Wigner tomography of a nanomechanical system", Physical Review A **81**, 041804 (2010), ISSN 1050-2947.

[161] S. Ribeiro and S. Scheel: "Controlled ripple texturing of suspended graphene membranes due to coupling with ultracold atoms", Physical Review A **88**, 052521 (2013), ISSN 1050-2947.

[162] A. Geraci and J. Kitching: "Ultracold mechanical resonators coupled to atoms in an optical lattice", Physical Review A **80**, 1–5 (2009), ISSN 1050-2947.

[163] A. B. Bhattacherjee and T. Brandes: "Phonon laser effect and Dicke–Hepp–Lieb superradiant phase transition in magnetic cantilever coupled to a Bose–Einstein condensate", Canadian Journal of Physics **91**, 639–644 (2013), ISSN 0008-4204.

[164] R. O. Pohl: "Low-temperature thermal conductivity and acoustic attenuation in amorphous solids", **74** (2002).

[165] M. M. Leivo and J. P. Pekola: "Thermal characteristics of silicon nitride membranes at sub-Kelvin temperatures", Applied Physics Letters **72**, 1305 (1998), ISSN 00036951.

[166] B. Zink and F. Hellman: "Specific heat and thermal conductivity of low-stress amorphous Si–N membranes", Solid State Communications **129**, 199–204 (2004), ISSN 00381098.

[167] M. Wallquist, K. Hammerer, P. Zoller *et al.*: "Single-atom cavity QED and optomicromechanics", Physical Review A **81**, 1–17 (2010), ISSN 1050-2947.

[168] A. Gałka, J. Telega and S. Tokarzewski: "Heat equation with temperature-dependent conductivity coefficients and macroscopic properties of microheterogeneous media", Mathematical and Computer Modelling **33**, 927–942 (2001), ISSN 08957177.

[169] T. Båå k: "Silicon oxynitride; a material for GRIN optics.", Applied optics **21**, 1069–72 (1982), ISSN 0003-6935.

[170] B. M. Zwickl: "Progress Toward Observation of Radiation Pressure Shot Noise", Phd thesis (2011).

[171] D. Meschede: *Optik, Licht und Laser*, Vieweg+Teubner, Wiesbaden (2008), ISBN 978-3-8351-0143-2.

[172] A. E. Siegman: *Lasers*, University Science Books (1986), ISBN 9780935702118.

Danksagung

Als erstes möchte ich meinen Doktorvater Klaus Sengstock nennen. Danke für die Unterstützung während der letzten fünf Jahre und insbesondere für die großen Freiheiten, die du mir beim Aufbau des Projektes gelassen hast. Es war immer eine Freude in deiner Gruppe zu arbeiten. Das Klima, das du geschaffen hast, war ideal zur Diskussion von neuen Ideen. Des Weiteren möchte ich Roland Wiesendanger für die Übernahme des Zweitgutachtens der Disputation und die Unterstützung von der „Cryo-Seite“ danken. Zudem danke ich Roman Schnabel für die Übernahme des Zweitgutachtens der Dissertation.

Insbesondere möchte ich alle, die Teil des inzwischen stark gewachsenen *Team-Nano* sind oder waren, hier erwähnen: Benjamin Abeln, Christoph Becker, René Chaeib, Philipp Christoph, Jannes Heinze, Ortwin Hellmig, Martin Jambor, Philip Rothfos, Alexander Schwarz, Christina Staarmann, Patrick Windpassinger und Hai Zhong. Ohne euch wäre diese Arbeit nicht möglich gewesen. Ein großer Dank geht auch an alle anderen Mitarbeiter des Instituts. Eure Tür war immer offen und man konnte jederzeit produktiv diskutieren oder gelegentlich Zerstreuung finden.

Des Weiteren möchte ich allen meinen Freunden, innerhalb und ausserhalb der Uni, für die Unterstützung und meiner Familie und Freundin für den Rückhalt danken.

Mir wird diese Zeit immer in feiner Erinnerung bleiben. Danke!